Study of K_x-Ray Multiplicities of Evaporation Residues in Heavy Fusion Systems Using the MINIBALL Spectrometer

Sebastian Reichert

Master-Thesis

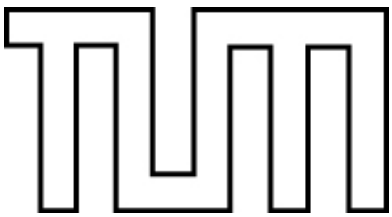

München 2013

Study of K_x-Ray Multiplicities of Evaporation Residues in Heavy Fusion Systems Using the MINIBALL Spectrometer

Untersuchung der Multiplizität charakteristischer Röntgenstrahlung nach Fusionsprozessen schwerer Kerne mit dem MINIBALL Spektrometer

Sebastian Reichert

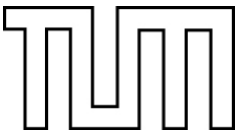

Master Arbeit

am Physik Department der
Technischen Universität München

vorgelegt von
Sebastian Reichert

im Studiengang
Kern-, Teilchen- und Astrophysik

Themensteller: Prof. Dr. Walter Henning

München, den 1. Oktober 2013

Contents

Introduction

Exotic nuclei far off the valley of stability and especially the super heavy elements have unique sensitivity to specific aspects of the nuclear interaction and of many-body dynamics. They help us to explore the nuclear structure towards the limits of nuclear binding and to increase predictive power of theories to simulate and calculate the behaviour of all nuclei.

The production of exotic nuclei is usually done by fusion of accelerated ions with heavy nuclei as targets. The initial decay of the highly excited compound nucleus is very fast and takes place in general by particle emission (protons-, neutrons and alpha-particles; for the heaviest nuclei nearly exclusively neutrons). Below the particle thresholds the remaining evaporation residues decay by electromagnetic transitions to their ground states, mostly by fast gamma-ray emission. Since the nuclei produced by fusion are generally on the proton-rich side of the valley of stability, they are unstable and radioactive. The heaviest nuclei produced up to now, i.e. super heavy elements, mostly decay by a sequence of (slow) ground-state alpha-particle emissions. So far, they have been identified by large high-resolution recoil spectrometers to detect the residual nucleus and the measurement of the energy and type of the subsequent decay particles. If the chain of decay particles ends in a known nucleus, the mass and nuclear charge of the original evaporation residue can be reconstructed.

This approach was successfully applied in fusion studies which produced the new elements from $Z = 107$ to 113 [58]. However, this method no longer works if the decay of the evaporation residues end in unknown residual nuclei which decay by spontaneous fission, as is the case for the recently discovered new elements $Z = 114$ to 118 [66]. In this case an independent verification of mass and nuclear charge of the fusion products seems mandatory.

Detection of characteristic γ-rays is in principle an elegant method for the identification of the fusion evaporation residue. Unfortunately, for exotic nuclei, the energies of the γ-rays are often not known so a different approach to identify them is needed. One alternative represents the measurements of their prompt characteristic K_x-rays which originate from internal conversion of electromagnetic transitions. Moseley's law gives a good approximation of their characteristic energies which are thus rather well known. In addition, the contribution of K_x-ray-yields of the evaporation residues arising from atomic collision processes is small [25].

Theoretical considerations provide estimates for the multiplicities M of K_x-rays in the deexcitations of the evaporation residues as a function of mass number A. For the heavier nuclei these are quite significant. Hence, this method allows the determination of the cross section from the number of measured K_x-rays and in particular the identification of the nuclear charge of the isotope is derived from the energy of the K_x-rays. In the framework of the present thesis we extend the systematics of K_x-multiplicities to assess its benefits

for the determination of the formed evaporation residues. Therefore we investigate the K_x-multiplicity of one medium heavy isotopee whose nuclear structure depends on the number of neutrons and perform an experiment with heavy evaporation residues whose level schemes are almost unknown.
Despite of the expected high multiplicity for super heavy elements ($M > 3$, [60]) one has very little cross section, i.e. of the order pico-barn, which thus requires very intense beams (approx. 1 particle-μAmp). However, then the rate of γ-decays from fission produce such a large background in the γ-ray detectors that in-beam spectroscopy is hardly possible. A reduction of fission γ-rays might be achievable by exploiting the angular distribution of the fission and fusion products. An appropriate shielding which suppresses more photons from the fission than from the fusion is supposed to reduce the background and to increase the contribution of fusion γ-rays in the spectra.
The experiments were performed at the Maier- Leibnitz- Laboratory with a newly constructed setup, consisting of four MINIBALL-detectors. The accelerator has of course too little energy to perform super heavy elements experiments. However, the experiments are sufficient to test the setup and to provide results which are the basis for further investigations.
After a discussion of the underlying physics in chapter 1, the experimental setup and basic analysis concepts which are an important part of this thesis, will be described in detail in chapter 2. The processing of the data enables us to compare two types of analysis to determine the multiplicity which will be presented in chapter 3. Different results on medium mass systems for different analysis methods in chapter 4 require interpretations and further discussions. Chapter 5 is devoted to the issue identifying heavy isotopes due to their characteristic radiations. A new shielding design to reduce fission background at fusions with heavy nuclei in the last chapter 6 give reasons to optimism.

Chapter 1

Physics Foundations

The first fusion experiments beyond the transuranium elements used proton induced reactions or captured neutrons in long-term irradiations in high-flux nuclear reactors. With this method, the nuclei are successively enriched until the element is formed. However, due to the competition between the n-capture and the decay of the nuclei, this method ends with the very short living ^{258}Fm ($\tau_{1/2} = 0.38$ ms).
To go beyond, fusion of two heavier nuclei can be used. High energy beams are then necessary to overcome the strongly increasing Coulomb barrier. This in turn leads to higher excitation energy of the compound nucleus and a sequence of particle emissions or fission is the consequence. Nevertheless, using heavy ion fusion, the synthesis of heavier elements up to $Z = 118$ were produced. Two main types of reactions can be distinguished, the so-called *cold* and *hot fusion*. For cold fusion, ^{208}Pb and ^{209}Bi are used and help to synthesize elements up to $Z = 113$ [58]. Heavier elements were obtained using the hot fusion which is based on actinide targets.
Fig. 1.1 illustrates the fusion process. Two nuclei merge together and form a highly excited *compound nucleus* which exhibits lots of angular momentum and energy. The nucleus gets rid of them by evaporation of charged and non-charged particles. They carry away parts of the spin and energy. If the remaining energy is no longer sufficient to evaporate particles one refers to an *evaporation residue*. The residual energy is emitted by γ-rays and *internal conversion*. The latter term is explained in detail in section 1.3. We briefly introduce the term which is the de-excitation via emission of electrons from the K-shell. Subsequently, characteristic K_x-ray radiation occurs when the vacancy in the shell is filled by an electron from a higher atomic shell.

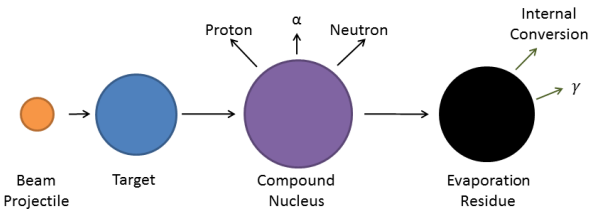

Figure 1.1: Principle of fusion of the beam projectile with the target. A highly excited compound nucleus is formed which de-excites by particle evaporation. The final nucleus, the so called evaporation nucleus de-excites by γ-decays and internal conversion.

The theoretical part tries to predict how often internal conversion takes place in depen-

dence on the residue's mass. The term *multiplicity* is defined by the number of K_x-rays which result from internal conversion during the de-excitation of evaporation residues.
This chapter explains the steps, leading to the predicted multiplicity. The fusion process is the starting point of the considerations. We give an overview of macroscopical and microscopical approaches. The end of this section is the formed evaporation residue. The next section 1.2 pursues the issue which shape is adequate to describe the excited nucleus. Further sections treat processes which have influence on the multiplicity. Finally, section 1.6 connects the relevant processes and gives a prediction of multiplicity.

1.1 Fusion

1.1.1 Classical Concept

The fusion of two atomic nuclei can be described by a macroscopical model. The potential V of the interaction is composed of the three parts: A Woods-Saxon shape attractive nuclear part, a repulsive Coulomb and a centrifugal potential. Fig. 1.2 shows the summed potential which besides its dependence on the distance R between the two nuclei also reflects the orbital angular momentum l. As long as l is smaller than a certain l_{max} which is inversely proportional to the product of the number of protons of the colliding nuclei, $Z_1 Z_2$, [27] the potential shows a pocket i.e. a local minimum. Its depth indicates the probability that two nuclei with centre of mass energy E_{cm} are a sufficient long time at close distance so that a compound nucleus up to a maximum spin l_{max} can be formed.
A brief statement should be added here to be complete: Even a beam energy which is above the fission barrier for a certain l_{max} is no guarantee for fusion since the spin of the compound nucleus itself depends on the deformation of the two interacting nuclei at the collision and that in turn relys on the distance between the mass centres of the colliding nuclei. So, if the beam energy is insufficient during the production process an extra push for the two merging nuclei would have been necessary to jump over the fission barrier and to form a compound nucleus. Bjornholm [8] specified following expression for this push:

$$E_{push} = 200(x_e - 0.7)^2 MeV \tag{1.1}$$

where the parameter x_e depends on the number of neutrons and protons and on the spin l of the compound nucleus. The exact expression can be found e.g. in [27].
Fig. 1.2 shows that a compound nucleus cannot be formed if its spin l_{max} increases to arbitrary height. Cohen, Plasil and Swiatecki [17] found a connection between maximum spin l_{max} of the compound nucleus and the fission barrier. They calculated the stability of charged rotating nonviscous liquid drops. Fig. 1.3 gives limitations for the maximum angular momenta in dependence on the fission barrier. The maximum angular momentum, the compound nucleus can absorb before it fissures has a maximum at $A \approx 130$ and decreases both at lower and larger number of nucleons. While classically, light nuclei cannot carry too much spin due to their reduced mass and moment of inertia, increased Coulomb repulsion for the heavy nuclei leads to reduced stability at large angular momentum. Fission can be avoided if the highly excited compound nucleus releases particles which carry away a part of the excess. The dashed line in Fig. 1.3 represents the requirement for a fission barrier of at least 8 MeV which is approximately the binding energy of a neutron. Along this dashed curve the probability for neutron evaporation is comparable to fission.

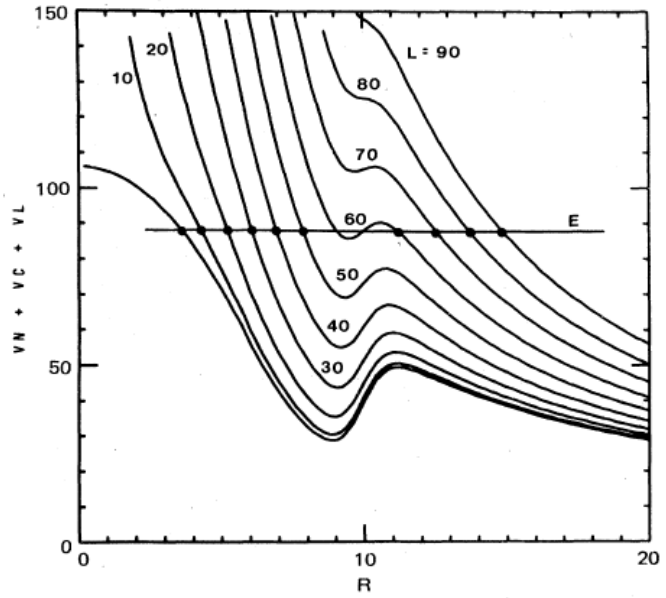

Figure 1.2: Fusion potential composed of Woods-Saxon, Coulomb and centrifugal potential. The depth of the potential pocket reflects the probability for fusion of the two colliding nuclei, the local maximum the fission barrier. For very large angular momentum l the pocket vanishes and no fusion is possible. *From* [29]

This is called a pre-compound or multistep compound reaction. Often this is necessary to get trapped in the pocket and thus, the only way to get two nuclei forming an *evaporation residue*.

1.1.2 Level Density and Transmission Coefficient

An evaporation residue is formed from an non-equilibrated system, i.e. from the compound nucleus, and the subsequent (statistical) decay via particle- and/or γ-ray emission. The flow of an evaporation cascade is determined by the spin dependent level densities and the transmission coefficients. The first quantity describes the available phase-spaces, the second assigns the fraction for each phase space of a decay.
The level density relates to the degrees of freedom in deformation and excitation energy. For this purpose, we consider the nucleus in more detail. Pauli postulated the exclusion of fermions occupying the same state i.e. each nucleon must differ in at least one quantum number. At zero temperature and without interactions single particle states are filled from the ground state successively and since in one state two spin orientations are possible each state is filled with two nucleons. Protons and neutrons are treated independently since they differ in iso-spin quantum number. The highest occupied state constitutes the surface. This concept was first proposed by Enrico Fermi and is known as Fermi Gas Model. Introducing excitations means to promote nucleons from their ground states into unoccupied states above the Fermi surface. The more particles are excited, the more compositions are possible to reach the same excited state which let the level density raises exponentially. For protons and neutrons one finds for the density of states at excitation energy E [85]:

$$\rho(E) = \frac{1}{12a^{1/4}E^{5/4}} \exp(2\sqrt{aE}) \tag{1.2}$$

where a is the level density parameter and the standard input for the level density param-

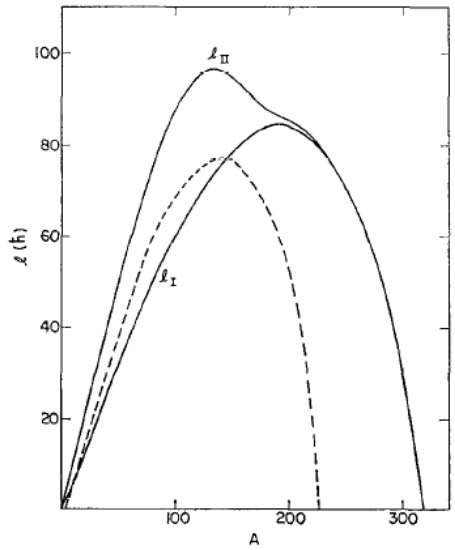

Figure 1.3: Cohen et al. [17] calculated the fission barrier influence on the maximum spin l_{II} in their model of a charged nonviscous liquid drop. The dashed line corresponds to the maximum spin under the condition of a fission barrier of $\approx$ 8 MeV. l_I is not of interest to this thesis. *From* [17]

eter is $a = \frac{1}{8}A\ MeV^{-1}$.
Assuming only rotational excitations the total energy E corresponds to E_{rot}. The level density parameter a is suggested to be proportional to the number of nucleons A. Thus, in first approximation one gets an A-dependence for the level density:

$$\rho(E) \propto A^{11/6} \tag{1.3}$$

However, in most cases this assumption is too simple and several correction parameters have to be included. In particular, two such corrections should be noticed. First, the temperature dependence which was omitted resp. fixed at zero, has to be added. Then, a pairing correction $\triangle$ is necessary to consider the interactions between nucleons which causes changes in the relative positions of individual levels [85].
The information of which fusion product will be formed depends on the transmission coefficient T_l. The value of this parameter permits comparisons with measured cross sections. The Schroedinger equation is the initial point to determine theoretical fusion cross sections. Known from scattering theory lectures [28] and from [33], the nucleon's total wave function can be written as

$$\psi(\vec{r}) = \sum_{l=0}^{\infty} \frac{u_l(r)}{r} P_l(\cos\vartheta) \tag{1.4}$$

where $u_l(r)$ is the radial-component of the wavefunction and $P_l(\cos\vartheta)$ represents the Legendre-functions. The Schroedinger equation has the form:

$$[-\frac{\hbar^2}{2\mu} \triangle + V(r) - iW(r) - E]\psi(\vec{r}) =$$

$$[-\frac{\hbar^2}{2\mu}(\frac{d^2}{dr^2} + \frac{2}{r}\frac{\partial}{\partial r}) + \frac{\mathbf{L}\hbar^2}{2\mu r^2} + V(r) - iW(r) - E]\psi(\vec{r}) = 0 \tag{1.5}$$

with **L** as the angular momentum operator. If V is the above mentioned potential and if a purely radial imaginary part W is added for absorption, then the angular part of the Schroedinger equation can be separated and depends only on the radius:

$$[-\frac{\hbar^2}{2\mu}\frac{d^2}{dr^2} + V(r) - iW(r) + \frac{l(l+1)\hbar^2}{2\mu r^2} - E]u_l(r) = 0 \tag{1.6}$$

The radial-component of the wavefunction $u_l(r)$ is the sum of a regular and a irregular solution of Equ. (1.6). Putting these solutions into the total wavefunction $\psi(\vec{r})$ (Equ. (1.4)) one can distinguish between incoming and outgoing wavefunctions defined by the wave number $\vec{k}$ and $\vec{k'}$. The relative ratio $f(\vec{k}, \vec{k'}) = (f(\vartheta)$ is written as

$$f(\vartheta) = \sum_{l=0}^{\infty} \frac{2l+1}{k} \sin\delta_l e^{i\delta_l} P_l(\cos\vartheta) \tag{1.7}$$

with $\delta_l = S_l(k)$ as the scattering phase and $P_l(x)$ are the Legendre-polynomials.
Under the condition of a well-defined W within the Coulomb-barrier the total fusion cross section σ_{fus} is calculated via the optical theorem

$$\begin{aligned}\sigma_{fus}(E) &= \frac{4\pi}{k}\Im f(\vartheta = 0) \\ &= \frac{\pi}{k^2}\sum_l (2l+1)(1 - |S_l|^2)\end{aligned} \tag{1.8}$$

The quadratic transmission can be approximated by $T_l^2 = 1 - |S_l|^2 = P_{l=0}[E - \frac{l(l+1)\hbar}{2\mu R_b^2}]^{-1}$ (R_b is the region up to the Coulomb barrier). ([33], Equ. B 3)

1.1.3 Subbarrier Fusion

Experimentally, fusions at energies below the Coulomb barrier have been observed. These go beyond simple basrrier penetration models and are called enhanced subbarrier fusion. A brief explanation is given based on the discussion in [33].
The ansatz so far was based on calculations with structureless mass points. Although, nuclei are often modeled isolated from their environment, in quantum mechanical calculations of nuclear reactions one has to include the couplings of the colliding nuclei and their nucleons. Starting point are low-lying collective excitations of the colliding nuclei during fusion. In the following, it will be shown that the interaction of heavy ions below the Coulomb-barrier can be well reproduced. The first correction to the previous macroscopical approach concerns rotational excitations. Introducing the angle θ between the symmetry axis of the compound nucleus and the beam direction, following from a redefined deformed Woods Saxon potential, the formula for the angle integrated fusion cross section of an axially symmetric target nucleus is given by

$$\sigma_{fus}(E) = \int_0^1 d(\cos\theta)\sigma_{fus}(E;\theta) \tag{1.9}$$

with an angle dependent cross section $\sigma_{fus}(E;\theta)$. Due to the deformation effect and the attractive nuclear interaction the potential is lowered at $\theta = 0$ and increased at $\theta = \pi/2$ compared to the spherical nucleus. As known from quantum mechanics, the tunneling

probability decreases exponentially with barrier height. This extended macroscopic approach explains subbarrier fusion partly. A considerable improvement of the model is achieved by a more microscopic description of nuclear structure effects. The coupled channel method formulates the collision of two nuclei taking into account coupling in the Hamiltonian:

$$H(\mathbf{r},\xi) = -\frac{\hbar^2}{2\mu} \bigtriangledown^2 + V(r) + H_0(\xi) + U_{coup}(\mathbf{r},\xi) \tag{1.10}$$

where $\mathbf{r}$ is the distance between the two nuclei and with $H_0(\xi)$ as intrinsic Hamiltonian for which applies [33]:

$$H_0(\xi)\psi(\xi) = \epsilon\psi(\xi) \tag{1.11}$$

where ψ corresponds to the wavefunction whose radial part solves the Schroedinger equation of the intrinsic Hamiltonian, Equ. (1.6).
To make clear, where the coupling happens, we label the parameters of the original wave function with α and that of the coupled one with α'. In analogy to Equ. (1.4) the total wave function can be decomposed in radial and angle dependent parts. Proper transforming leads to the radial coupled-channel equation [33]

$$[-\frac{\hbar^2}{2\mu}\frac{d^2}{dr^2} + \frac{l(l+1)\hbar^2}{2\mu r^2} + V_\alpha(r) - E + \epsilon_\alpha]u_\alpha(r) + \sum_\alpha U_{\alpha;\alpha'}(r)u_{\alpha'}(r) = 0 \tag{1.12}$$

Using adequate incoming wave boundary conditions the result for the fusion cross section can be expressed as

$$\sigma_{fus}(E) = \frac{\pi}{k^2}\sum_k (2J+1)T_l^2(E). \tag{1.13}$$

Of course the penetrability T_l^2 does not conform to Equ. (1.8) but contains channel coupling effects. This approach has provided a suitable method to replicate experimental data.

1.1.4 Time Scale and Angular Distribution of the Evaporation Residues

The basic condition for the formation of compound nuclei is that the *relaxation time* τ_n, i.e. the time nucleons need from their starting point of random distributions to an equilibrated state of the compound nucleus, is shorter than τ_{app} which is the time the system needs to penetrate to the minimum of the potential V_{min}, i.e. to the pocket. Kumar et al [48] calculated τ_n depending on the entrance channel. The authors could show that fusion of rather symmetric nuclei, in their case ^{31}P+^{27}Al, takes twice the time as the fusion of asymmetric systems e.g. ^{12}C+^{46}Ti to compose the same compound nucleus. The formation of an intermediate, temperature equilibrated di-nuclear complex was seen as causing this difference [48]. The di-nucleus is formed at $V > V_{min}$ and the potential difference $\triangle V = V - V_{min}$ acts as new interaction. As a consequence, fast fission or deep inelastic scattering is likely for such complexes [27].
A distinction of the products in compound nucleus formation and fission resp. deep inelastic reactions is achieved with the help of their different angular distributions. For the decays of the compound nuclei into evaporation residues and particles, following considerations can be made:

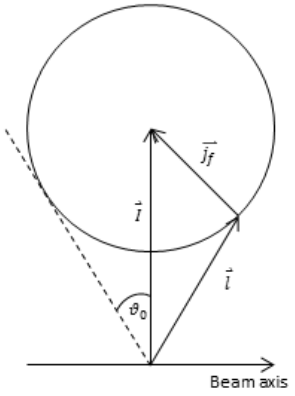

Figure 1.4: Coupling of angular momentum vectors in the case of a 0 spin target. From [23]

For zero spin targets, the angular momenta of the compound nuclei $\vec{I}$ are defined by the orbital angular momenta of the beam and are perpendicualar to the beam direction. The evaporation of particles splits the momenta. One part stays at the residue, the rest is transferred to emitted particles. The distribution of the residue's spin $\vec{j_f}$ has no restrictions and the direction is arbitrary around the end of $\vec{I}$. Conservation of angular momentum requires a connection between the length of the vector $\vec{j_f}$ with the restricted direction of the angular momentum $\vec{l}$ of the particle by $\vec{l} = \vec{I} - \vec{j_f}$. Fig. 1.4 illustrates the conditions; $\vec{l}$ must end on the sphere of radius j_f. Ericson [23] defined the maximum angle of decoupling between $\vec{l}$ and $\vec{I}$ by

$$\sin \vartheta_0 = \frac{j_f}{I}. \tag{1.14}$$

Under the assumption of complete alignment of $\vec{l}$ and $\vec{I}$, the angular distribution is obtained by integration over the possible orientations $\vec{I}$ [23], [27]

$$\frac{d\sigma}{d\Omega} \sim \frac{1}{2\pi} \int_0^{2\pi} \delta(I \sin \vartheta_0 \cos \phi) d\phi = \frac{1}{2\pi I \sin \vartheta_0} \tag{1.15}$$

This $1/\sin \vartheta_0$ behaviour has been experimentally confirmed, with exception around $\vartheta = 0$ and $\vartheta_0 = \pi$, where it is undefined. Ernst et al. [25] measured the cross section $\frac{d\sigma}{d\Omega}$ in the laboratory frame for the fusion of sulfur with tin isotopes. Integrated over the azimuthal angle ϕ they determined $\frac{d\sigma}{d\Omega}$ which exhibits a maximum of evaporated residues at $\theta_{lab} \approx 3^\circ$ with a long tail extending up to $\theta_{lab} \approx 10^\circ$, see Fig. 1.5. We expect similar cross sections for our experiments.
Different calculations are based on this statistical model. In the present work, PACE4 [53] was used.

1.2 Models of Nuclei

K_x-ray multiplicity occurs during the γ-decay of the evaporation residue. At the end of this chapter we present data from previous experiments which indicate that the multiplicity depends from the mass of the evaporation residue. So, we have to understand different processes during the de-excitation of the nucleus. The condition for adequate descriptions of the decay is based on assumptions of the shape and de-excitation modes. Therefore we clarify the starting point for further aspects, i.e. we present two models for the evaporation residue. Both models come from geometrical consideration of a nucleus. The vibrational model is applicable for almost spherical shapes and assumes collective behaviour in nuclei without considering internal interactions and is introduced as an approach for describing excitations of deformed nuclei. This is the basis for the rotational model which takes rotations, excitations, collective and individual particle motions into account to calculate the transitions between the excited states with regard to the nuclei's mass.

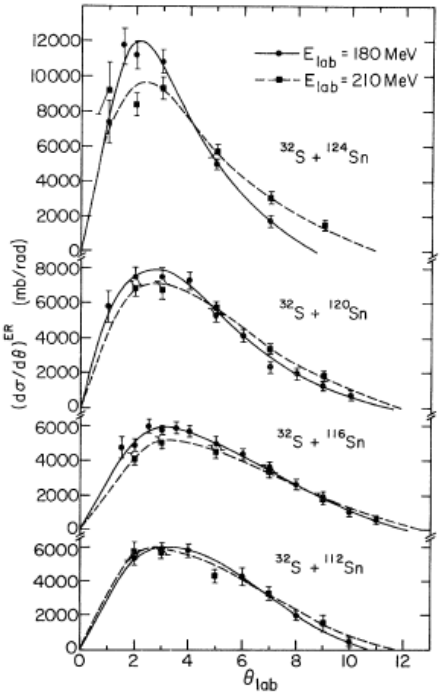

Figure 1.5: Differential cross sections for the fusion of sulfur with various tin isotopes. A maximum at $\theta_{lab} \approx 3^\circ$ for all reactions can be observed. θ_{lab} defines the angle between beam direction and direction of the nucleus. *Data from* [25]

1.2.1 Vibrational Model

The fundamental idea of the vibrational model is to consider the nucleus as spherical in its ground state and the interactions of the nucleons as contribution in form of collective oscillations. Deviations in shape are expressed in the form of stable and permanent deformations. Using spherical harmonics $Y_{2\mu}(\theta, \phi)$ the simplest change from a spherical shape is obtained by static quadrupole deformations:

$$R = R_0[1 + \sum_{\mu} \alpha_{2\mu}(t) Y_{2\mu}(\theta, \phi)] \tag{1.16}$$

where $R_0 \propto A^{1/3}$ represents the average radius and the parameter $\alpha_{2\mu}(t)$ constitutes the time dependent quadrupole distortion of the nuclear surface vibrations [30]. Depending on the parameters there are three possible shapes for a quadrupole deformed nucleus. It can be prolate i.e. the nucleus is extended in one direction and squeezed in the other two, or its shape is oblate, i.e. there are two directions extendend and one is squeezed. The last possible choice is a triaxial shape, i.e. all directions are different [16].
A convenient formulation of excitations of nuclei is done with the concept of phonons. They are treated like bosons, i.e. their wave functions must be total symmetrical and the parities are even. Their creation and destruction can be expressed by operators. For such quadrupole distortions the time dependent Hamiltonian H results in

$$H = E_0 + \hbar\omega \sum_{\mu} \mathbf{b}^{\dagger}_{2\mu} \mathbf{b}_{2\mu} + \frac{1}{2} + \sum_{L} C_L [\mathbf{b}^{\dagger}_2 \times \mathbf{b}^{\dagger}_2]^{(L)} \cdot [\mathbf{b}_2 \times \mathbf{b}_2]^{(L)} \tag{1.17}$$

where $\mathbf{b}^{\dagger}_2$ and $\mathbf{b}_2$ correspond to the creation and annihilation of a quadrupole vibration [16]. The equation of motion of such a Hamiltonian is the known harmonic oscillator

equation and the energy levels E of nuclei where the model is applicable are therefore the solution of the 5-dimensional oscillator:

$$E = \hbar\omega(N_{ph} + 5/2) \tag{1.18}$$

with N_{ph} as the number of quadrupole phonons. The third term is neglected under the assumption of a purely harmonic vibrational spectrum [16].

1.2.2 Rotational Model

For some nuclei the framework of the vibrational model, which describes the collectivity for weakly deformed nuclei as a surface-vibration is a quite good approximation. Nevertheless, this assumption turns out to be inadequate for a large range of nuclei. An improvement is achieved by taking into account rotational motion in the laboratory system ([16], *p.202*).
So far we neglected rotations for one reason: In quantum mechanics rotations around symmetry axes do not change the quantum mechanical state. However, when considered in more detail there is not only vibration coming from the surface but also from movements of each nucleon inside the nucleus. A first approximation includes these rotations with the adiabatic ansatz. For this purpose, no coupling between the very slow outside, collective frequence ω_{coll} and the much faster intrinsic frequence ω_{intr} is assumed [47]. Thus, the total wave function separates in a collective function and an intrinsic one:

$$\psi = \phi_{coll}\ \chi_{intr} \tag{1.19}$$

In the simplest case the axial symmetric nucleus can be limited to the ground state where all states are occupied in the same way. Furthermore, rotation should have equal frequency around the x or y axes. With these restrictions one gets the rotational Hamiltonian

$$\hat{H} = \frac{\hbar^2}{2I}\mathbf{R}^2. \tag{1.20}$$

The parameter I indicates the moment of inertia and $\mathbf{R}$ the rotational angular momentum operator. Section 1.3 shows that internal conversion is found predominantly for low energy transitions. Such transitions are expected to have low-lying, low spin states. Under these conditions and the assumption that the quantum numbers of the ground state for even-even nuclei are $J^\pi = 0^+$ and $K = 0$, the total angular momentum is equal to the rotational angular momentum i.e. $\mathbf{J} = \mathbf{R}$. In the case of an even-odd nucleus we assume the odd nucleon to be in a single j-orbit and not to polarize the residual even-even nucleus. Hence, the total angular momentum is the vector sum of the single j-vector and the rotational angular momentum J: $\mathbf{R} = \mathbf{J} - \mathbf{j}$. Solving the corresponding Schroedinger equation with the above mentioned Hamiltonian, equ. (1.20)

$$\hat{H}\psi = i\hbar\frac{\delta}{\delta t}\psi, \tag{1.21}$$

multiplying with $< \psi|$ and making use of equ. (1.19) gives the rotational energy of the ground state for the even-even nuclei

$$E_{rot}(J) = \frac{\hbar^2}{2I}J(J+1) \tag{1.22}$$

and for even-odd nuclei

$$E_{rot}(J) = \frac{\hbar^2}{2I}(J(J+1) + j(j+1) - 2\mathbf{J}\cdot\mathbf{j}). \tag{1.23}$$

A significant quantity is the moment of inertia

$$I = \frac{2}{5}AMR_0^2(1 + 0.31\beta) \propto A^{5/3}. \tag{1.24}$$

with β describing the extent of the quadrupole deformation. The intrinsic quadrupole moment of the ellipsoidal shape is given by

$$Q_0 = \frac{3}{\sqrt{5\pi}}ZR_0^2\beta(1 + 0.16\beta). \tag{1.25}$$

Experimental energy levels of nuclei with $150 < A < 190$ and $A > 230$ show impressive agreements with the ratio $E(4^+)/E(2^+) = 3.33$ [45]. The projection of the intrinsic angular momentum J_{intr} onto the symmetry z-axis is denoted as K; the total angular momentum then is the combination of nuclear rotational motion and the projection K.

$$J = K, K+1, K+2, ... \text{ or } J = 0,\ 2,\ 4, ... \text{ for } K = 0$$

The rotational energies relative to its ground state (equ. (1.27)) for even-even nuclei are given by [16]

$$E_{rot}(J) = \frac{\hbar^2}{2I}[J(J+1) - K(K+1)] \tag{1.26}$$

and for odd-A nuclei we define a Coriolis energy so that the energy results in

$$E_{rot}(J) = \frac{\hbar^2}{2I}[J(J+1) - 2K^2 + \langle\mathbf{j}^2\rangle] + V_{Coriolis}. \tag{1.27}$$

E_{rot} can be interpreted as rotational energy inside an excited intrinsic state with angular momentum J_{intr}. Each projection K generates a rotational band. The transitions between states within a *band* are intense electric quadrupoles $(E2)$ whereas separations between single bands are weak magnetic dipoles $(M1)$ [38]. One speaks about a band if the projection K is fixed and the intrinsic angular momentum J_{intr} is variabel.
For our further investigation we keep in mind a proportionality which should prove to be important. With equ. (1.24) the transitions between low lying states, equ. (1.27) show proportionality to the number of nucleons in the nucleus:

$$\triangle E \propto A^{-5/3} \tag{1.28}$$

1.3 Internal Conversion

If the compound nucleus has no longer sufficient energy to emit particles, the still highly excited evaporation residue can only decay via electro-magnetic transitions. This happens in two ways: One is γ-ray emission, the other is the process of internal conversion. The latter refers to an interaction of electro-magnetic fields with an atomic electron from the K-shell in such a way that the electron absorbs the energy and leaves the atomic shell. Within atomic time scales (10^{-14}sec to 10^{-17}sec) [25] an electron from a higher shell fills

the vacancy which is accompanied by the emission of an K_x-ray. The new shell requires less binding energy of the electron than it was necessary in higher shells. The residual energy is emitted by a γ-ray. As the total nuclear decay time is much longer ($> 10^{-9}$sec) thus, in principle there could be emission of more than one electron of the K-shell during the de-excitation of the evaporation residue.
For the further discussion one is only interested in the most abundant case i.e. in emitting K_x-rays with energies due to Moseley's law, see appendix A.
As a consequence the total decay probability λ_{total} consists of two components

$$\lambda_{total} = \lambda_\gamma + \lambda_e. \tag{1.29}$$

λ_γ is the probability of a decay via photon emission and λ_e refers to the decay probability due to internal conversion. A general definition of λ is given in equation 1.36.
The ratio between the transition probabilities of the two kinds of de-excitation can be outlined in the following way. Although it does not behave like a two-step process but indeed is a direct transfer of the electromagnetic field's energy to the electron, for pure theoretical reasons the internal conversion is often explained by a virtual photon. The source of the radiation fields results from the multipole operator

$$m_{fi}(\sigma L) = \int \psi_f^* \, m(\sigma L) \, \psi_i d\nu \tag{1.30}$$

which describes the transition between the nuclear states which wave function's ψ_i and ψ_f, integrated over the volume of the nucleus. Simultaneously a photon with the proper energy, parity and multipole order is created [45]. In contrast to γ-transitions, for the description of internal conversion an add-on is necessary that includes the wave function ψ_{i_e} of the electron, too, namely

$$\psi_i = \psi_{i_N} . \psi_{i_e} \tag{1.31}$$

Since the states of the nucleus and of the atomic shell are separated, the first term ψ_{i_N} indeed contains all nuclear information so both kinds of de-excitation exhibit the same nuclear part of the operator.
The decay-probability λ is proportional to the squared multipole operator

$$\begin{aligned} \lambda_\gamma(\sigma L) &\propto |m_{fi}(\sigma L)|^2 \\ \lambda_e(\sigma L) &\propto |m_{fi}(\sigma L)|^2. \end{aligned} \tag{1.32}$$

It should be stated here that λ_e itself is the sum of the decay probabilities into different shells. We will soon see that the probability for internal conversion into higher lying shells goes with $1/n^3$ and gets progressively irrelevant. The decay ratio of excited states via γ-rays or internal conversion is obtained by the internal conversion-coefficient

$$\alpha = \frac{\lambda_e}{\lambda_\gamma} \tag{1.33}$$

In non-relativistic calculations one distinguishs between electric (E) and magnetic (M) multipoles and their expressions are given by [45]

$$\alpha(EL) \cong \frac{Z^3}{n^3}\left(\frac{L}{L+1}\right)\left(\frac{e^2}{4\pi\epsilon_0\hbar c}\right)^4\left(\frac{2m_e c^2}{E}\right)^{L+5/2}$$

$$\alpha(ML) \cong \frac{Z^3}{n^3}(\frac{e^2}{4\pi\epsilon_0\hbar c})^4(\frac{2m_ec^2}{E})^{L+3/2} \tag{1.34}$$

They exhibit the following characteristics:

1. The increase is strongly influenced by the number of protons within the nucleus, namely Z^3. Excited states of heavy ions show a higher probability to decrease by internal conversion.
2. With increasing transition-energy the internal conversion-coefficient drops rapidly $(1/E^{L+const})$.
3. The higher the multipole order L the larger is the internal conversion-coefficient.
4. Electrons of higher lying atomic shells n are less likely to participate in internal conversion with the probability, scaling as $1/n^3$.

A further feature of internal conversion is the probability of a nucleus to decay by $E0$-transition, a situatio which does not allow γ-emission. This is important for decays of 0^+-states into likewise 0^+-states.
Experiments [42], [37] suggest strong $M1$-transitions between rotational bands. At last we give the probability P_{IC} for internal conversion during one cascade. Under the assumption of $\alpha \ll 1$ and $M1$-transitions it is simply

$$P_{IC} = \frac{\lambda_e}{\lambda_{tot}} = \frac{\lambda_e}{\lambda_e + \lambda_\gamma} = (1+\alpha^{-1})^{-1} \propto \alpha \propto Z^3 \cdot E^{-2.5} \tag{1.35}$$

1.4 Transition Probability

Decays of excited states include squared multipole operators which can be seen as perturbations in the Hamiltonian. They allow us to obtain the internal conversion-coefficient, in Equ. (1.34). We now want to add an application of multipole operators. The transition rate of the compound nucleus can be calculated with them; it is based on the principle of the *Fermi's Golden Rule* which is applied to many fields in atomic processes and treats spontaneous conversions resulting from radioactive decays or emission of photons. In the latter case the multipole operator, Equ. (1.30), is nothing else than a perturbation function $m(\sigma L)$ that transfers the initial state with its wave function ψ_i into another final state. A further factor is the phase space ρ which describes the density of the final excited states *f*. Without derivation that can be found, e.g. in [83], one obtains this concrete expression for the cross section per unit time, expressed in first order, by Fermi's Golden Rule

$$\lambda = \frac{2\pi}{\hbar}|m_{fi}(\sigma L)|^2\rho \tag{1.36}$$

where ρ is the final state level density from section 1.1, Equ. 1.2. This equation justifies now the proportionality of Equ. 1.32. For the further studies we conclude

$$\rho \propto (a \cdot E^5)^{-1/4} \propto A^{11/6} \Rightarrow \lambda \propto A^{11/6}, \tag{1.37}$$

i.e. there is an $A^{11/6}$ dependence on transitions. Since the reciprocal value corresponds to the mean lifetime of an excited state one concludes that for heavier nuclei the lifetime decreases and hence more transitions per unit time occur.

1.5 Fluorescence Yield

The principle of internal conversion (section 1.3) is the transition of discrete energy of electromagnetic fields to an electron which comes mostly from the K-shell. The electron emits and the vacancy will be filled by an electron from a higher lying shell. Due to the lower binding energy, K_x-rays are emitted which are characteristic for each isotopee.
However this K_x-ray is not necessarily measurable by γ-detectors. There is the phenomenon of non radiative emission in which the photon transfers its energy to another electron that changes the shell or leaves the atom. This process is known under the term Auger Effect [14].
This effect is crucial for the so called fluorescence yield of the detectable radiative K_x-rays. It gives the probability for detecting γ-rays and is defined as

$$\omega_k = \frac{P_{rad}}{P_{rad} + P_{Aug}}. \tag{1.38}$$

The simplest assumption is that of a Z independent Auger-probability $P_{Aug} = C$ and a Z^4 proportional probability for radiative emission $P_{rad} = R\,Z^4$ [14]:

$$\omega_k = (1 + \frac{\alpha}{Z^4})^{-1}. \tag{1.39}$$

with $\alpha = C/R$ and R and C are constants.
In Fig. 1.6 are drawn experimental values together with the above indicated formula. One recognizes that the description is quite good. More specific calculations under relativistic aspects give similar results and prove the denoted dependence.

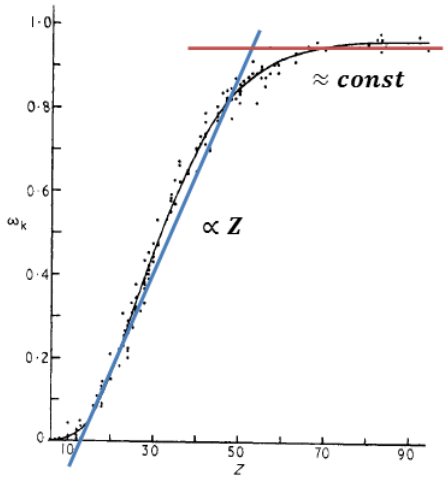

Figure 1.6: Best fit at experimetal data for the fluorescence yield. *From* [14]

From Fig. 1.6 we conclude that for the approximate region $15 \leq Z \leq 60$, ω_k increases more or less linearly with Z, i.e.

$$\omega_k \approx Z \tag{1.40}$$

and then quickly saturates for large Z to a constant value close to one:

$$\omega_k \approx 1 - Z^{-4} \approx 1 \tag{1.41}$$

With regard to the nuclei we study, the non radiative effect has little influence. Most of the K_x-rays leave the atom.

1.6 Multiplicity of K_x-Rays

In the last sections we presented several models and relevant parameters for fusion processes. Here comes a summary of the results. Heavy nuclei can be described by the vibrational model where rotations are included. Even almost spherical nuclei tend to rotational behaviour in high energy as suggested by [38]. Furthermore, there is a connection between the energy of the excited state with the number of involved nucleons. Also the level density of excited states depends on the mass of the nuclei and hence the transition probability relies to it, too. We saw that internal conversion occurs more and more for heavy ions where transition energies between excited states are small. Finally it was of interest how many K_x-rays leave the atom. This probability is given by the fluorescence yield.

With a further approximation, $Z \approx \frac{1}{2}A$, one gets in summary:

Rotational excitation (section 1.2 Equ. 1.28): $E_{rot} \propto A^{-5/3}$

Fluorescence yield (section 1.5):

for $15 \leq Z \leq 60$, Equ. 1.40: $\omega_k \propto Z \ \widetilde{\propto} \ A$

and for $Z \geq 60$, Equ. 1.41): $\omega_k \propto 1$

Occurence of internal conversion (section 1.3 Equ. 1.35): $P_{IC} \propto Z^3 \cdot E^{-2.5} \widetilde{\propto} \frac{1}{2^3} A^3 \cdot A^{25/6}$

Transition Probability (section 1.4 Equ. 1.37): $\lambda \propto A^{11/6}$

From these relations it is seen that for a fixed transition energy E, the A-dependence is between A^3 and A^4. The first, A^3, for the heaviest nuclei where the fluorescence probability ω_k saturates to the constant value of one. A^4 for the mass region $15 \leq A \leq 60$ where ω_k is roughly linear with A.

Of course, since the transition energies decrease with $A^{-5/3}$, the multiplicity for the heavy region might increase as much as $\sim A^6$, but this would only be true if the internal conversion probability would not reach unit-value and saturates which it does for low energies. So, there is a cut-off and the more probable dependence is perhaps between A^3 and A^4. All these aspects depend on specific nuclear structure (as does the level density) and therefore considerable fluctuations should be expected around an average dependence near A^4.

Henning et al. [35] predicted under different aspects the multiplicity and suggested a similar proportionality:

$$M \ \widetilde{\propto} \ A^{4.5} \tag{1.42}$$

Previous experiments are quite convergent to the predicted line in Fig. 1.7. The plot shows the mass number against logarithmic scaled multiplicity. It gives also an indication which multiplicities are expected for super heavy elements. They are assumed to have at least two internal conversions during their decay cascades.

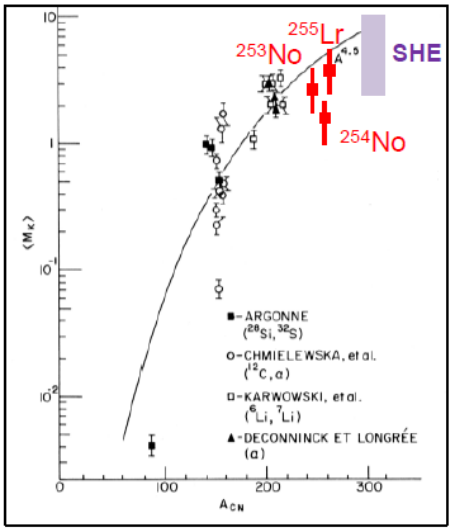

Figure 1.7: Systematics of multiplicity in measured data. *From* [35]

With the MINIBALL-detectors and a suitable setup we had the opportunity to perform experiments with isotopes of radon as evaporation residues. The data are analysed with different methods so that the results for the multiplicity can be compared with the existing data and furthermore, one can make statements attributed to the nuclear structure. Preliminary results for fusion reactions with heavy nuclei i.e. fusion to evaporation residues with $A > 220$, need further studies.

Chapter 2

Experimental Setup

Fig. 2.1 shows the setup for the experiments. Four MINIBALL- detectors surround a newly- designed chamber which was motivated by special challenges. The low K_x-rays energies have to emit trough the chamber wall with minimum absorption; furthermore the determination of the multiplicity relys on the correct counting of photons, originating from transtitions between low excited states. The centres of the detectors are directed on the target position and are symetrical with respect to the beam line. The detectors, labelled with 1 and 4, are positioned in backward direction, the detectors 2 and 3 in forward direction. The energy signals are transmitted to the electronics setup which converts the analog signals into digital ones.
The first section explains the design and inner lifes of the chamber. Informations about the used high-purified germanium detectors are summarised in section 2.2. The last part of this chapter is reseved for a detailed description of the electronics setup.

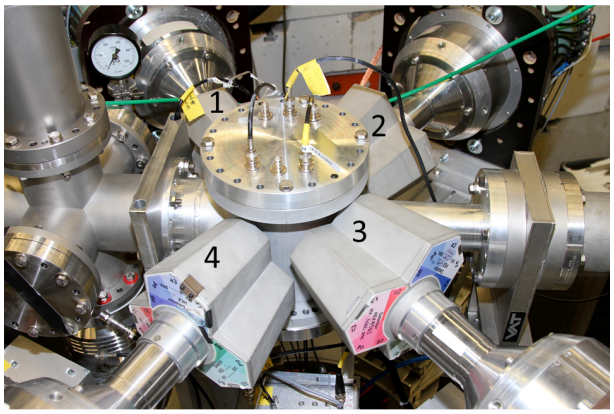

Figure 2.1: Detector array. The beamline is from left to right. The detectors are numbered clock-wise.

2.1 Detection Concept

The target chamber is a new design and optimized for K_x-ray experiments. The observable K_x-rays have low energies ($\leq$ 100 keV) and the challenge to get high measurement sensitivity is obtained by a thin wall thickness consisting of a material with low absorption coefficient. A suitable material was aluminium and the wall of the chamber was 2 mm thick. Most of the beam is elastically scattered at small angles and not stopped in

the thin target. On the opposite side of the beam entry an exit was mounted to prevent the detectors to be flooded with photons resulting from interactions between the beam and the wall of the chamber. Finally, the beam is stopped in a dump about three meters downstream.

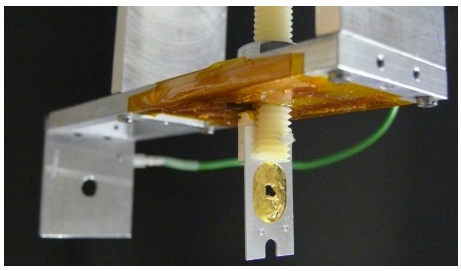

Figure 2.2: The target is positioned in the middle of the chamber. 10 cm behind it, an implantation plate was installed.

Fig. 2.2 shows the interior of the chamber. For the correct recording of decays of evaporation residues an implantation plate was mounted at a distance of 10 cm from the target which catches evaporation residues. A hole in the plate was necessary to let the beam pass and as a consequence also a part of the evaporation residues emits through it. Hence, only nuclei that deviate at least 1.2° from the beam direction can be implanted. This ensures that photons of evaporation residues are detected by the detectors and the whole spectrum is recorded. The effort is needed to catch transitions between low lying states especially for nuclei which have isomeric states. For the analysis of well documented evaporation residues we determine the number of produced evaporation residues by counting low lying transitions. To achieve this the level scheme with the isomer states has to be known and the angular distribution of the cross section is necessary.

2.2 MINIBALL Detectors

In the beginning of this century there was the necessity to develop new γ- detectors for two reasons: A nearly 4π apparatus should be created that is flexible to assemble further detectors like, e.g., a neutron detector in the setup. In addition, experiments which work with inverse kinematics require angle dependent photon energies. Therefore, one needs a spatially resolving detector [81].

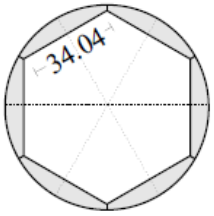

Figure 2.3: Shape and size of one of three crystals in a MINIBALL detector. *From* [81]

Arising from the first demand it follows that a classical 4π- germanium detector like EUROBALL must not be developed but many single detectors which cover together almost the whole solid angle. The MINIBALL setup consists of separated detectors and the complete setup how it is used at CERN has eight of them. With optimal alignment a space covering of 65% is reached. Our experiment has only four detectors which are positioned in a plane at the level of the target position. The surface of a detector S_{det} is three times the surface of the crystals S_{crys} which have hexagonal shapes, see Fig. 2.3. Its distance $d_{tar \to det}$ to the target position is 76 mm. In approximation the detector configuration at the MLL covers

$$\epsilon_{sc} \approx 4 \cdot \frac{S_{det}}{S_{sphere}} = 4 \cdot \frac{3 \cdot S_{crys}}{4\pi d^2} = 4 \cdot \frac{6021mm^2}{72583mm^2} = 33.2\% \tag{2.1}$$

of the space 4π.
The degree of spatial resolution is called granularity. A high granularity was obtained by dividing each detector six times. A crystal has one cathode, the so called core, which gets all signals. The six segments act as anodes.
In Fig. 2.4 the composition of one crystal is shown. Interactions of photons with matter are strongly dependent on the number of protons of the semiconductor material as the photo effect exhibits a Z^{4-5} dependency and the probability for Compton scattering is linear in Z. Furthermore, the band gap decreases with arising Z and enhances the resolution. Hence, n-doped germanium semiconductor serves as detector material particular well. For p-doping bor implants are used at the outer contacts. A depletion zone is formed by connecting the preamplifier which is installed on the lid with the core via AC-coupling whereas the segments are DC coupled. This zone can be massively extended by applying high voltage towards reverse direction and in the case of MINIBALL the zone almost reaches the size of the whole segment. Depending on each MINIBALL detector the high voltage is 3500V or 4000V, respectively. MINIBALL crystals reach an effciency of 60% relative to a 3" 3" NaI detector [22]. More informations about the operation of HPGe-detectors can be read in appendix B.
The six segments are spatially separated in such a way that no contact exists. The crystal is enclosed by a vacuum-sealed aluminium capsule of 0.7 mm thickness that does not touch the crystal. This is necessary to retain the thermal isolated inner part from the outer room temperature because the conductivity of this material evolves at very low temperatures. As a consequence the crystals must be cooled permanently with liquid nitrogen. This happens via a cryostat.

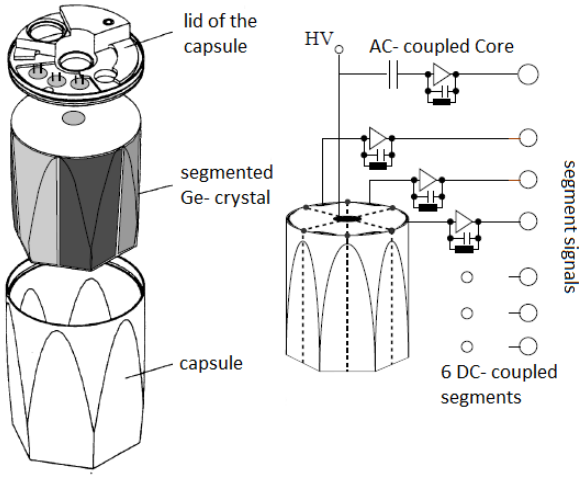

Figure 2.4: Composition of one MINIBALL- crystal. *From* [81]

The resolution of the detectors are indicated in the literature as 2.2 keV for the core and 2.4 keV for the segments at 1.3 MeV photon energy [81]. In our experiment the values for the cores extends from 2.6 keV to 3.7 keV. Most of them have a resolution of about 3.0 keV. The segments show a worse resolution of up to 8 keV. On the one hand due to

additional capacities between the crystals and the wall of the capsule a worse resolution for the segments is expected. On the other hand the shapers for the signals are not suited for high-resolution spectroscopy. So, the procedure in analysing signals is to take the energies from the core and the position is given by the segments.

2.3 Electronics Setup

The transformation of analog signals into (usable) digital signals establishes the electronics. The electronic setup was a central part of this thesis. Its aim was to collect and process as much as possible events with low dead time. In our case, this means sharp energy resolution over a time range determined by γ-cascades that decay almost simultaneously. In total four MINIBALL- detectors with each three crystals were used. Each crystal is segmented into six pieces and has a core that gets all information. Thus, the γ-detector array provide 84 signals.
Each detector is connected to one MADC-32 which converts the analog energy signals into digital ones. The converted data were read out by the Data Acquisition (DAQ) successively with a blocktransfer.

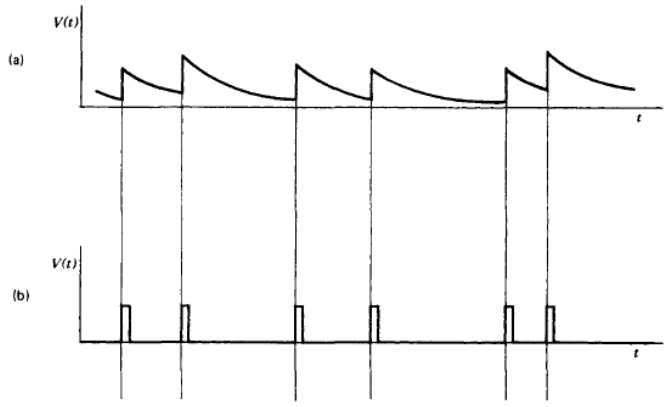

Figure 2.5: The spectra show the shape of the signals plotted against time. a) corresponds to the incoming signal with its large tail and pile up effects. In b) the shaper converts the signals into their origin amplitude with tighter width. *From* [44]

Fig. 2.8 shows the schematic setup of the electronics. A first preamplifier is integrated in the MINIBALL-detectors to minimize noise due to interferences of the very small detector signal with electro-magnetic fields or with the resistance of cables.
The signals of the segments are plugged in the modul STM-16+ that has the property of a shaping /timing filter amplifier with discriminator and multiplicity trigger [55]. The entrance signal has a fast increasing slope and a slow exponential decay. Because of the tail it is obvious that pile up effects occur when multiple signals come in rapid succession. Therefore, the shaping amplifier provides a new (Gaussian) shape of the signal without tail and magnifies the input signal. The strength of the amplitude is the distance from the (pile-up) bottom and the top of the signal. Fig. 2.5 shows the conversion of the incoming signal into the shaped outcome. However, the exponential decays in Fig. 2.5a are in reality not infinite but finite as illustrated in Fig. 2.6a. The initial signals are superimposed by electronics effects. Shaping of this signal gives a slight zero crossover or *undershoot* of the pulse, see Fig. 2.6b. Signals arriving during this undershoot are

assigned to wrong energies. Their amplitudes are reduced compared to the base line and a shift to lower energies is the result. Since in the digital spectra a part of the arising peak would contain too low energies one observes *left tail*. This effect has to be corrected by manual adjustments until the undershoot is eliminated and the Gaussian shape is restored. This procedure is called Pole Zero cancellation [44].
The transformed signal is directly sent to the MADC. This modul is an analog to digital converter of the signals. With the STM and the MADC the signals of the segments are fully processed.

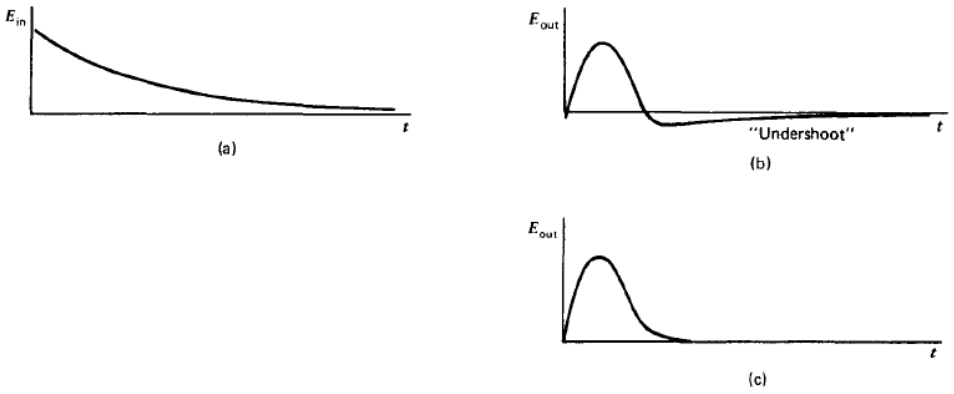

Figure 2.6: Tail of the signal shape in Fig. 2.5a). In a) the preamplifier passes a not pure but finite exponential decay, b) is the result by shaping the signal, c) corresponds to the signal after Pole Zero cancellation. *From* [44]

The command to trigger the signals of the detectors comes from the twelve cores. Their signals are splitted into slow and fast branches by the MSCF-16. This modul differs from the STM mainly through more individual operational functions like peculiar Pole Zero and threshold settings. With the slow branch one extracts the energy which is directly put into the MADC where the same procedure takes place as with the segments.

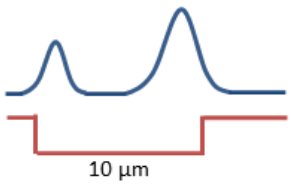

Figure 2.7: Energy signals of the segment and core with the corresponding gate.

The MADC offers more features. It assigns a time stamp to each signal with resolution of 16 MHz. To get a global clock for the signals of all MADCs the MADCs were synchronized in time. Too, it sets the length and delay of the gates and in addition a busy as long it converts the data. The fast branch carries the time information i.e. acts as trigger that opens a large enough gate in the MADC so that the energy signal of both the cores and the associated segments are enclosed, see Fig. 2.7. Energy signals of the segment appear earlier than the signals from the core. Hence, the gate is expanded to 10 μs which is quite long. Why the trigger cannot be put in the MADC so easily has the following reasons. A challenge presents the inaccurate working of the MADC when it gets a trigger in the time it is busy, so the trigger has to be held back. A further stopping of the acquisition of the signals is caused by an additional veto that is activated if the storage place of the MADC is filled again during the readout time of the DAQ. The trigger is stopped by using a veto composed of the busy of the MADC and the DAQ-busy.

The DAQ needs an input-signal that gives the command to read out the MADCs. To start the time-consuming readout as little as necessary, a complex help construction is needed. First one puts the trigger signals of all twelve cores into a rate divider and gives a reduction which ensures that no signals get lost, i.e. one has to prevent the MADC to get an overflow and to crash. Ideally, the DAQ starts when the MADCs have enough data to be worth for being read out. Of course, it must be ensured that the DAQ gets no readout command during an actual read out turn. That would cause a rejection and loss of the command with the result that the system is able to crash if the storage place of one MADC is completely full and gets the status of permanent busy. So if the DAQ gets a read out command during a readout, the command should occur after the actual reading out immediately and, additionally the acquisition of signals should stop meanwhile. Therefore, a coincidence is necessary with the components 'read out' and the DAQ 'busy'. This is done as follows: The coincidence signal is used as trigger for a gate-generator that opens an infinitely long gate. When the DAQ is again ready to read out another DAQ-signal 'Gobit' sends a pulse which activates the reset and thus, the gate will be closed. With its closing the delay signal occurs and is taken as command to start the DAQ immediatly. The gate corresponds to the above mentioned second veto for the trigger.

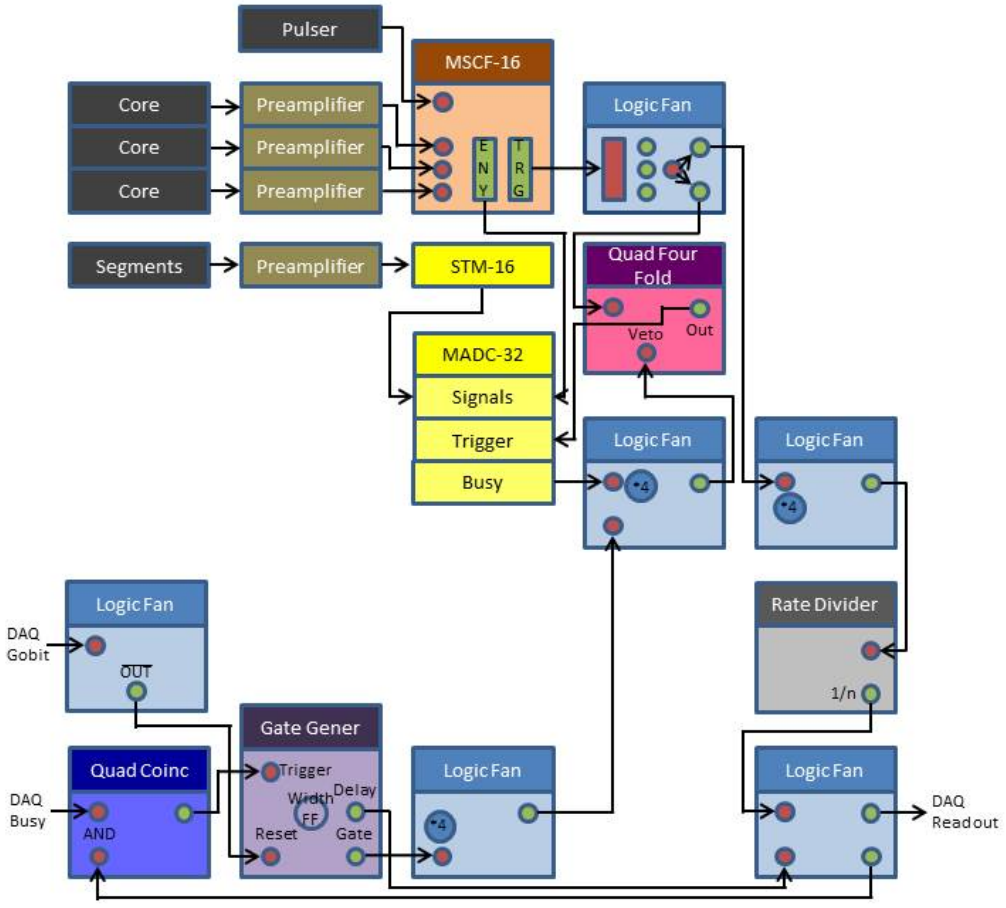

Figure 2.8: Electonics setup of this experiment for one detector. The labelling $\cdot 4$ means that the signals of all four γ- detectors have to be plugged in.

To get an idea of the dead time corresponding to the DAQ-mechanisms a pulser with low frequency which was chosen to be 100 Hz was initialised. Its sharp signals were added to the MSCF-16 and pass through the electronics. From the known duration of the experiment and from the number of accepted signals in the spectra it is easy to calculate the percentage of efficiency i.e. the ratio between accepted and rejected signals from each detector. In our experiments the loss did never exceed 20%.

Chapter 3

Calibration and Analysis Steps

The evaluation of the experiment was performed with a software package especially developed for this experiment which is based on the analysis platforms Marabou and ROOT. Due to the large set of HPGe detectors we have the possibility to analyse the data with the γ- K_x-ray- method resp. γ- K_x-ray- K_x-ray- method in contrast to previous experiments [42]. These methods allow clear separation of the generated fusion products and is suited to study absolute K_x-ray multiplicity synchronously for different reaction channels. That opens up the oppurtunity of studying structure effects.
This chapter explains the practical realization and tools for the analysis and addresses to necessary presets. Finally we use the analysis program in a first application, namely in testing the prediction of the absolute efficiency of coincident events with a ^{60}Co source.

3.1 Analysis Methods for the Determination of Multiplicity

For the analysis of the experiments, one has basically two methods to determine the K_x-ray- multiplicity. The γ- K_x-ray- coincidence method in subsection 3.1.1 is based on known transition energies which are used as gates in order to search for associated K_x-rays. The next subsection 3.1.2 deals with simultaneous occuring K_x-rays and should be seen as intermediate step towards the next method. Finally, an approach connects the two kinds of methods, i.e. the γ-ray gate separates the isotopes and then one searches explicit for cascades with at least one K_x-ray.

3.1.1 γ- K_x-Ray- Coincidence Method

If less than one internal conversion is expected per decay, one determines the multiplicity by comparing the number of measured K_x-rays with the number of produced evaporation residues. But in the original spectrum, this is hardly practicable since the K_x-rays and transition energies have large backgrounds and might be superimposed by transitions of other elements.
The setup enables us to assign each signal to a timestamp. The idea for the γ- K_x-ray-coincidence method is to exploit this information and to search for coincident signals between strong transition energies of evaporation residues and the K_x-rays. One choses transitions between the lowest excited states since cascades of higher excited states decay

into them instead of decaying immediately into the ground state; this let the lowest states be fed strongly.
As indicated before, we cannot be sure if the peaks consist only of the transitions of one element. Taking such peaks as indicators for the number of evaporation residues and searching for coincident K_x-rays, one would underestimate the multiplicty since a part of the peak cannot be coincident to the K_x-rays at all. However, the peaks can be used to generate a new spectrum which contains only events which are coincident to the peaks. The events of the established spectrum do not have to be coincident among each other. This spectrum is sufficient purified and the number of evaporation residues N_γ is determined by appropriate counting of the occuring γ-lines which belong unambiguously to the evaporation residue and, since both the transition lines and the K_x-rays radiate isotropic, the multiplicity M_K results from the quotient of the number N_{K_x} of detected K_x-rays and the amount of evaporation residues N_γ [42]:

$$M_{\gamma x} = \frac{N_{K_x}}{N_\gamma} \tag{3.1}$$

To keep the term simple, relative efficiencies are already included in the numbers N_{K_x} and N_γ.
The term γ- K_x-ray- coincidence method is perhaps misleading because we do not compare the gate with the K_x-rays but in the generated spectrum we compare the peaks of transition energies with the K_x-rays. The great advantages of this method are a purified spectrum and the elimination of the absolute efficiency, i.e. only relative efficiencies are necessary. A further important aspect is that cascades which do not emit K_x-rays are included in the statistics.
Of course, the described approach is suitable for already good studied nuclei where one knows not only the energies of the low lying states but also their transition intensities. The next two methods select the cascades according to the occurence of internal conversion and are required to compare our results with previous experiments.

3.1.2 K_x-Ray- K_x-Ray- Coincidence Method

The condition to know transtitions of states is hardly granted for heavy and super heavy nuclei. For them, the so called K_x-ray- K_x-ray- coincidence method is suitable. Instead of setting the gate on γ-lines, one is explicitely interested in simultaneous occuring K_x-rays. Of course, this method is not applicable if multiplicities are expected to be smaller than two. This is due to the fact that the original spectrum is too dirty to extract the absolute number of K_x-rays of the evaporation residues, so one relys on the number of coincident K_x-rays. For heavy nuclei, previous experiments predict indeed multiplicities larger than two (compare Fig. 1.7).
The number of coincidences has a defined distribution for a fixed multiplicity. For example, assume a multiplicity of $M_{XX} = 3$. Then, the probability to detect three coincident K_x-rays is limited by the total space volume ϵ_{sc}, the crystals cover. The detector array can detect none, one, two or three K_x-rays. The absolute efficiency of one detector is three times the absolute efficiency of one crystal, i.e. $\epsilon_{det} = 3 \cdot \epsilon_{crys}$ and hence, the probability to detect exactly one of the three emitted K_x-rays is:

$$P_{3-1} = 3 \cdot \epsilon_{sc}(1 - (\epsilon_{sc} - \epsilon_{det}))^2.$$

Two coincident signals are found with a probability of

$$P_{3-2} = 3 \cdot \epsilon_{sc}(\epsilon_{sc} - \epsilon_{det})(1 - (\epsilon_{sc} - 2\epsilon_{det})).$$

A simultaneous detection of all three K_x-rays leads to

$$P_{3-3} = \epsilon_{sc}(\epsilon_{sc} - \epsilon_{det})(\epsilon_{sc} - 2\epsilon_{det}).$$

The prefactors origin from the possible compositions of the three K_x-rays. In the first case, one detects one K_x-ray out of three. The second line consists of the compositions of detecting the first and second K_x-ray, the first and third K_x-ray and the second and third K_x-ray simultaneously. Finally, there is only one possibility to measure three coincident K_x-rays.
Internal conversion is assumed to occur prompt and so, in principle, several K_x-rays might have hit one crystal but the pile-up effect is responsible that such signals are discarded because the output signal would be the sum of the K_x-ray energies. According to Compton-scattering, coincidences within one detector are neglected.
In general, the scheme for the distribution of coincident events at fixed multiplicity M_{xx} is:
1 photon:

$$N \cdot \begin{pmatrix} M_{xx} \\ 1 \end{pmatrix} \cdot \epsilon_{sc}(1 - (\epsilon_{sc} - \epsilon_{det}))^{M_{xx}-1}$$

2 photons:

$$N \cdot \begin{pmatrix} M_{xx} \\ 2 \end{pmatrix} \cdot \epsilon_{sc}(\epsilon_{sc} - \epsilon_{det})(1 - (\epsilon_{sc} - 2\epsilon_{det}))^{M_{xx}-2}$$

3 photons:

$$N \cdot \begin{pmatrix} M_{xx} \\ 3 \end{pmatrix} \cdot \epsilon_{sc}(\epsilon_{sc} - \epsilon_{det})(\epsilon_{sc} - 2\epsilon_{det})(1 - (\epsilon_{sc} - 3\epsilon_{det}))^{M_{xx}-3}$$

The maximum number of measurable coincidences corresponds to the number of detectors, i.e. one cannot find more than four coincidences:

$$N \cdot \begin{pmatrix} M_{xx} \\ 4 \end{pmatrix} \epsilon_{sc}(\epsilon_{sc} - \epsilon_{det})...(\epsilon_{sc} - 3\epsilon_{det})$$

The scaling prefactor N is necessary to compare the terms with the measured number of $n-$coincidences, with $n = 1, 2, 3, 4$. In contrast to the above explained γ- K_x-ray coincidence method one relies on the explicit number of 2-, 3-, 4- coincidences. Two equations are sufficient to determine the multiplicity. The first one can be solved for the scaling prefactor N. Inserting it into the second equation gives the multiplicity M_{xx} of the element.

3.1.3 γ- K_x-Ray- K_x-Ray- Coincidence Method

The first two procedures differ in one important respect: The minimum number of coincident K_x-rays in the K_x-ray- K_x-ray- coincidence method is two. Due to the high background and superpositions, it is not possible to determine the total number of emitted K_x-rays. The γ- K_x-ray- coincidence method even takes cascades with none K_x-rays into account to determine the multiplicity. The adding and omitting of cascades might result to different multiplicities.
The measurement concepts in previous experiments, e.g. in [42], cannot be transferred to this setup and our K_x-ray- K_x-ray- coincidence method is rather not comparable with their analysis methods. They were able to identify cascades with the emission of only one K_x-ray but were blind on cascades which had no internal conversion.
We achieve a comparable method by combining the so far presented two methods. In the so called γ- K_x-ray- K_x-ray- coincidence method, the first gate is set on γ- lines of the evaporation residues. This makes the original spectrum sufficient purified and one can determine the number of K_x-rays; one gets explicit numbers for multiple-coincidences by applying the K_x-ray- K_x-ray- coincidence method. Thus, this multiplicity, labelled with $M_{\gamma xx}$, determines cascades which have at least one transition, initiated by internal conversion.
In previous experiments, the K_x-ray- K_x-ray- coincidence method was the approved way to determine the mean multiplicity of the formed isotopes. Without particle trigger, it has the disadvantage that one cannot distinguish between the xn- channels of the element. Especially, the dependence of internal conversion on the nuclear structure would be an interesting field. We separate the isotopes while in those experiments only the element was selected.

3.2 Event Buildung

The first step towards the just described methods to determine the multiplicity is to create coincidence matrices. All signals are tagged with a time stamp of 60 ns spacing. Simultaneous signals are identifiable by the difference of their times. Fig. 3.1a) and b) show this time difference where the time stamp of each signal is compared with the time stamps of all other signals. The large peak at $|\triangle t| \leq 3$ units (1 unit corresponds to $\approx$ 60 ns) are defined as simultaneous measured signals. The rest of the spectrum consists of random coincidences and an area around the peak results from dead time.
Next, a two dimensional matrix is formed with all coincident signals as presented in Fig. 3.4. The x- and y-axes show the energies of the coincident signals, the color represents the number of events between two γ-energies. The volume depends on the choice of the time interval in which one declares two signals as coincident. For prompt decays without isomeric states one expects a sharp time window but it must be adjusted to the individual decay of the residue. Rather long lived states need broader time intervals. Fig. 3.1b) shows a typical example of the broadness of the peak. In the peak all decays are merged i.e. decays from fusion and fission, isomeric and non- isomeric decays. The inner time window is sufficient for prompt decays but for non- isomeric decays it would be too narrow. More realistic for them is the broader window. The special treatment for evaporation residues with isomers are illustrated with the aid of a concrete instance in section 4.2.2. Using different time windows in the offline analysis, one is also able

to search for coincidences between signals which do not need to occur simultaneously. Corrections due to random coincidences in time are discussed in subsection 3.3.1.

The formed 2D- coincidence matrix includes all signals whose time stamps have a defined difference. The matrix is the starting point of the next step that involves setting gates on occuring peaks of photon energies which belong to the required isotope. To get pure samples, a well defined gate on the vertical and horizontal energy lines of known transitions or K_x-rays was used by taking one FWHM (Full Width at Half Maximum). This reduces only statistics but does not contribute to systematic uncertainties. It is energy dependent why the ^{152}Eu- source was used to make a FWHM- calibration. The resulting spectrum consists of K_x-rays and γ-energies which associate to the peak. The procedure to set gates on known γ- energies of expected evaporated residues is necessary due to the indistinguishability of the K_x-rays of isotopes. In each experiment there are more neutron-evaporation channels what leads to a variety of isotopes. Compton scattered photons or just background photons require further correction and its realization is presented in subsection 3.3.2.

The multiplicity can now be calculated by determining the number of K_x-rays and the peak areas of selected transitions whose choice relys on the demand that the produced evaporation residues must be recorded in total. This depends on the number and modes of the decay bands. Also, this spectrum is necessary for the γ- K_x-ray- K_x-ray method. In principle this method is applicable for evaporation residues with isomeric and non-isomeric states. A side effect of this method provides a very sensitive method to find isomeric states.

3.3 Background Corrections

In the previous section, matters of background correction were outsourced. The next two subsections present them. The first subsection explains an adequate correction of time windows which consist of real and random coincidences. The coincidence matrix taken so far requires further corrections due to individual backgrounds of each peak. Subsection 3.3.2 shows the treatment of this challenge.

3.3.1 Random Time Coincidences

Section 3.2 exhibited the necessity of using time windows to find coincidences between signals. We focus on an appropriate correction of the background because a part of the peak results also from random coincidences i.e. crystals measure indeed photons simultaneously but they do not descend from decays of the residues but from the background and Compton scattering, respectively. Random coincidences which remain in the peak are subtracted by removing the averaged number of coincidences which are counted in another time window. In Fig. 3.1a) this window was set left of the peak and is red marked. A proper method to get a reliable random coincidence subtraction is to select a broader range of the window and to scale the number of subtracted events to the width of the prompt window. In the analysis, the range of the random coincidence window was five times larger than the prompt coincidence window and was scaled accordingly.

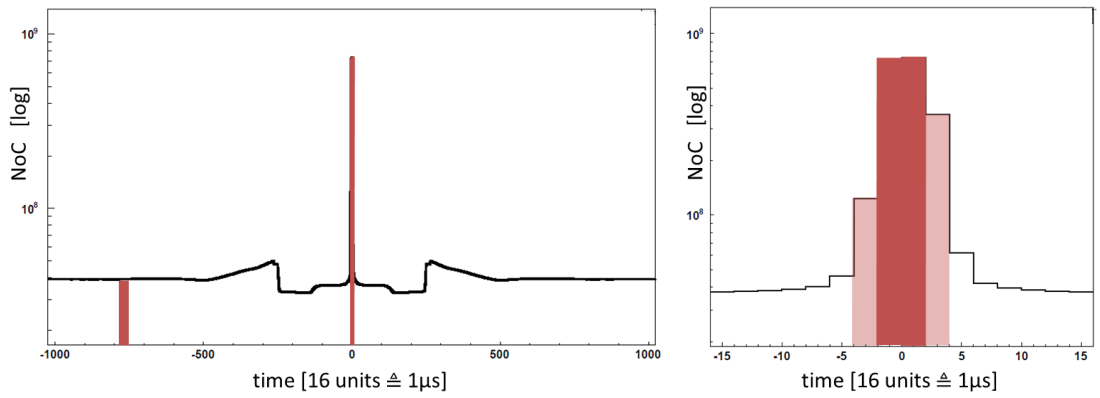

a) Red marked are the areas of the peak and of the background

b) Detail of the peak

Figure 3.1: Time difference spectrum with random coincidences from $|\triangle t| > 300$ units, dead time window from $4 < |\triangle t| < 300$ units and the real coincidences from $|\triangle t| \leq 3$ units.

3.3.2 Peak Background

The matrix is corrected from random time-coincidences but further background corrections are needed. Each peak continues to have an background which arises e.g. from Compton scattered photons of other peaks which vary the background locally. If one sets the gate on the peak one uses an additional gate which is set on an energy range that is near and right of the peak. Vicinity is necessary because the background must represent the surrounding area. The background is preferentially removed right from the peak because otherwise one would remove Compton-scattered photons of it.

3.4 Time Alignment

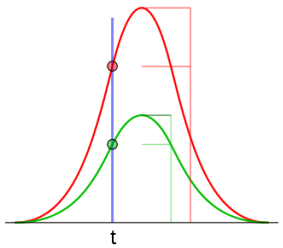

Figure 3.2: Defining the time stamp by the CFD. *From* [84]

The easiest way to minimize the background is to set a sharp time window. It is not only defined by prompt or isomeric decays but also from the processing to assign the time stamps to the signals. The allocation of the time stamp is provided by the trigger (in the MADC) and a CFD (Constant Fraction Discriminator) in the electronics. The principle of constant fraction triggering is shown in Fig. 3.2. It is a mathematical operation which mimics the maximum of the pulse by determining the zero of its slope. However, the rise time of the signal depends on the position where the interaction of photons with the germanium in the detectors occur and so, two coincident photons might have different time stamps. This is not unlikely since MINIBALL- detectors have large volumes.

We can check the relevance for our data, e.g. from the reaction ^{198}Pt(^{16}O,5n)^{209}Rn. The occuring γ- energies can be checked in its level scheme (Fig. 4.7). In the matrix of Fig. 3.3 the number of measured transition photons are plotted against the time difference $\triangle t = t(\gamma) - t(K_x\text{-ray})$ between them and the K_x-rays of radon.

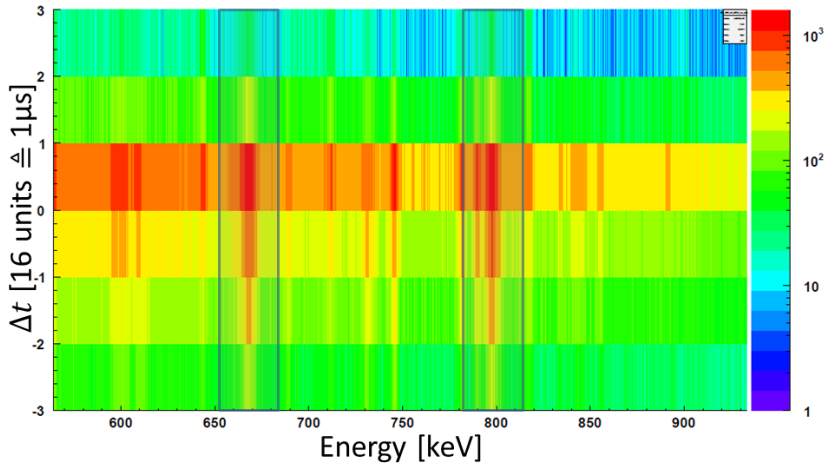

Figure 3.3: The plot shows the time difference of K_α-rays of radon and the associated transition of excited states at γ- energies from 500 keV to 1 MeV in the reaction ^{198}Pt(^{16}O,5n)^{209}Rn.

In the time interval from 0 to -1 unit i.e. from 0 ns to -60 ns one finds more entries of the low transition energies of ^{209}Rn (667 keV and 797 keV) than entries from random coincidences relative to $\triangle t = 0$. In this case, negative time difference means that the lowest transitions occur before internal conversion takes place which is impossible. If the place of interaction of the γ-rays with the germanium is energy dependent this might cause the strange behaviour. Hence the minimal time interval to declare two lines as coincident is from -60 ns to 60 ns.

3.5 Compton Scattering

Diagonals in coincidence matrices are indications for unwanted processes. For example an angle bisector would have shown that each event was compared with itself. In our data all coincidence matrices have $90°$ rotated angle bisectors i.e. a photon with an originating energy splits into two varying parts. Fig. 3.4 shows coincidences between two different detectors (a)) and within one detector (b)), respectively. Several solid diagonals are very distinctive on the right matrix and one finds an incomplete diagonal from the 511 keV peak with two symmetric maxima; in contrast to b) further lines seem to disappear in the background.
The crystals of each detector are not shielded from Compton-scattered photons. γ-rays which are inelastic scattered by particles lose a part of their energies. Depending on the lose of energy, the photons change the direction and can be detected by a further crystal where the residual energy is stored. Within one detector, the Compton-scattered photons leave the first crystal and hits another crystal under arbitrarily angles. Hence one has solid lines in Fig. 3.4b). This is an expected effect and coincidences within one detector will not be included in the analysis.
Compton scattering also explains the incomplete diagonals in the coincidence matrix between two independent MINIBALL detectors. In this case only selected scattering angles are allowed since the detectors have a limited covering of the 4π- space.
In the experiments, Compton scattering could not be avoided. Exemplarily, two different gates were set on the coincidence matrix in Fig. 3.4. The spectra in Fig. 3.5a) and b) show the γ- energies which are coincident to the gated energy range. The spectra exhibit

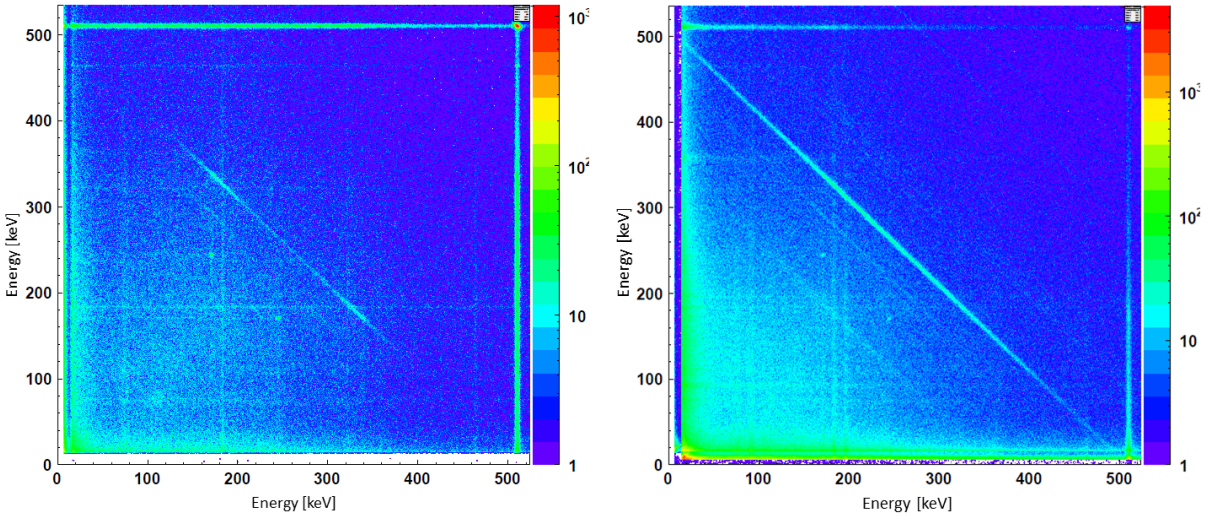

a) Coincidence matrix between two detectors

b) Coincidence matrix within one detector

Figure 3.4: Diagonal lines in the coincidence matrix

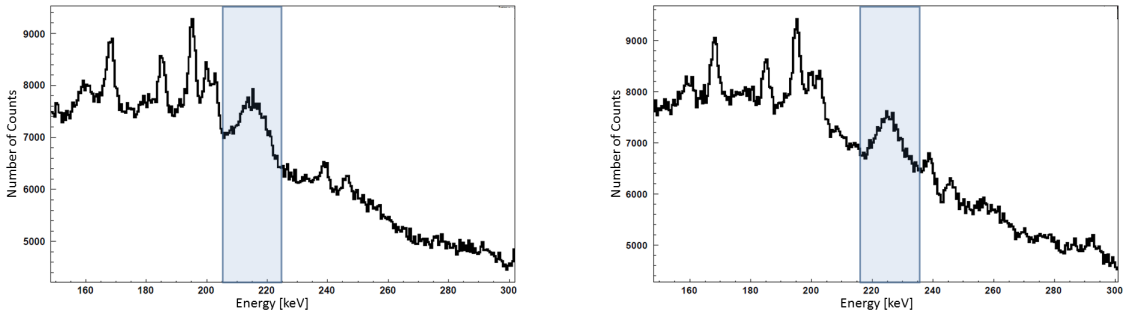

a) Gate is set from 290 keV to 300 keV

b) Gate is set from 280 keV to 290 keV

Figure 3.5: γ- energies which are coincident to gated peaks. The blue marked peaks are artefacts from the diagonal at 511 keV.

the occurence of peaks which are attributed to the diagonal at 511 keV in the coincidence matrix i.e. to Compton scattered photons (blue marked). These peaks are false friends. To identify these ones, various background cuts will be set in the analysis. This guarantees that only real peaks were taken into account.

3.6 Photon Detection Efficiency

3.6.1 Efficiency

For the analysis exact energy and efficiency calibrations of each core are essential. In the experiments energies range from 35 keV to 1.5 MeV. The lower limit is defined by the lowest generated K- x ray from the created evaporation residue, in our case that from radon. The upper limit is not specified but follows from the necessary resolution in the lower energy range.

Both energy calibration and efficiency are determined with the sources ^{152}Eu and ^{133}Ba which cover an energy range from 30.6 keV to 1.4 MeV. The normal approach to calibrate the energy is making a linear ansatz. Fig 3.6 shows the residual of the measuring points with the reference line for a perfect linearity at the zero- line. The unit of the x- axis is the number of available channels in the MADCs. Up to channel number 1000 the residual for the data points falls but therafter it arises. For a linear calibration that would imply a shift in the energy to channel correspondence. Since the highest measurable photon energy is 1.5 MeV and the europium source has its last strong peak at 1.4 MeV the use of a polynomial of 8th degree guarantees a sufficient energy calibration. It is clear that for the energy regions that are outside of the outer peaks of the sources this kind of calibration is improper. An alternative would be the usage of two linear fits. One fit covers the region up to channel number 2000 and the other one succeeds from this value.

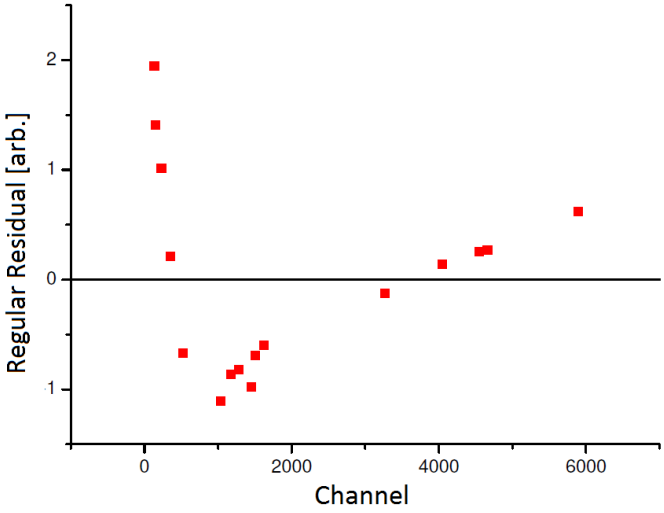

Figure 3.6: The residual clearly demonstrates that a linear fit for the whole range is not possible.

Additional to energy calibration, the source- measurements are used to determine the efficiency. The following formula was used as a fit- function

$$\epsilon(E) = (a \cdot E + b/E) \cdot exp(c \cdot E + d/E). \tag{3.6}$$

The efficiency is determined in two steps: First the formula is applied for the barium source because its peaks reach the low energy region where the detector efficiency decreases again. Furthermore, the energy point 344 keV of ^{152}Eu lies between two energies of ^{133}Ba and can be taken as reference value very well. With help of the calibration of barium one obtains a reliable value for the relative efficiency of this peak. The remaining europium- energies get multiplied with the relative efficiency of the 344 keV- peak. The two connected sources serve as data points for a second application of the efficiency formula. Fig. 3.7a) gives the total efficiency of all cores, located at the centre, b) corresponds to the efficiency where the sources were placed on the implantation plate. Why a second calibration is necessary we explain in the next section. The parameters for both cases are summarized in Tab. 3.1.
Each core has its own efficiency and contributes to the total efficiency depending on its detection efficiency. The gathered data will be summed up. The total efficiency consists of the averaged product of the core's efficiency and the absolute number of the volume of their characteristic γ- lines:

	Value centre	Uncert.	Value plate	Uncert.
a	$1.04 \cdot 10^{-3}$	$2.7 \cdot 10^{-4}$	$7.17 \cdot 10^{-4}$	$8.11 \cdot 10^{-4}$
b	506	10	579	59
c	$1.18 \cdot 10^{-3}$	$1.7 \cdot 10^{-4}$	$-0.93 \cdot 10^{-4}$	$6.41 \cdot 10^{-4}$
d	-111.9	1.1	-138.9	5.1

Table 3.1: The parameters for the efficiency determined at the centre and on the plate

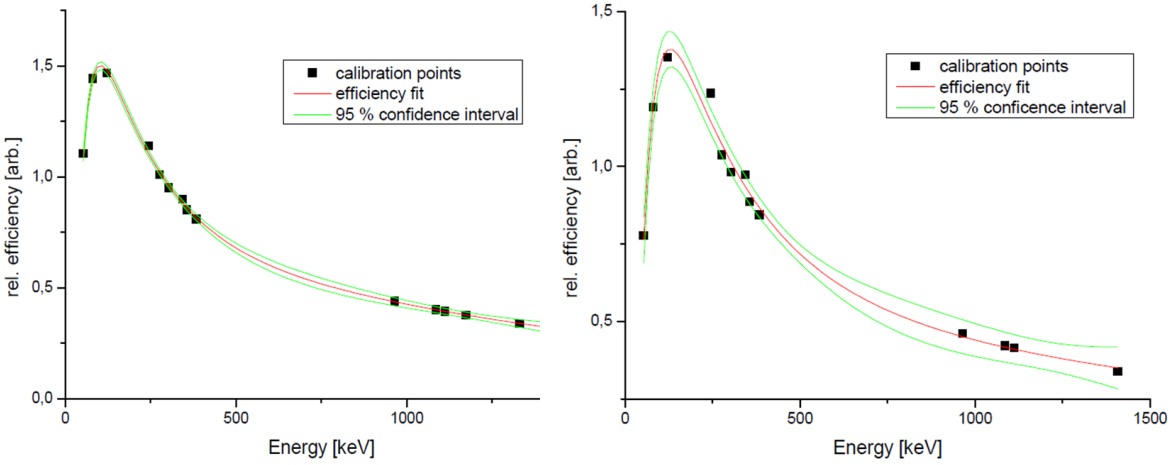

a) Efficiency at centre

b) Efficiency on the implantation plate

Figure 3.7: Relative efficiency normalized to one at the 276 keV line. The efficiency is made in combination of two sources. The uncertainty is given by the confidence interval of 95%.

$$\epsilon_{tot}(E) = \frac{1}{\sum_{i=1}^{12} V_i(E)} \sum_{i=1}^{12} V_i(E) \cdot \epsilon_i(E) \tag{3.7}$$

3.6.2 Position of Radiation

The crystals vary in their acceptance capacity which was taken into account in Equ. 3.7. However, the measurable intensity does not only depend on the quality of the core but also on geometrical effects and hence the γ-ray decay positions of the nuclei are fundamental to calculate the right ratio of the peaks. Although each event is assigned to its time of measurement with the help of a time stamp that has a resolution of 60 ns, this resolution of time is indeed adequate to find coincident decays but insufficient to allocate the position of decay. This lack of information would have been of importance as the intensity of radiation decreases with quadratic distance. For the efficiency this is a source of uncertainty, especially since the half- lives of all states and the occurence of internal conversion is often not known. To have an idea of this geometrical effect a calibratioan source was mounted on the implantation plate. This corresponds to the maximal position change of the evaporation residues. In Fig. 3.8 a direct comparison is demonstrated by superimposing the two efficiencies. While they differ in the energy region < 300 keV one recognizes convergence for higher energies.
Let's clarify for the analysis of the data which is the approach for the choice of calibration. Internal conversion is supposed to occur after short time the evaporation residue was

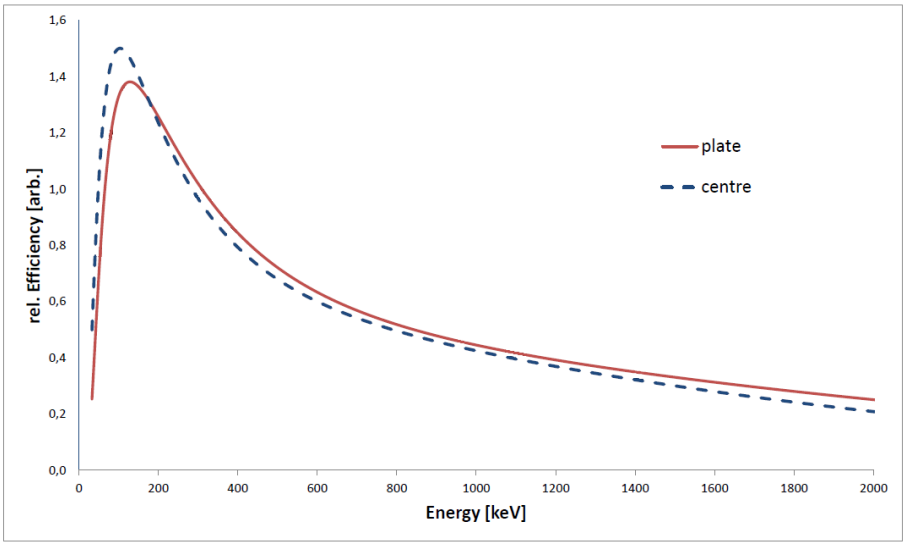

Figure 3.8: Comparison of the efficiencies, measured at the target position (centre) and on the plate.

formed. In all cases, the K_x-rays are evaluated with the efficiency determined at the target position. This regards to all kinds of methods for finding coincidences i.e. the γ-ray- K_x-ray, K_x-ray- K_x-ray and γ-ray- K_x-ray- K_x-ray method. Photons from transitions are distinguished between prompt and non- prompt decays. Prompt decays include photons which are coincident to K_x-rays within three units of the time stamp, i.e. 180 ns and their efficiency calibration is the same like for the K_x-rays.
The situation changes if decays of isomeric states are detected at a time where the K_x-rays occured at least two units of the time stamp before. These (non- prompt) photons are surely implanted on the plate and will be calibrated with the efficiency of Fig. 3.7b).

3.6.3 Probability for Detection of Coincidences

Effects like time alignment and Compton scattering were discussed qualitatively so far. The aim of this section is to check their influences on the results. On the basis of the setup's geometry, section 3.1.2 determined the probabilities to measure coincident signals at fixed multiplicity. These calculations did not include external effects like dead- time that might hinder to measure coincidences. Experimentally most suitable to check these effects is the usage of a ^{60}Co source. Its characteristic is the simultaneous decay of two photons with the energies 1173 keV and 1332 keV. Fig. 3.9a) is the recorded spectrum. The two peaks have almost the same height but most of the peak areas consist of signals which are not measured simultaneously with another one. To a certain percentage only one instead of two signals are detected.
One searches for coincidences to the line at 1332 keV. The resulting spectrum in Fig. 3.9b) has a large peak at 1173 keV. The ratio between the number of coincident events at 1173 keV, $N^{after}(1173\text{ keV})$ and the original volume of the peak at 1332 keV, $N^{before}(1332$ keV) is given by

$$P_{meas} = \frac{\frac{N^{after}(1173\text{ keV})}{\epsilon_{1173}} - \frac{N^{after}(1332\text{ keV})}{\epsilon_{1332}}}{2 \cdot \frac{N^{before}(1332\text{ keV})}{\epsilon_{1332}}}$$

$$= \frac{\frac{1025089}{0.376} - \frac{8857}{0.337}}{2 \cdot \frac{5768873}{0.337}} = 7.9(1)\%. \tag{3.8}$$

where ϵ is the efficiency at the centre. At the energy 1332 keV a small peak remains. At strong sources it is not unlikely that many decays occur such that more than one decay is registered at the same time. i.e. the photons have the same time stamp. Also the peak at 1173 keV consists partly of random coincidences. The second term in the numerator takes this into account by subtracting the volume of the peak at 1332 keV, $N^{after}(1332)$. The whole term has to be divided by two because of effects originating from the program code.
For the theoretical calculation one obtains

$$P_{2-2} = \epsilon_{sc}(\epsilon_{sc} - \epsilon_{det}) = 33.2\% \cdot 24.9\% = 8.3\%. \tag{3.9}$$

The correspondence is very good i.e. electronic effects are small with 5% deviation but not negligible. In the analysis we resort to this where necessary.

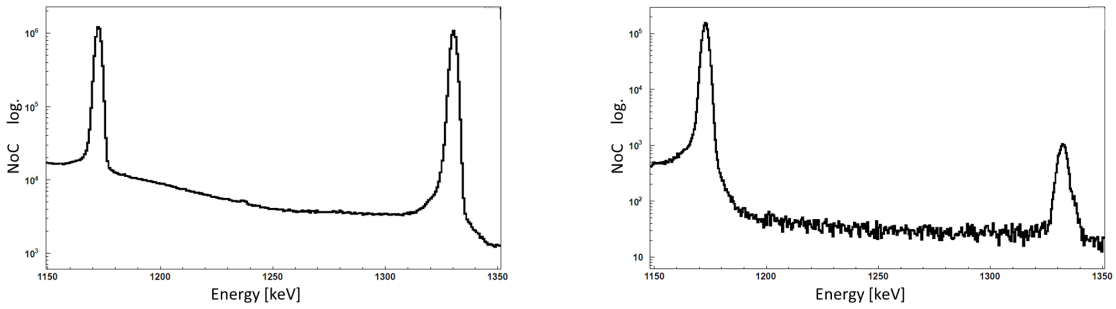

a) Spectrum of ^{60}Co

b) Coincident lines to the peak at 1332 keV

Figure 3.9: Detectibility of coincidences on the example of an ^{60}Co source. The spectra are zoomed from 1150 keV to 1350 keV.

Chapter 4

Reactions with Medium Heavy Targets

The setup is located in the Maier Leibnitz Laboratory in Garching. The acceleration of the beam is accomplished by the van de Graaf Tandem accelerator with high voltage up to 14 MV. The experiments were done from May to July 2013.
The collected data cover various fields of interests. One motivation was to test effects of nuclear structures on the proposed mass- dependence on K_x-multiplicity. The sections deal with experiments where the same element radon but different isotopes were produce. Their analysis is examined with the presented coincidence methods. The surprising results are the basis for a discussion about the validity of the methods.
All uncertainties of the results are based on the standard practice and are oriented towards [32]. The uncertainties in the coincidence methods arise from the statistical uncertainty of the peaks but most of the uncertainty comes from the subtraction of the background. The values are listed in appendix C.

Multiplicity for the Isotope Radon

For medium heavy nuclei, one expects a reduction of nuclear structure effects for the occurrence of internal conversion i.e. for the multiplicity since the nucleus mass gain in importance. This section investigates the element $_{86}$Rn. The formation of several isotopes of one element is reached by using very different platinum isotopes as targets. The reactions ^{192}Pt(^{16}O, 4n)^{204}Rn, ^{198}Pt(^{16}O, 5n)^{209}Rn and ^{198}Pt(^{16}O,4n)^{210}Rn were used to populate states in ^{204}Rn, ^{209}Rn and ^{210}Rn. The beam energy for both experiments was 87 MeV. This energy was assumed to give the highest fusion cross sections where the fission is not too strong, yet. The cross sections of the evaporation residues, their maximum spin as well as their angular distribution in relation to the beam direction are based on the theoretical calculations of the program PACE4 from LISE [53]. Fig. 4.1 shows data on whose basis the beam energy for reaction the ^{198}Pt(^{16}O,xn)^{y}Rn was chosen.

4.1 ^{192}Pt(^{16}O,4n)^{204}Rn

After the reaction ^{192}Pt(^{16}O, 4n)^{204}Rn at a beam energy of 87 MeV, the compound nucleus has a velocity of 0.249 cm/ns and a maximum spin of 25 $\hbar$ [53]. The strongest fusion channel in the reaction is the evaporation residue ^{204}Rn. This nucleus is kind of

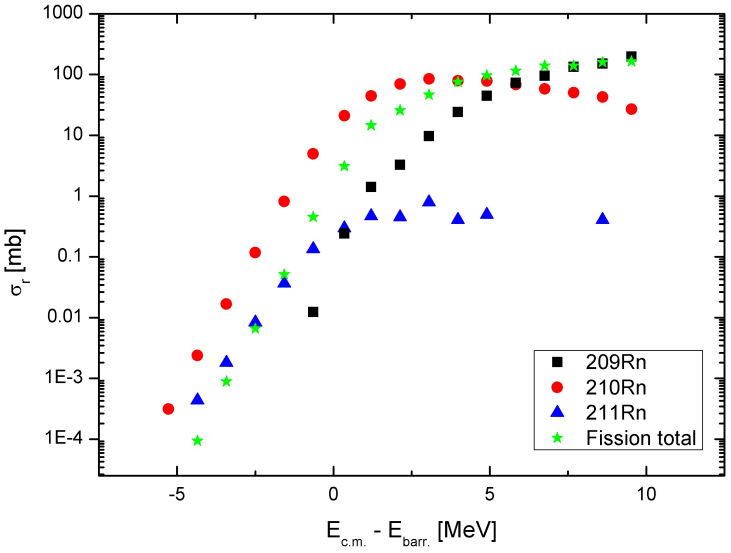

Figure 4.1: Example for the choice of the beam energy, marked in red, for the reaction ^{198}Pt(^{16}O,xn)^{y}Rn. High evaporation residue cross section was in this case more important than low fission formation. *Data from* [53].

deformed. In contrast to the number of protons the number of neutrons is not close to a magic number.

The raw spectrum is shown in Fig. 4.2a. The strongest lines, marked with "1" and "2", are atomic excitations of the target, i.e. K_α and K_β of platinum. All other large peaks stem from fission decays. The γ-lines of ^{204}Rn exist but are small in comparison of the strongest lines. The right figure b) is the zoom into the K_x-ray energy range. Despite of the large characteristic radiation of platinum, one recognizes the K_αs of radon in the tail of the platinum peaks and the K_β as small peak. The spectrum is purified if one uses the γ- K_x-ray- coincidence method. Following the level scheme of ^{204}Rn in Fig. 4.3, a gate on the $2^+ \rightarrow 0^+$ transition at 542.9 keV should return all higher-lying γ-rays, populated in the reaction. This is a general feature for even-even nuclei, as most cascades finally decay in the yrast-cascade. Fig. 4.2c shows the result: The marked lines are associated with the isotope ^{204}Rn and are clearly separated from background. Comparing the level scheme in Fig. 4.3 with the detected transition lines, two bands are excited and their transition energies are green resp. dark blue colored in the Fig. 4.2c and also in the level scheme. All known cascades merge together in the state 4_1^+ except the transition from $(2,3,4)^+$ into 2_1^+. The last-mentioned transition has an energy of 1084.9 keV and is not present in the spectrum. Thus, the $(2,3,4)^+$ at 1084 keV was not populated significantly in the reaction.

For the determination of the multiplicity it is sufficient to count the area under the peak at 588.6 keV, $N^{542}(588\text{ keV})$, and to compare it with the number of K_α's and K_β events of ^{204}Rn, $N^{542}(K_x\text{-rays})$. The efficiency corrected experimental values are presented in Tab. 4.1. The multiplicity is the ratio of the two areas $N^{542}(\text{K-x-rays})/N^{542}(588\text{ keV})$ and one obtains the value $M_{\gamma x}$=0.91 (2).

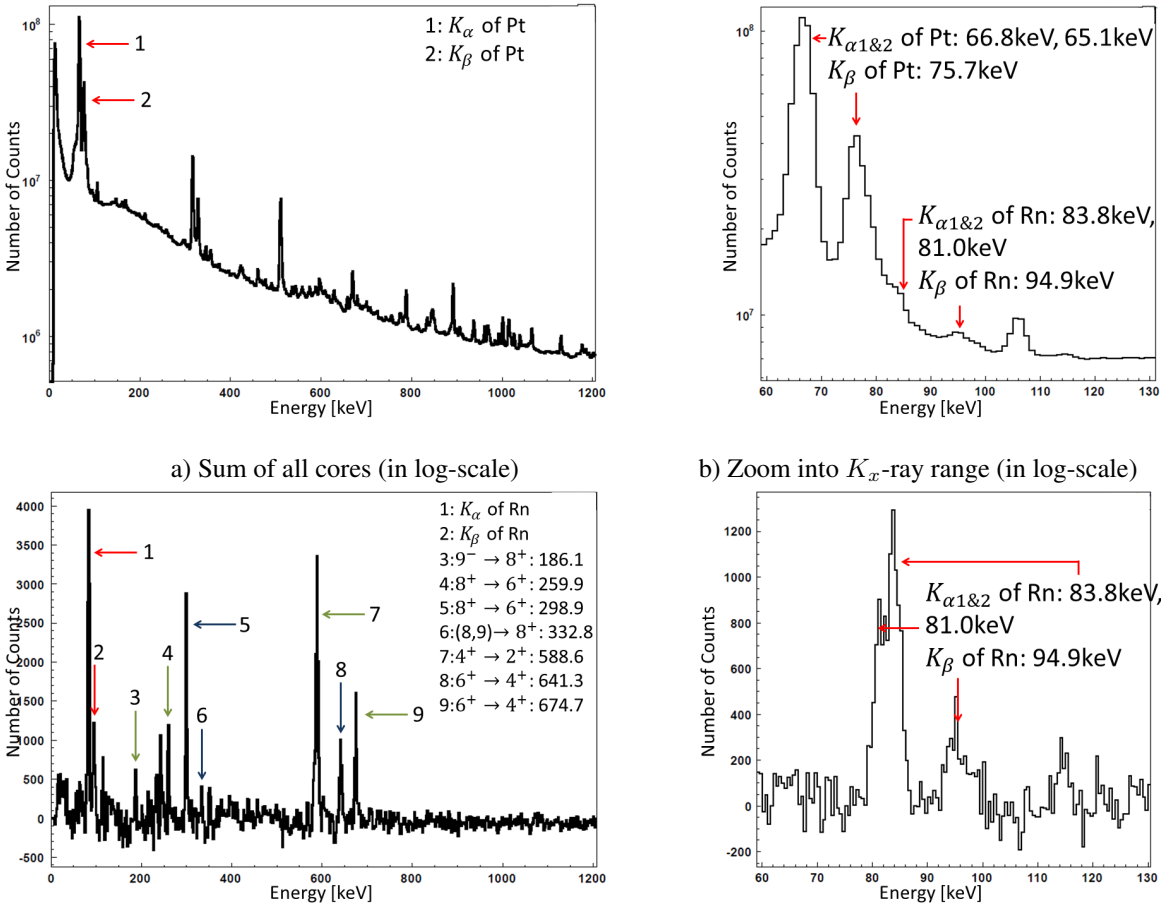

a) Sum of all cores (in log-scale)

b) Zoom into K_x-ray range (in log-scale)

c) Gate on 542 keV

d) Zoom into K_x-ray range

Figure 4.2: The colors of the arrows mark the different cascades. The different binning of the x-axis cause different number of counts between the full spectrum and the K_x-ray range.

Trans.	Energy [keV]	Area	eff.corr. Area
$K_{\alpha1}$	81	6616 (123)	7120 (132)
$K_{\alpha2}$	83	8687 (133)	9282 (142)
K_β	95	4557 (117)	4747 (122)
$1131 \rightarrow 542$	588	9070 (156)	23213 (399)
$1627 \rightarrow 542$	1084	0	0
$M_{\gamma x} =$			0.91 (22)

Table 4.1: The gate was set to the lowest transition energy 542 keV.

The value is much lower than one could have expected from previous experiments. The multiplicity of many experiments are summarized in Fig. 4.12 and lie above our result of ^{204}Rn. However, the results are determined using a different analysis method which is similar to our γ- K_x-ray-K_x-ray coincidence method, i.e. they could only identify cascades where at least one K_x-ray was emitted.
Applying this method we set the γ-gate on 542 keV. The second gate is the K_x-ray energy region and this gate is necessary to search for coincident K_x-rays, i.e. the multiplicity of each event. The values are listed in the second column of Tab. 4.2.The term *one coincidence* is related to the number of K_x-rays which are coincident to the energy 542 keV and

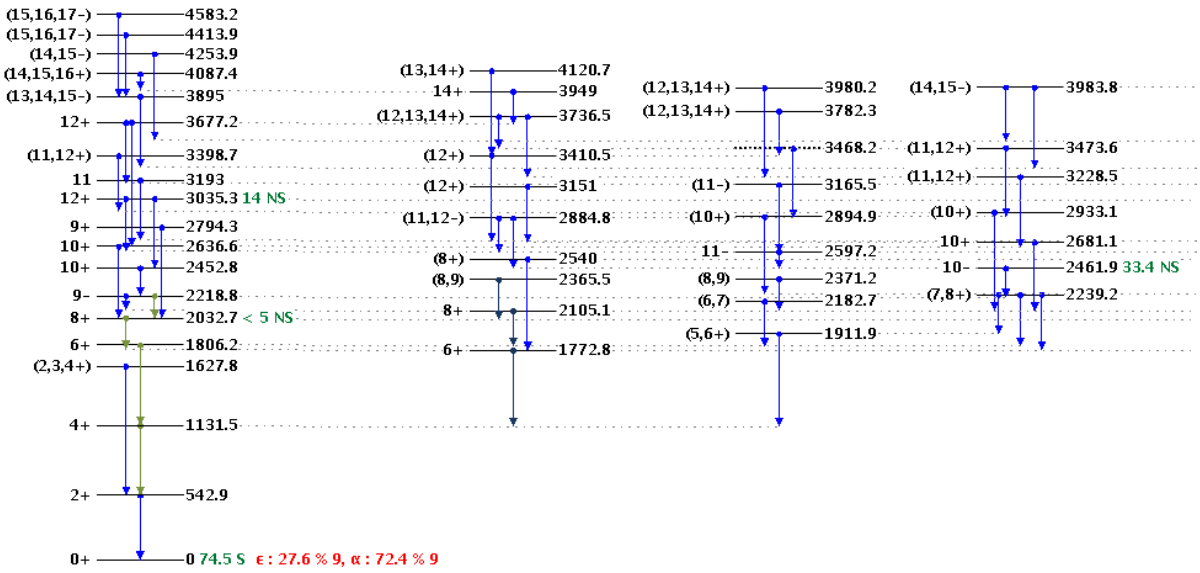

Figure 4.3: Bands of ^{204}Rn (*incomplete*). Peaks exist for the first two bands. The remaining ones are not or only weak excited. *Data from* [64]

not coincident to another K_x-ray. *Two coincidences* mean that exactly two K_x-rays are coincident to the gated photon and coincident amongst themselves. *Three coincidences* follows the scheme but the statistics is far too small.
Since we have background, a reference region was set right of the K_x-ray energy region. The multiplicity of the region is presented in the third column. Events which are only coincident to the gate, i.e. coincident to photons with the energy 542 keV, are labelled with one. The number of two coincidences relies to the number of reference photons which occured simultaneously with another photon within the region. These values have to be normalized to the range of the K_x-ray region and finally, they are subtracted from the second column.

# Mult.	K_x-rays	Ref.	K_x-rays *corr.*
One	38698 (197)	17079 (131)	18203 (135)
Two	299 (17)	27 (5)	272 (16)
Three	2	0	2

Table 4.2: The lines give the number of coincidences between transitions and K_x-rays when the first gate is set on 542 keV.

The last column is the number of multiple events in the K_x-rays region which are assumed to stem from the decay of evaporation residues. Applying the formulas from section 3.1.2, we obtain the for multiplicity of ^{204}Rn

$$M_{\gamma xx} = 1.91(48). \tag{4.1}$$

This is much higher than before. The two used analysis methods differ in one important subject: In the γ- K_x-ray- method we include cascades with no internal conversion. So, two reasons are likely for the increased multiplicity using the γ- K_x-ray- K_x-ray- method. Internal conversion might be strongly dependent on the cascades, on which the evapora-

tion residue is deexciting. Cascades without internal conversion are neglected in the γ-K_x-ray-K_x-ray coincidence method.

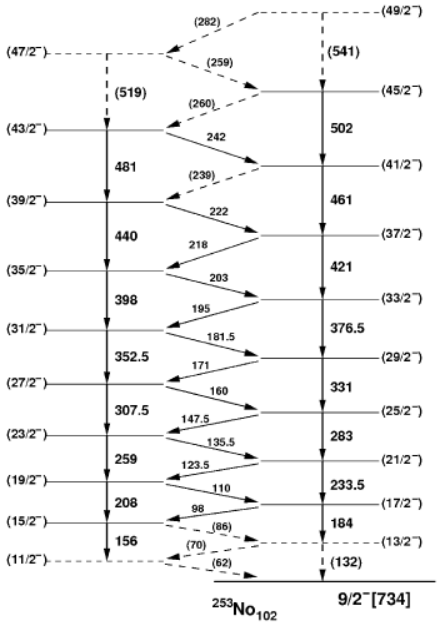

Figure 4.4: Herzberg et al. measured $M1$- Transitions between Rotational bands for ^{253}No. *From* [37]

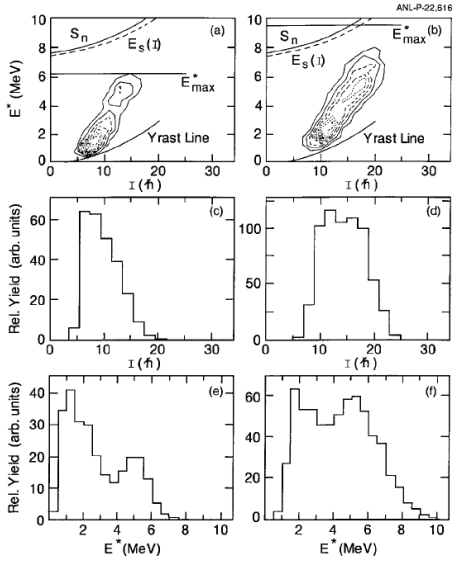

Figure 4.5: Example of different spin I and excitation energy E^* of the evaporation residue ^{254}No at $E_{beam} = 215$ MeV (*left*) and at $E_{beam} = 219$ MeV (*right*). *From* [70]

Karwowski worked out in the mass region $A = 200$ that $M1$- transitions come from transitions between strongly coupled rotational bands ([42], p.16) which are highly converted and have low energy. Due to the low energy spaces between the $M1$- decays of adjoining rotational bands and the high K_x-ray conversion coefficient for low energetic $M1$-transitions one also expects internal conversion between transitions at high spins. Herzberg et al. [37] was able to identify such low- energetic $M1$ transitions. These $M1$- transitions appear as interband transition between the two negative-parity bands, shown in Fig. 4.4. This is in agreement to the work of Karwowski et al. Due to such effects, it seems possible that only selected cascades have large K_x-ray multiplicities, whereas other bands may not shown any substantial internal conversion at all.

Another hypothesis is that the evaporation residues have broad distributions of the maximum spin. If the decay begins at lower states and under the assumption that internal conversion occurs in high energy regions then it would not appear, too. The γ-K_x-ray method collects all produced evaporation residues whereas the γ- K_x-ray- K_x-ray method would be only sensitive of the highly excited states with large spin.

Reiter et al. [70] measured the distribution of spin I and excitation energy E^* of the evaporation residue ^{254}No. Reiter could show that the distribution relys not only on the beam energy but also at fixed beam energy, there is a wide spread of the entry channels. The example is shown in Fig. 4.5. For the beam energy $E_{beam} = 215$ MeV the average highest excited spin is at around 10 $\hbar$. This average value shifts towards 15 $\hbar$ when using the beam energy $E_{beam} = 215$ MeV. If the internal conversion occurs only at transitions of high states, the multiplicity should change since more evaporation residues exhibit large initial spins.

The difference between the two explanations is that the first one is based on structure effects of the residues, i.e. the internal conversion takes only place in certain cascades. The second reason explains from which state and spin on internal conversion occurs. Both explanations might result in a weighted multiplicity of 0.91 when

the γ- K_x-ray method was used and an enhancement of it as soon as one demands for mandatory coincidences between γ-transitions and at least one K_x-ray.
A trivial explanation might be isomeric states. For them the time window would be to narrow. The nuclear data from *NNDC*[64] (see Fig. 4.3) have almost no information on the half lifes of the individual states. It is known that one state (2461.9 keV and spin (10-)) lives 33 ns long and another has a half life of 14 ns (3035 keV with spin (12+)). But they are short living in relation to the coincidence time interval of $|\triangle t|<$ 60 ns and are included.
One can check if further isomers exist and if they emit K_x-rays. Like in the introduction of this chapter one searches for all γ-rays which are coincident to K_x-rays of radon and plot these ones against the time difference $\triangle t$. If rather long lived states exist which exhibit internal conversion then one should see an exponential decay of strong transitions between low lying states because in even- even nuclei basically all cascades end in the yrast cascade. Fig. 4.6 shows an example of such an analysis. At present, we assume that there are no isomers since expected tails of transition energies of low lying excited states (542 keV and 588 keV) are not visible at any time difference. Hence, the time window $\triangle t$ from -60 ns to 60 ns was sufficient for our analysis.

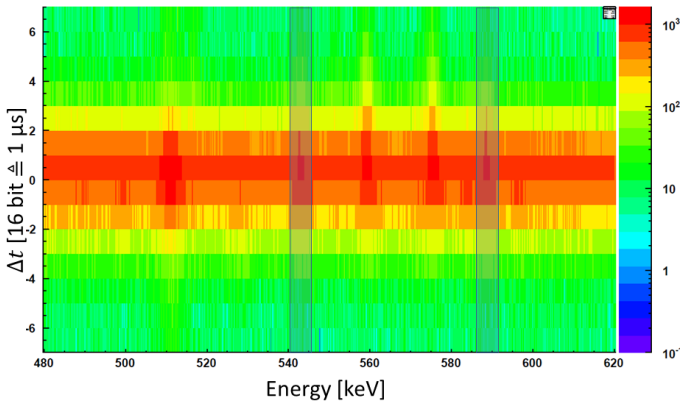

Figure 4.6: The gate is set on K_α- x-rays of radon. Strong decay lines of ^{204}Rn are indicated by the blue windows.

4.2 ^{198}Pt(^{16}O,xn)^{y}Rn

The shape of the radon- isotope converts from a deformed structure into a spherical one with rising number of neutrons towards the magic number $N = 126$. The neutron rich ^{209}Rn and ^{210}Rn were produced by fusion of the beam ^{16}O with the target ^{198}Pt. The compound nucleus receives a maximum spin of 23$\hbar$. Its initial speed is calculated to 0.242 cm/ns [53].

4.2.1 ^{209}Rn

The cross section for this reaction is larger than in the previous section. In Fig. 4.8a the spectrum is shown and markant lines of ^{209}Rn are clearly identified. Although the peak 667.7 keV is a double peak, a large part belongs to this isotope. On the right is the zoom into the K_x-ray region and also here, one recognizes the K_x-rays of radon better than in

the last reaction. The level scheme (see Fig. 4.7) is more complex compared to ^{204}Rn. Two lines end in the lowest excited state $9/2^-$. These are the transitions $13/2^- \rightarrow 9/2^-$ and $13/2^+ \rightarrow 9/2^-$. The decay of the state $9/2^-_1$ into the ground state is the last one of all cascades. The state $13/2^+$ is an isomer, thus, we give priority to this subject, now.
The excited state has a half life of 13.4 μs. Hence, setting the gate on the last transition $9/2^- \rightarrow 5/2^-$ would indeed give the number of produced evaporation residues but all K_x-rays which belong to the cascade which ends preliminarily in the isomer, would be neglected.

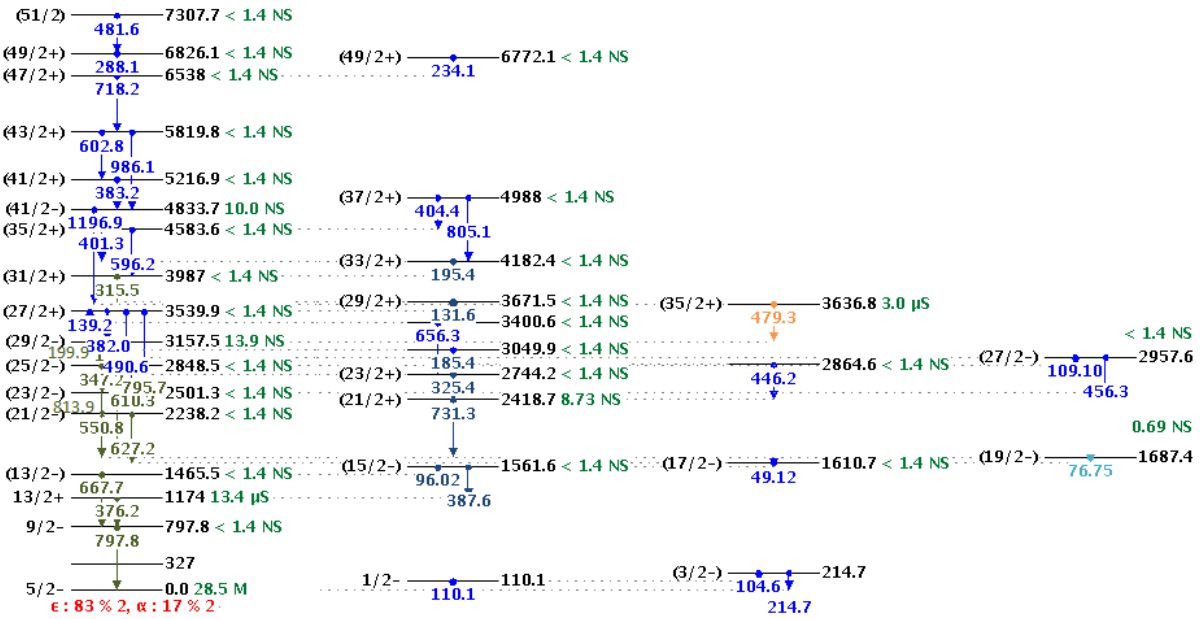

Figure 4.7: Level scheme of ^{209}Rn. Observed decays are colored. *Data from* [64]

We used two gates: The first one corresponds to the decay path where no isomer occurs. The decay into the lowest excited state is carried out by the transition $13/2^- \rightarrow 9/2^-$ with the transition energy 667.7 keV. The number of produced evaporation residues is given by the peak area at 797.8 keV. The second gate represents the decay into the isomer. It is populated by the transition $15/2^- \rightarrow 13/2^+$ with the energy 387.6 keV.
First, we analyze the data with the γ- K_x-ray- coincidence method. The spectra which result from setting the gate on the named transitions are presented in Fig. 4.8c)-f). Peaks which are associated to the level scheme of ^{209}Rn are labelled and the color of the arrows relys on the cascade on which the nuclei decay. We emphasize that both transitions are fed from the same cascades with the exception that the spectrum e) has the additional transitions $15/2^- \rightarrow 13/2^-$ at 96.0 keV and the transition into the ground state.
Note, that the line at 105 keV in d) and f) does not belong to the isotope but is coincident to the peak at 667 keV. This line also does not belong to another isotope of radon, thus, the K_x-rays are unaffected to this decay. The relative increase of the K_β-intensity in f) is due to the transition $15/2^- \rightarrow 13/2^-$ which has the similar energy 96.0 keV. For the multiplicity, all three peaks of the characteristic radiation are needed. Since the ratio between the intensities of the K_α lines and of the K_β peak is known [18] and since the K_α- peaks should be pure these ones can be used to calculate the peak area of the K_β.
The energy level scheme exhibits one further challenge. The transition to the ground state has the energy 797.8 keV. A similar γ- energy of 795.7 keV exists in the transition from

the level with 3400.6 keV (spin (27/2+)) into the state with 2744.2 keV (spin (23/2+)) and cannot be distinguished in the spectrum originating from the 667 keV-gate, seriously. In Fig. 4.8e) this is indicated by giving both transitions the label "17" in the list. To determine the intensity of the 795.7 keV transition one simply sets the gate on 797.8 keV.

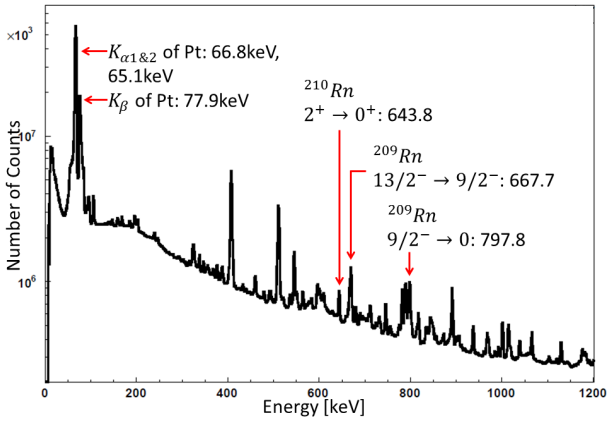

a) Sum of all cores (in log-scale)

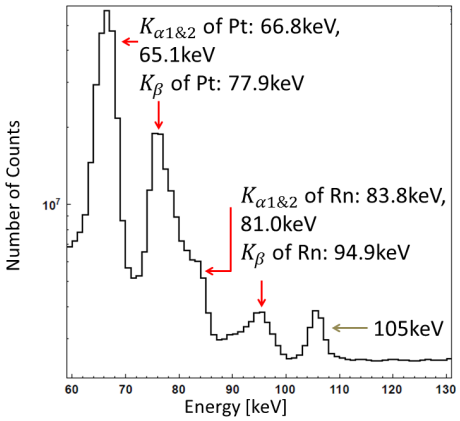

b) Zoom into K_x-ray range (in log-scale)

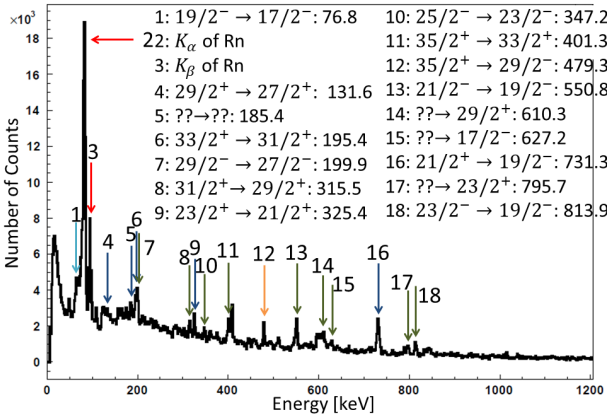

c) Gate on 387 keV

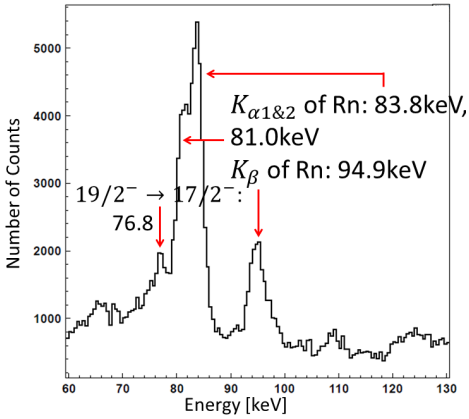

d) Zoom into K_x-ray range

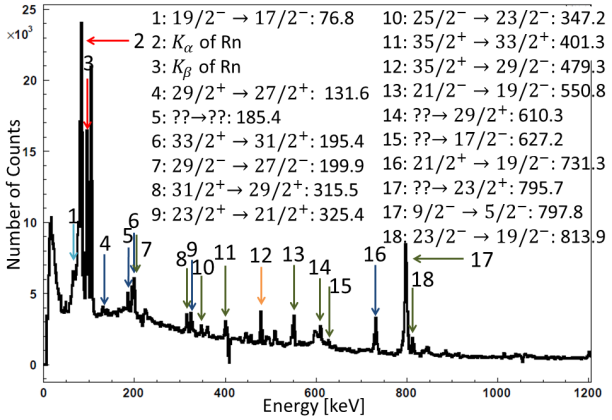

e) Gate on 667 keV

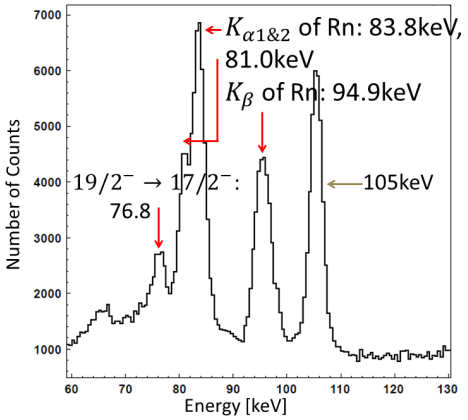

f) Zoom into K_x-ray range

Figure 4.8: The different colors of the arrows mark different decay cascades. The binning of the x-axis cause different amplitudes between the full spectrum and the K_x-ray range.

A (small) doublepeak occurs with maxima at 795 keV and 797 keV. The peak at 797 keV is explained by background and by coincidences with the 795 keV peak which lies partly

in the FWHM-gate. The ratio between the 667 keV peak and the 795 keV peak must be the same between the peaks at 795 keV and 797 keV when the gate is set on 667 keV. Thus, one gets the ratio between the peak areas of the states with the transition energies 795 keV and 797 keV. Results for the areas by setting the gate on 797 keV are found in Tab. C.1 in the appendix C. The peak at 795 keV is very small in comparison to, e.g. the 667 keV line but one has to revise the peak 797 keV in spectrum e).

Trans.	Energy [keV]	Area	K_β/K_α corr. Area
$K_{\alpha 1}$	81	14704 (509)	18203 (630)
$K_{\alpha 2}$	83	38490 (572)	47307 (703)
K_β	95	-	18342 (373)
$797 \rightarrow 0$	797	22222 (179)	76233 (614)
$M_{\gamma x} =$			1.10 (10)

Table 4.3: The gate was set on the transition energy 667 keV. The areas of the energy peaks are corrected in the fourth column. The uncalibrated areas are shown in the third column. The peak of the K_β-ray is calculated from the known ratio between K_α and K_β which is 0.28 [18]

Trans.	Energy [keV]	Area	eff.corr. Area
$K_{\alpha 1}$	81	12157 (818)	10374 (698)
$K_{\alpha 2}$	83	32484 (901)	27522 (763)
K_β	95	13020 (156)	10755 (129)
$797 \rightarrow 0$ *calc.*	797	8756 (71)	27697 (223)
$M_{\gamma x} =$			1.76 (104)

Table 4.4: The gate was set on the transition energy 387 keV. The measured ratio between the K_α and K_β peaks are very similar with the theoretical predictions.

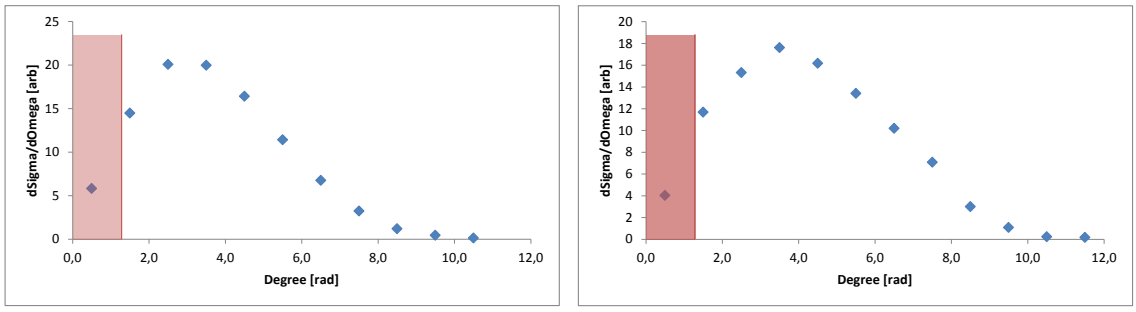

a) Angular distribution of ^{209}Rn

b) Angular distribution of ^{210}Rn

Figure 4.9: Angular distribution of the evaporation residues. Nuclei in the red marked part cannot be caught by the implantation plate. *Data from* [53]

The results for the multiplicity of the two cascades, calculated in the last rows of the Tab. 4.3 and Tab. 4.4, are quite remarkable. Actually the decay paths differ not due to the decay scheme, see Fig. 4.7, except in the last transition into the lowest excited state. However, there is a factor of 1.6 between their multiplicities. One possibility for the different multiplicity is the existence of peaks which do not belong to ^{209}Rn but overlap

with the peaks of the characteristic radiation. It is also conceivable that still unknown bands end into states which decay preferably into one of the two transitions which were used as gates. At least for the gate at 387 keV, the first possibility can be excluded since the ratio between K_αs and K_β is accords to the predicted one.
The ratio between the decay intensities of the two cascades into the state $9/2_1^-$ can only be determined indirectly. Both the isomer and the cascade via non isomeric states decay into the lowest excited state. Even if the decays of the two paths are time delayed, the transition $9/2^- \rightarrow 5/2^-$ is coincident to both transitons $13/2^- \rightarrow 9/2^-$ and $13/2^+ \rightarrow 9/2^-$.

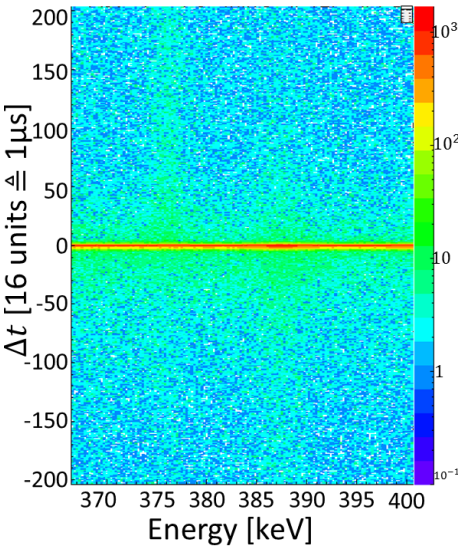

Figure 4.10: Cut of $\triangle t$-matrix with gate on K_x-rays on the transition energies 376 keV and 387 keV.

If the gate is set on the transition $9/2^- \rightarrow 5/2^-$ one gets the ratio between the isomeric and non-isomeric cascades:

$$\frac{N^{797}(667\ \text{keV})}{1.15 \cdot N^{797}(376\ \text{keV})} = \frac{92782}{41312} = 2.2(6). \quad (4.2)$$

Fig. 4.9a indicates a loss of evaporation residues of 13% due to the hole. In first order, one had to multiply the number of the isomeric decay $N^{797}(376$ keV) by 1.15 since most of the long lived states de-excite on the plate. The ratio shows that almost 2/3 of the cascades decay into the $13/2^-$-state and 1/3 decay into the isomer.
The multiplicity from the weighted sum of the two decay paths (Tab. 4.3 and Tab. 4.4) according to Equ. 4.2 is calculated to

$$M_{\gamma x} = 1.27(42). \quad (4.3)$$

Again, this result is lower than expected from previous experiments in this mass region, compare Fig. 4.12. An uncertainty is given by the so far neglected second isomer. Within the standard time window $|\triangle t| \leq 60$ ns one measures the transition with an energy of 479 keV of the isomeric state. Setting the gate on the K_x-rays and plotting the coincidence events against $\triangle t$ one gets following matrix in Fig. 4.10 for the transition energy 387 keV. There is almost no difference between positive and negative $\triangle t$. The zoom into the transition energy 667 keV is shown in Fig. C.1 in the appendix and one detects also no significant differences between positive and negative $\triangle t$. A larger value for positive $\triangle t$ would indicate isomeric decays. This is the case ,e.g., for the decay of the isomeric state 13^+ with the transition energy 376 keV which can be nicely observed in Fig. 4.10. Hence, the feeding of the rather long lived state does not contribute to the occurence of K_x-rays in a high quantity.
One can restrict the search for coincidences by using triple-coincidences where γ-peak and the K_x-rays are used as gates. For the reaction ^{16}O(^{198}Pt, $5n$)^{209}Rn, the starting point for the γ- K_x-ray- K_x-ray coincidence method is to set the first gate on the transition energies 667 keV resp. 387 keV, what guarantees to select the isotope ^{209}Rn. The transitions take place between the lowest lying excited states and the whole decay scheme is supposed to be observed. For the purpose of triple coincidences the second gate is limited to the K_αs since the peak of K_β is superimposed by a strong populated line which belongs to ^{209}Rn, too. In Fig. 4.11 the difference between γ- K_x-ray coincidences and γ- K_x-ray-

K_x-ray coincidences is demonstrated: Whereas a single gate on the 667 keV line gives contaminating peaks from platinumm (66 keV) and other nuclei (105 keV), the additional K_x-ray gate removes these completely and nicely shows the K_αs and K_β lines of ^{209}Rn, only.

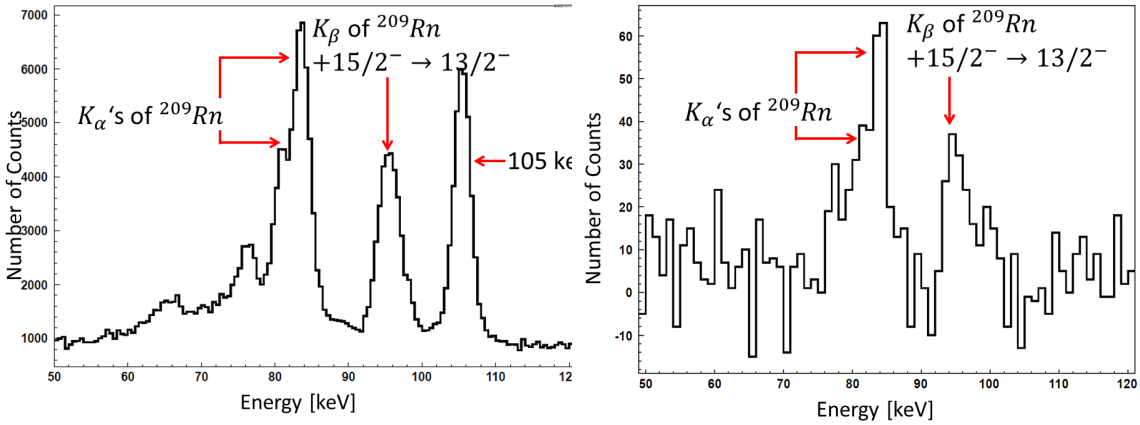

a) Energy spectrum gated on 667 keV. Lines which do not belong to ^{209}Rn e.g. the K_α of platine at 66 keV and the peak at 105 keV are visible.

b) Energy spectrum gated on 667 keV and on K_α's of ^{209}Rn. While some lines disappear the K_x-rays of radon remain.

Figure 4.11: Comparison between coincidence methods at the instance of ^{209}Rn

# Mult.	K_x-ray	Ref.	K_x-ray *corr.*	K_x-ray	Ref.	K_x-ray *corr.*
One	37592 (194)	9941 (100)	25663 (160)	32637 (181)	8341 (91)	22628 (150)
Two	407 (20)	16 (4)	391 (20)	291 (17)	9 (3)	282 (17)
Three	1 (1)	0	1 (1)	4 (2)	0	4 (2)

Table 4.5: Number of coincidences between the chosen energy ranges and K_x-rays. The first three columns refer to the gate, set on the peak at the energy 387 keV, the following three columns belong to the gate where it was set on the peak at 667 keV.

Analysing the data with the γ- K_x-ray- K_x-ray coincidence method leads to the results, summarized in Tab. 4.5. It contains the number of one/two/three coincident K_x-rays to the corresponding γ-ray line. The values of the table are processed with the accompanying K_x-ray- K_x-ray coincidence method and the multiplicity is calculated using the equations in 3.1.2. For the nucleus ^{209}Rn, one obtains a new result of

$$M_{\gamma xx} = 1.81(46) \tag{4.4}$$

where the ratio between the two decay paths is given to 2.2 due to Equ. 4.2. This multiplicity is higher than the result in Equ. 4.3. We already gave reasons in section 4.1 for this phenomenon. The just determined multiplicity of ^{209}Rn fits into the diagram, Fig. 4.12, like it is also the case for the recalculated multiplicity of ^{204}Rn. We will not present results for ^{210}Rn after the γ- K_x-ray- K_x-ray coincidence method because of strong isomeric decays.
In total, we draw the following conclusion: Multiplicities, determined with the γ- K_x-ray coincidence method exhibit smaller values than expected from previous experiments. On the other side, processing the data with the γ- K_x-ray- K_x-ray coincidence method, we

have larger results and get closer to the suggested values. Two reasons seem plausible, once that only specific decay cascades have lots of internal conversion and other cascades prefer transitions via γ-radiation.
It is also possible that the main reason lies in the distribution of the highest excited energies and spins in the evaporation residues. The decay of a part of the residues starts below the excited states where internal conversion occurs.
For the future, the next step will be to check both statements. The condition for the first one is to search for very high excited states whose transitions are coincident to K_x-rays and to find transitions of cascades which include no internal conversion. One can support the second statement by setting the gate on peaks of various transition energies and examines the feeding from higher lying states and the number of K_x-rays. If the number of K_x-rays remains constant although one set the gates on peaks with less area than lower transitions have, then one can subsequently exclude transitions within the same cascade where much of internal conversion occurs. The population and feeding of the different excited states give the percentage of states which are fed from higher transitions and the parts which are initial populated by the excited evaporation residues after they were synthetized.

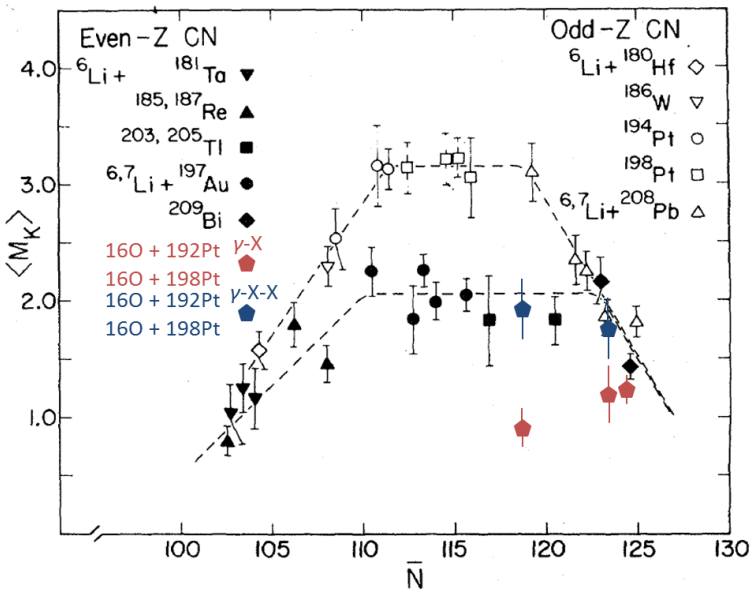

Figure 4.12: The new data together with previous measurements. *From* [42]

4.2.2 ^{210}Rn

The same experiment produces not only ^{209}Rn but in less intensity also ^{210}Rn. All transitions of excited states end in the lowest excited state which decays into the ground state with the transition energy 643.8 keV. As in the previous sections, we set the gate on this energy and get Fig. 4.14. Associated lines are labelled and the different colors belong to different cascades. The lowest excited state is fed from many cascades and in particularly from the blue marked cascade. The level scheme in Fig. 4.13 shows that the right cascade ends in the first and second cascade.

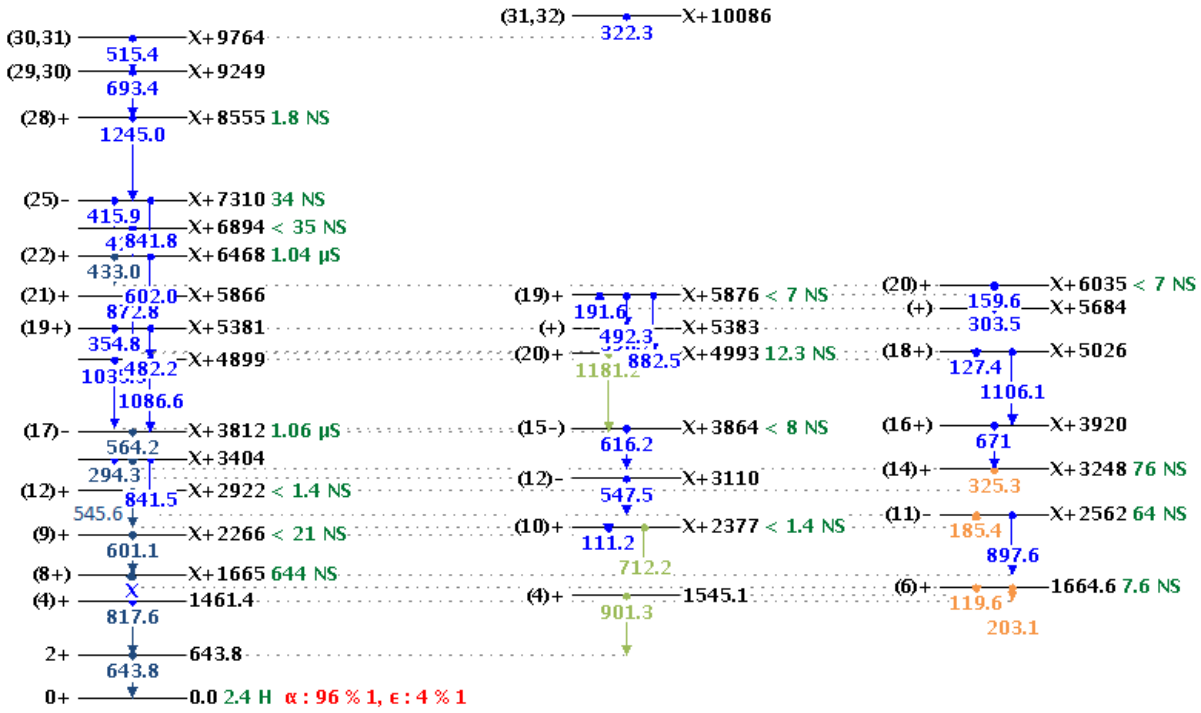

Figure 4.13: Decay scheme of ^{210}Rn. Markant lines which were found in Fig. 4.14 are colored.

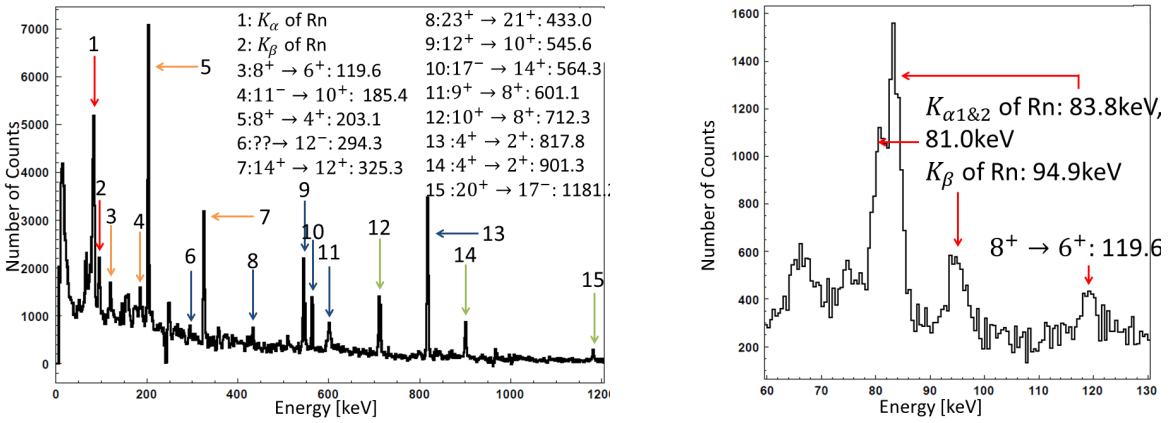

a) Gate on 643 keV

b) Zoom into K_x-ray range

Figure 4.14: The single γ-spectrum is shown in 4.14. The colors of the arrows mark different decay cascades. The binning of the x-axis cause different number of counts between the full spectrum and the K_x-ray range, shown in b).

Hence, the 2_1^+-state is populated directly by two transitions $4_1^+ \rightarrow 2_1^+$ and $4_2^+ \rightarrow 2_1^+$ with the energies 817.6 keV and 901.3 keV, respectively. For reasons, which will be discussed below, the time window to declare events as coincident is extended to $|\triangle t| < 180$ ns. If the gate is set on the lowest transition with the energy 643.8 keV, one obtains for the (preliminary) multiplicity for ^{210}Rn the value

$$M_{\gamma x} = 0.62(2). \tag{4.5}$$

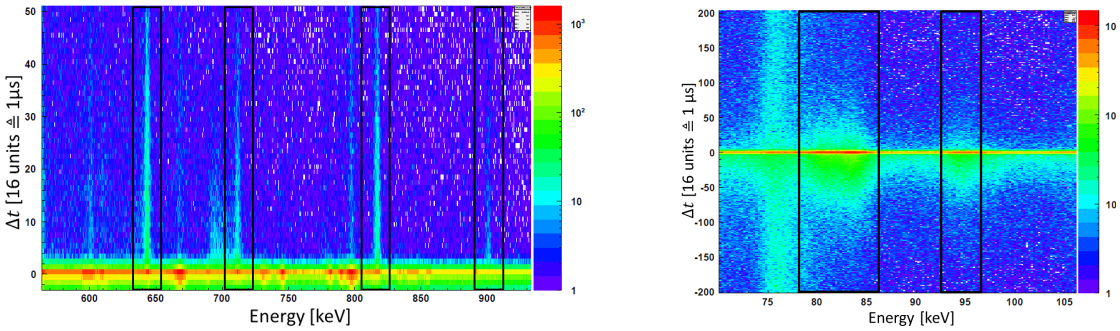

a) Gate is set on the K_x-rays of radon. The decay lines of ^{210}Rn have a large exponential decay. This gives a hint where the K_x-rays occur.

b) Gate is set on the peak at 643 keV. The decay lines of the K_x-rays of ^{210}Rn have a large exponential decay.

Figure 4.15: $\triangle t$-spectra for different gates.

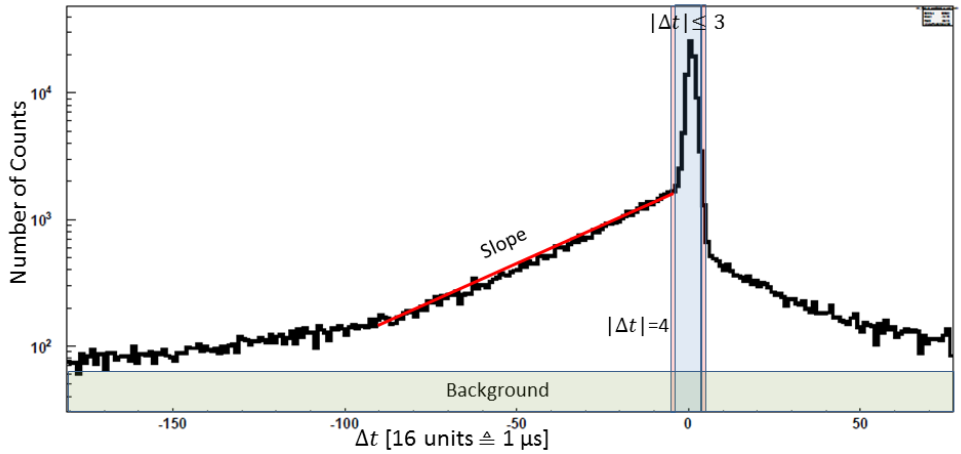

Figure 4.16: Y- Projection of Fig. 4.15, gated on K_x-rays of radon. The red slope gives the decay of the isomer. The green line is the background.

The experimental peak areas are listed in Tab. 4.6. The result for $M_{\gamma x}$ is quite small. As discussed earlier, isomers may cause such small values, as in this case the true number of K_x-rays is not measured correctly. Following the known level scheme, isomers with half lifes in the order of 1 μs are known. The effect is clearly seen in the $\triangle t$ matrices, shown in Fig. 4.15. On the left side, the gate was set on the K_x-rays of radon. Lines which belong to ^{210}Rn are enclosed with a black line. Especially, the transition energies at 643 keV and 817 keV exhibit a large tail. Thus, the just calculated multiplicity took by far too few K_x-rays into account although the time window was already extended to 180 ns. Accordingly, gating on the 643 keV photons clearly shows that K_x-rays are emitted earlier, i.e. $\triangle t$ is negative. In this spectrum the exponential decay of the isomers is visible and consistent with the known half lifes of 1 μs.
To extract the real number for $M_{\gamma x}$ a time gate of $|\triangle t| \leq 180$ ns must be used. However, this would increase the rate of random coincidences of, e.g. ^{209}Rn, significantly. To overcome this difficulty, we proceed in the following way. First, as stated before, the time window is set to $\triangle t \geq 180$ ns for the prompt part. Then, we measure the efficiency corrected area of K_x-rays $N_{\triangle t_{180\rightarrow 240}}$ in the time window from 180 ns to 240 ns when the

gate was set on the ground state transition. The additional K_x-rays are calculated via the formula

$$N_{add} = N_{\triangle t_{180\rightarrow 240}} \sum_{\triangle t} e^{a\cdot\triangle t} \tag{4.6}$$

where $a = -0.037$ is the slope of the exponent (red line in Fig. 4.16). The additional K_x-rays are listed in Tab. 4.7.
With the sum of the values from Tab. 4.6 and Tab. 4.7 the multiplicity for ^{210}Rn is calculated to

$$M_{\gamma x} = 1.25(11). \tag{4.7}$$

Also, this new data is added into Fig. 4.12. It is interested to note that this value agrees to the literature results although the γ- K_x-ray method was applied what resulted in smaller values in the case of ^{204}Rn and ^{209}Rn.

Trans.	Energy [keV]	Area	eff.corr. Area
$K_{\alpha 1}$	81	4427 (144)	5349 (174)
$K_{\alpha 2}$	83	7446 (161)	8932 (193)
K_{β}	95	3187 (93)	3727 (109)
$1461 \rightarrow 643$	817	6591 (83)	23575 (297)
$1545 \rightarrow 643$	901	1429 (47)	5462 (180)
$M_{\gamma x} =$			0.62 (7)

Table 4.6: The gate was set on the transition energy 643 keV and the time difference was set prompt.

Trans.	Energy [keV]	Area	exp. eff.corr. Area
$K_{\alpha 1}$	81	189 (21)	4733 (526)
$K_{\alpha 2}$	83	280 (24)	7012 (601)
K_{β}	95	178 (20)	4458 (501)

Table 4.7: Decay of isomeric states. Again, the transition energy 643 keV was gated. The number of the K_x-rays follows from the exponential decay, see Equ. 4.6. Also, the loss due to the hole in the implantation hole is regarded. According to Fig. 4.2.1, the loss is 16%.

Following the arguments of Karwowski et al. the plateaus in the universal curves in Fig. 4.12 were explained by γ cascades between strongly coupled rotational bands. Theoretical calculations, based on bands with "mildly deformed, high K, few-quasiparticle intrinsic states" [42], *p.25*, support K_x-ray- multiplicities of $M \approx 2$. Collective rotational bands are supposed to disappear at spherical nuclei, leading to a decreasement of the multiplicity for $N > 120$.
Thus, it seems either that the K_x-rays in ^{210}Rn are not emitted due to collective rotational bands. Instead, the isomers at low excitation energies are known to be highly converted. As almost all cascades are connected to these low-lying isomers, the difference in multiplicity after γ- K_x-ray and γ- K_x-ray- K_x-ray methods should not so strong anymore as pronounced for ^{204}Rn and ^{209}Rn. This might be a possible explanation why our result for $M_{\gamma x}$ for ^{210}Rn fits into the systematics of Karwowski et al., whereas this is not the case of ^{204}Rn and ^{209}Rn.
Of course, one has to do the γ- K_x-ray- K_x-ray method for ^{210}Rn to check our statements. This will be done in future.

Chapter 5

Reactions with Heavy Targets

The analysis of the first part of the experiments focused on the dependence of the multiplicity on nuclear structure and was based on large statistics and well known isotopes. For heavy and super heavy elements, the basic challenge is to identify them because the synthetization of these elements is associated with a drastical decrease of the production cross section. Furthermore, there is limited data available on γ-transitions. As mentioned in the introduction, an identification of the evaporation residue is proposed to be performed by measuring the K_x-rays, occuring from internal conversion.
The experiments, discussed in the last section had cross sections in the order of tens of millibarn. Heavy elements have less binding energies between the nucleons compared to lead or platinum and fission becomes more likely. At the same time, fusion cross sections decrease the scale for the cross section changes to $\mu barn$ i.e. a decrease of a factor 10^3. In addition, the cross section is strongly dependent on the beam energy and has to be chosen carefully. From literature, experiments were found from which it is possible to extrapolate the necessary beam energy ([63], [77], [7]). Fig. 5.1 shows increasing and decreasing cross sections of evaporation residues as a result of varying the beam energy. The higher the energy the more fission products occur and more evaporation channels open. Of course, fission is always the stongest channel ($\approx 1barn$) resulting in large background.
Shinohara et al. [77] determined the maximum cross section for the reaction ^{238}U(^{12}C, $4n$)^{246}Cf to $62\mu barn$ at a beam energy of 67.5 MeV, see Tab. 5.1. This is 3.3 MeV above the Coulomb barrier. For our experiment we assume that under similar nucleus-properties the maximum cross section follows approximately the height of the Coulomb barrier. For thorium the Coulomb barrier exhibits a value of 63.1 MeV. In accordance to the assumption of a correlation between Coulomb barrier and the height of the cross section, a beam energy of 67 MeV is proposed.

Reaction	σ_{max} [μb]	E_p^* [MeV]	$\Gamma_n/(\Gamma_n+\Gamma_f)^b$
^{241}Pu(^{13}C,4n)^{250}Fm	5	71	0.11
^{242}Pu(^{12}C,4n)^{250}Fm	6	72	0.12
^{238}U(^{12}C,4n)^{246}Cf	62	67.5	0.28
^{242}Pu(^{16}O,4n)^{254}No	0.034	89	0.044

Table 5.1: Experimental determined cross section of fusion with heavy targets. *From* [77]

The reference experiment in Fig. 5.1 indicates that during the formation an evaporation

of four neutrons is expected what would result to the reaction ^{232}Th(^{12}C, $4n$)^{240}Cm. The energies of the characteristic radiations are $E_{K\alpha 1} = 109.3$ keV, $E_{K\alpha 2} = 104.6$ keV and $E_{K\beta} = 123.4$ keV [15].

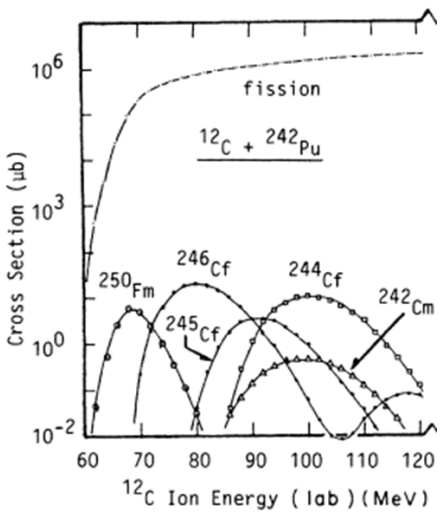

Figure 5.1: Example of the mixture of evaporation residues. Depending on the beam energy, residue channels open and close. *From* [77]

So far, the proof for the synthetization of evaporation residues was provided by their γ-lines. In the coincidence matrices, one sets the gate on the peaks and on the background. The resulted, new coincidence spectrum was purified from random coincidences and lines which did not belong to the isotop disappeared. Curium isotopes have almost no known γ-transition energies and in particular, no one is known for ^{240}Cm. Here, one has the possibility to identify evaporation residues by setting the gate on the K_x-rays and search for peaks which arise against the surrounding peaks. The probability to identify a peak in this method is much higher than ,e.g., searching for coincidences with a (known) γ-gate. In this mass region, high multiplicity is expected. Is the multiplicity for example $M = 2$ then one has twice the chance to detect a coincident peak.

The aim is not extending the level scheme with a new transition energy but to use this new peak as gate to purify the spectrum which in turn results in an increase of K_x-rays compared to lines which are not coincident to the new transition.

The finding of γ-rays which belong to evaporation residues is based on following principle: The gate on the K_x-rays is compared with two regions: One of them has a smaller energy and was taken from 95 keV to 100 keV. The other one is higher and was chosen from 135 keV to 140 keV. Fig. 5.3a shows the x-projection of the coincidence matrix in the K_x-ray region of curium. The peak at 105 keV belongs to the K_β-ray of thorium. The right one cannot be identified but it is probably a transition line of fission products. This spectrum does not allow defining background corrections for the gates. Hence the coincidence spectra will exhibit lines which are random coincident to the gate. Independently of the gate, the ratio between random coincident peaks remain equal since the identical percentage of all peaks is random coincident. One will not only observe peaks, occuring from random coincidences but also increasement of some lines which are really coincident to the K_x-ray and reference regions, respectively. To distinguish radiation from fission and from the evaporation residue, it is helpful once to gate on K_αs and then on the K_β of curium. If on both spectra the same peak is increased then this is a good candidate for a photon, occuring in the decay of the evaporation residue.

Unfortunately, no candidate for a new γ-transition in curium could be found in this work. To demonstrate the principle, in Fig. 5.2a-d are shown coincident spectra for the four mentioned gates. The gate is set from 95 keV to 100 keV in a) and from 135 keV to 140 keV in b). The spectra in c) and d) associate to the K_αs- and K_β- gate. The spectra are zoomed into an energy region where a very small indication for a peak at 981(1) keV is observed in the figures c) and d), compared to a more flat background in a) and b).

Setting the gate now on 981 keV results to the following coincidence spectra in the low

energy region: In the original coincidence spectrum, Fig. 5.3a, one recognizes a peak at 106 keV and 112 keV. The gated spectrum in Fig. 5.3b also has a peak at 106 keV but the right peak seems to slide leftwards. While the K_β region is structureless in the original coincidence spectrum, a peak at $E = 123$ keV can be assumed in the gated spectrum.

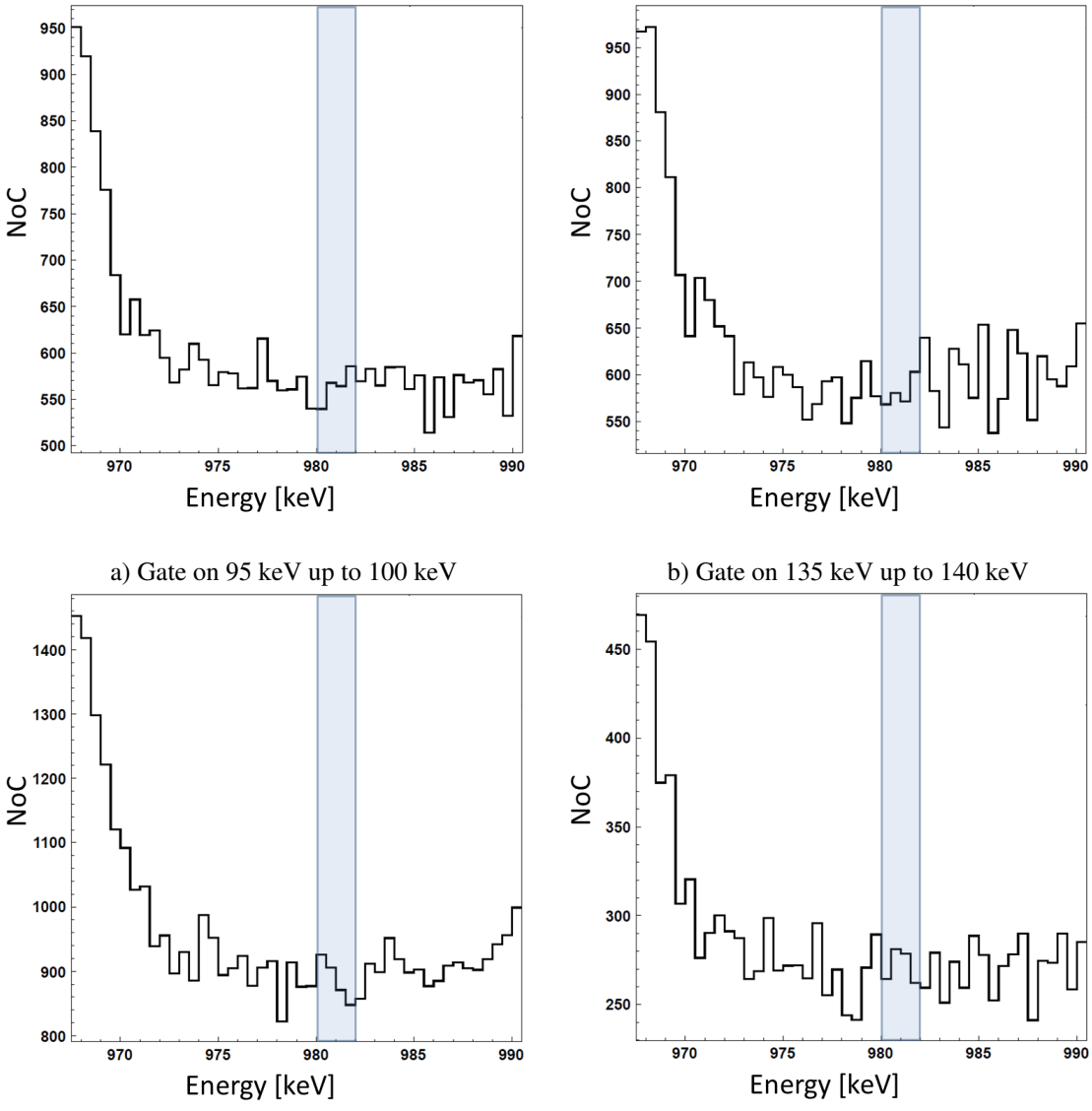

a) Gate on 95 keV up to 100 keV

b) Gate on 135 keV up to 140 keV

c) Gate on K_αs

d) Gate on K_β

Figure 5.2: Coincidence spectra using various gates.

Two further steps are necessary to clarify if this peak belongs to curium. Data from the plot in Fig. 1.7 suggest K_x-ray multiplicities larger than one in this mass region. By applying the γ- K_x-ray- K_x-ray method with the peak at 981 keV as γ-gate, one should observe more multiple coincidences in the K_x-ray region than in a reference region. Futhermore, a cross check of the results is essential and is done by using a reference gate. The ratios between the number of coincidences in the K_x-ray region should change. Tab. 5.2 contains coincident events to the two γ-gates 973 keV and 981 keV. The first two columns belong to the gate 981 keV. The ratio between the numbers of two and one coincidences is larger in the K_x-ray region than in the reference region. If the gate is

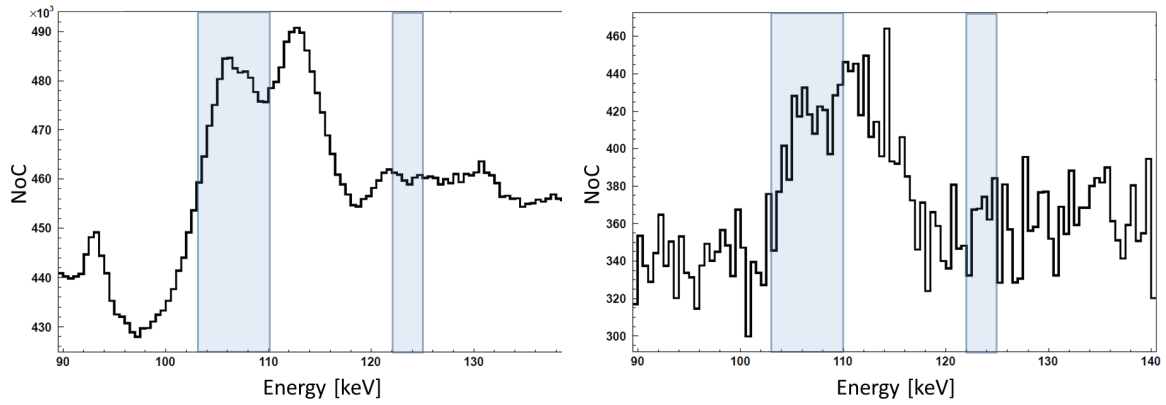

a) Original Coincidence spectrum

b) Gate on 981 keV

Figure 5.3: K_x-ray region

set on 973 keV (last two columns) then the ratio is almost equal for the K_x-ray and the reference region.

# Mult.	K_x-ray	Ref.	K_x-ray	Ref.
One	5765 (76)	2582 (51)	7950 (89)	3666 (61)
Two	16 (4)	1 (1)	17 (4)	8 (3)
Ratio	0.003 (1)	0.000 (0)	0.002 (1)	0.002 (1)

Table 5.2: Number of coincidences between the peak at 981 keV resp. the reference peak at 973 keV and K_x-rays resp. reference region from 138 keV to 143 keV.

The increase of two-coincidences in the K_x-ray region in column one compared with the value of the second column is an indicator for the formation of curium. However, the similar ratios in the first, third and fourth column make it difficult to claim the energy 981 keV as a transition energy of an isotop of curium.
An unambiguous identification was not possible. Two reasons seem plausible: First, the cross section is several orders of magnitude lower than in so far presented reactions. Second, it is possible that evaporation residues were not formed at the chosen beam energy of our experiment. As mentioned before, the choice of the beam energy was based on the extrapolation of measured data. These ones already showed that the cross section depends strongly on the actual beam energy.

Chapter 6

Lead Shielding

Heavy elements can best be produced by fusion of light ions with heavy nuclei at high beam energies. As an unwanted by-product, fission occurs massively with highly excited fission fragments. Furthermore, the fusion rate decreases drastically in comparison to targets of lighter nuclei. Hence, there is the risk that detectors are flooded unwanted γ-rays in an in-beam experiment.
In the case of fusion using medium-heavy targets, the background of a peak was subtracted by defining an energy range that was supposed to content only background events. This is justified if the background distribution is indeed random. However, at very high and extensive fission, the transition energies of many and various decaying fission products can be so close to one other, such that they are not separated and the structure seems to form a homogeneous background like structure. In reality, one set the gate on real peaks and only a little part corresponds to classical background. Hence, this method of background correction is inappropriate for fusion of heavy elements where fission is by far the strongest channel.
So a great challenge for heavy fusion- experiments is the detection of rare events in a spectrum with very high fission background radiation. We propose a solution ansatz which uses the different kinematics of fission and fusion events to suppress the fission γ-rays to some extent. After a brief presentation of the shielding design below, the next section 6.2 gives a qualitative overwiew of the expected changes in the spectra. In the main section 6.3, calculations for the new observed fusion to fission ratio are performed and discussed.

6.1 Installation of the Lead Pot

In contrast to the evaporation residues with forward momentum, fission products are emitted more isotropically in 4π. So, it would be of great benefit if the major part of the photons of fission fragments not emitted in beam direction, are blocked. Therefore, the shielding "pot" in Fig. 6.1 was developed with a slit and a beam entrance and exit. The shielding is provided by 1 cm thick lead and corresponds to an absorption of 90% for γ-rays with an energy of 500 keV. Most of internal conversion is assumed to occur in transitions of highly excited states whose lifetimes are very short. It is likely that the K_x-rays arise while the nucleus is still inside the pot. The slit is necessary for the MINIBALL- crystals to detect decays which take place in the pot. Fig. 6.2 and 6.3 illustrate the situation: Photons of nuclei which are emitted in forward direction exhibit a higher probability to

get out of the lead pot compared to the photons, rising from the decay of isotropic spread fission products. With this configuration, the observed yield of the γ-rays from fission is more reduced than the inevitably reduced yield of the photons emitted from evaporation residues. As reference and in order to determine the improved ratio, the slit was adjusted, such that not all crystals of one forward positioned detector are affected to the slit.

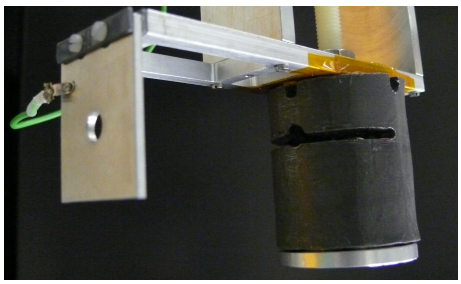

Figure 6.1: Installation of the lead pot. The slit enables forward directed crystals to detect photons from the target position.

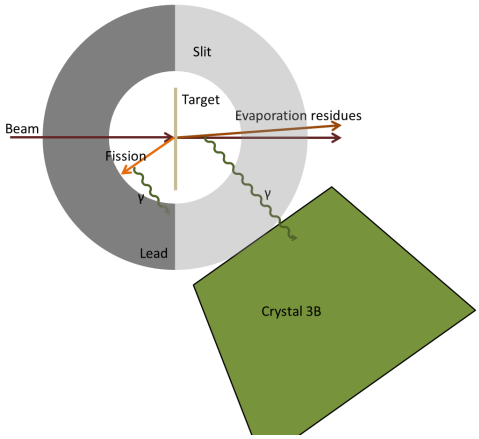

Figure 6.2: Two dimensional view of the pot from above. The probability of fission products in recoil direction to send photons to the detectors is less than evaporation residue emitted in forward direction.

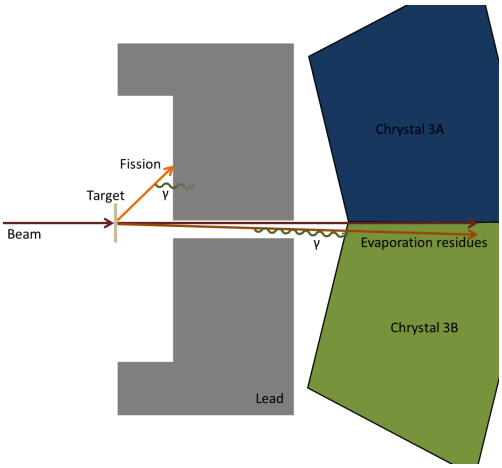

Figure 6.3: Lead pot in side view. Since the detectors lie in a plane the slit prevents γ-rays coming from fission products in beam direction but with large angle to the beam axis.

6.2 Radiation at the Target Position

The installation of the pot represents a significant change in the setup which must be calibrated using the ^{133}Ba source at target position. Fig. 6.4 shows the energy spectra for ^{133}Ba without (a)) and with (b)) direct source contact. The crystal 3A is totally shielded from the source. Since the absorption coefficient of the 1 cm thick lead depends on the energy exponentially, the intensity of the low lying peaks decreases much more than that of high energies. Note that the relative efficiencies of the crystals change, depending on the amount of lead between target and the actual crystal. ^{133}Ba shows its first line at 80.9 keV. It is strongly suppressed and its theoretical transmission through lead is only 0.1%; for higher energy photons the detection efficiency improves.

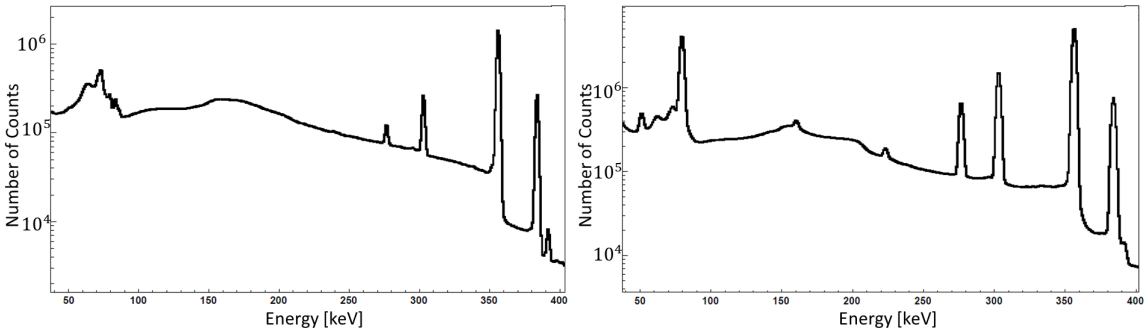

a) Spectrum of crystal 3A that sees not the source b) Spectrum of crystal 3B that sees the source

Figure 6.4: Dependency on the position of the crystal of the spectra ^{133}Ba.

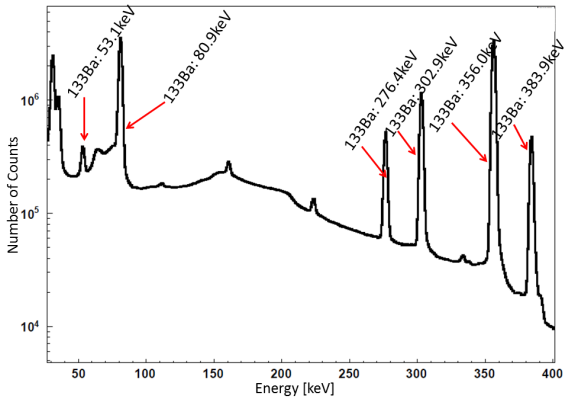

Figure 6.5: ^{133}Ba spectrum without lead pot.

This characteristic radiation is also observed in Fig. 6.4b, i.e. the spectrum of the crystals which are directed to the source. Due to the slit, now all Ba-lines are visible. The spectrum complies better with the spectrum of Fig. 6.5 which is recorded without pot.
As an example, the 80.9 keV line of ^{133}Ba is suppressed by a factor of 10, whereas the line at 356 keV is suppressed by a factor of 6 between the spectra in 6.4a and b, only.
The next section describes experiments to understand the lead pot. The main goal is to see, whether or not an improvement in the ratio between photons from fusion and fission elements can be achieved. During this analysis, the effects from changing relative efficiencies are cancelled out.

6.3 Fusion to Fission Ratio

In this section we measure the influence of the lead pot on the ratio between photons from fusion and fission elements. To observe an effect of the lead pot, both kinds of products have to decay within a period of time where the nuclei are inside the pot. This is reasonable since from the results of previous sections one has strong reasons to assume that internal conversion originates from highly excited states which decay promptly. Hence, the probability to detect K_x-rays will be enhanced if more K_x-rays of the evaporation residues enter the slit than photons of fission products.
The necessary data are obtained from the experiment in section 5 where the cross section for fission was very high. In the left energy spectrum of Fig. 6.6, no lid is mounted. The peak at 937 keV exceeds its surrounding area. The right figures come from the experiment where shielding was installed whereas in b) the crystal is full shielded and the crystal in c) was directed toward the slit. One clearly recognizes that the 937 keV peak is suppressed in contrast to the other decays which remain approximately at the same level relative to each other. It seems likely that this line stems from a fission product which radiates its characteristic line inside the pot. The other lines should stem from fission nuclei which partly could escape through the slit before transitions between excited states take place i.e. before they emit photons. The appearance of the peak at 937 keV in the spectrum b) and c) is attributed to the transmission probability of such highly energetic photons through the lead.

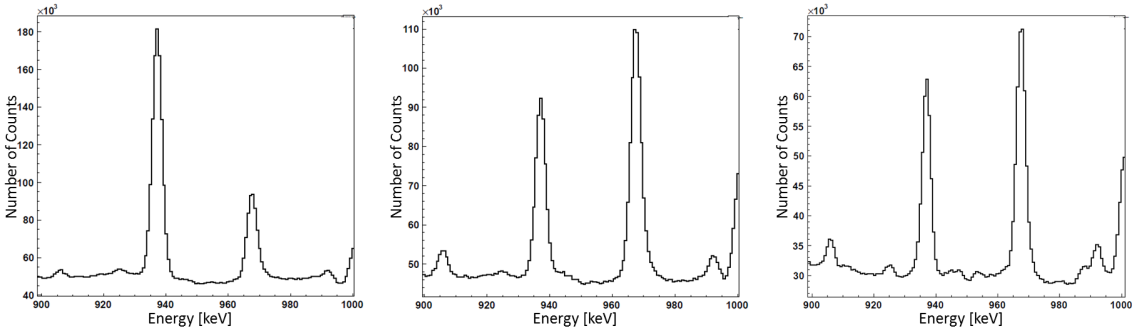

a) No shielding b) Shielding without slit c) Shielding with slit

Figure 6.6: Energy spectrum of crystal 3B from 900 keV to 1000 keV. The focus is on the decay of the 937 keV peak.

So far, it was unmentioned that the used target is a compound of ^{232}Th and ^{16}O. Hence, some of the peaks are γ-transitions of fusion products generated in the "parallel" experiment with ^{16}O as target. The produced nuclei have high kinetic energy and speed. These light elements are pushed in forward direction. The emitted radiation is shifted to frequencies depending on whether the nucleus moves towards the detector or away from it. The resulting peaks have different energies in the spectra of detectors which are positioned around the target. This phenomenon is known under the term *Doppler shift* and *Doppler broadening*. A suitable decay was found whose energy shifts from 340 keV, measured at the backward detectors, to 365 keV, measured at the forward positioned detectors. Fig. 6.7a-c show the movement of the peak in the unshielded case.
To reach spatial comparable detection systems the two crystals are taken which have the same angle relative to the beam direction whereas one crystal is focused on the slit and

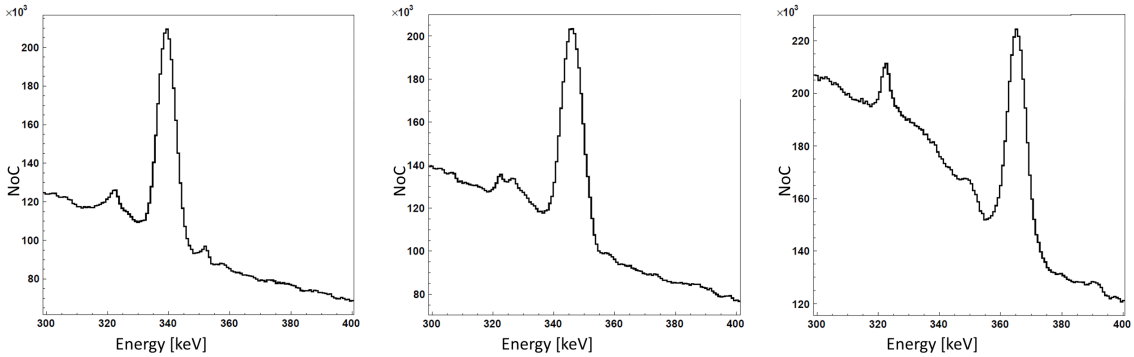

a) Backward directed crystal b) Crystal under 90° c) Forward directed crystal

Figure 6.7: Doppler broadening of a light fusion product from 340 keV to 365 keV

the other one does not record reactions within the lead pot. In this part of evaluation the localization of decay is of great importance. The crystals are sensitive to geometrical effects arising from the emitting nuclei and from the lead pot.

Efficiency calibrations already indicated that for each detector it depends on whether the decay takes place at target position or on the implantation plate. One cannot study crystals which are mounted under different angles with regard to the moving nucleus. The number of measurable photons decreases with the square of the distance between nucleus and detector. Fig. 6.8 illustrates the situation of decaying nuclei. The angles $|\theta|$ and φ are the same for the blue and green crystal but different for the red one. In this example, the first two crystals are closer to the nucleus than the right one and hence, they have a higher signal rate. The second geometrical effect deals with the size of the lead pot that cannot be neglected. It covers a part of the solid angle which hinders especially photons from evaporation residues to reach backward positioned detectors. One cannot compare forward with backward directed detectors.

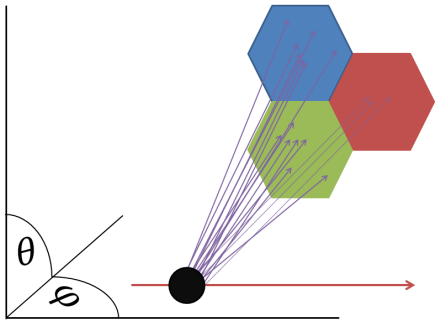

Figure 6.8: Illustration of efficiency dependency on the angle θ and φ

Taking the two effects into account let one chose crystals A and B of the forward positioned detector 3. The position of it in the setup is shown in chapter 2. In Fig. 6.9 the effect of the lead pot on the photon at 360 keV of the evaporation residue is compared with the data of the unshielded experiment. The crystal 3A detected a much less of the transition energy whereas a peak is identifiable in crystal 3B. This is in accordance to the last section where the ratio between peaks in the energy region of around 380 keV was given.

Tab. 6.1 contains the areas of peaks both with and without shielding. It includes the mentioned prompt decays of one fusion (360 keV) and one fission (937 keV) element and furthermore an additional line at 197 keV is tabulated which is taken as a reference decay of a fission nucleus. The transition takes place after a period of time where the particle

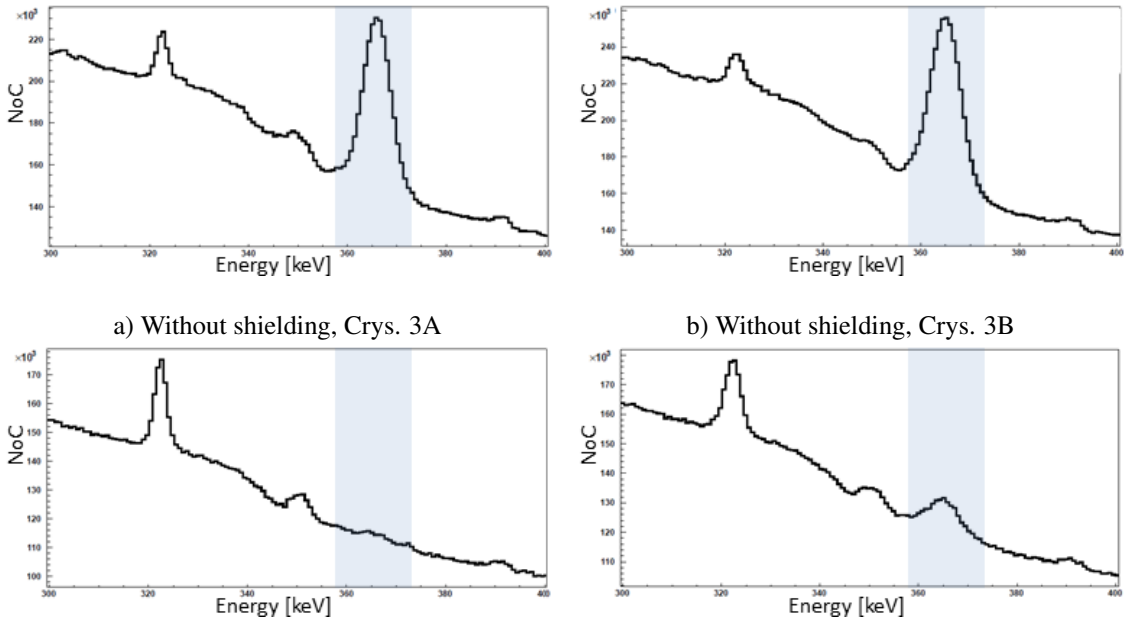

a) Without shielding, Crys. 3A

b) Without shielding, Crys. 3B

c) With shielding and without slit, Crys. 3A

d) With shielding and with slit, Crys. 3B

Figure 6.9: Prompt decay of light evaporation residue at 360 keV.

Crystal	Vol. 197 keV	Vol. 360 keV	Vol. 937 keV
3 A *nLP*	1991441 (2619)	764814 (2038)	771652 (1315)
3 B *nLP*	2188976 (3560)	973590 (2278)	827753 (1612)
3 A *wLP nS*	402245 (1835)	9785 (1377)	254387 (1062)
3 B *wLP wS*	441788 (2482)	103629 (1739)	283541 (1374)

Table 6.1: Values of the peak areas before shielding *(nLP)* and after the lead pot was installed *(wLP wS), (wLP nS)*.

is already outside of the dimension of the lead pot. Such decays do not distinguish in the spectra of the two chosen crystals. The results with this peak serve as reference for the right grading of the results obtained for the prompt decays.

By using normalized values one can abstain from efficiency which was only declared qualitatively in this chapter. The first and second row of Tab. 6.2 contain the ratios between the number of events in crystal 3A and 3B from Tab. 6.1 using the lead pot and without it, respectively. The values for the peak at 197 keV agree within the tolerance perfectly. A strong decreasement appears in the second line for the peak at 360 keV. This is comprehensible because crystal 3A can only measure photons that were not absorbed from the lead. At a lead thickness of 1 cm the transmission probability for this energy lies at about 5%. Photons with an energy of 937 keV transmit through lead with a probability of over 41%. The high value of $0.897(6)$ for the ratio between the two crystals 3A and 3B reflects this. If one compares the values from the rows one and two under the aspect of large statistics and unchanged efficiency, which is proven by the reference line, then the difference can be classified as significant and the statement is justified that this decay occurs inside the lead pot. The next row of the table presents the percentage of photons which originates not from the slit. For the reference peak the value is just pro forma and is meaningful as indicator for possible uncertainties. 12% of the area of the peak at 360

	197 keV	360 keV	937 keV
Vol. 3A / Vol. 3B *nLP*	0.910 (2)	0.786 (3)	0.932 (2)
Vol. 3A / Vol. 3B *wLP*	0.910 (7)	0.094 (13)	0.897 (6)
Ratio row 2 / row 1	1.001 (8)	0.120 (17)	0.962 (7)
Vol. 3B *theor. nLP*	1640783 (2669)	729770 (1708)	620456 (2590)
Vol. 3B *theor. wLP wS*	-356 (3331)	91172 (2336)	10659 (1884)
Transmission	-0.000 (2)	0.125 (3)	0.017 (3)

Table 6.2: Calculation results

keV originates from radiation which refers to transmission through the lead and the peak at 937 keV loses a large part of the measured events namely 96% i.e. 4% of the photons emit through the slit.
To normalize the measurements with lead pot and without lead pot to each other, we assume a transmission of 41% through the lead pot for the 937 keV photon. This normalized theoretical value is given in row four. Furthermore, the known ratios for the measurement without lead pot from Tab. 6.1 are used to obtain the corresponding values for 197 keV and 360 keV. The theoretical values for the measurements with a perfectly shielded lead pot are given in row five. These were calculated from the corresponding values of Tab. 6.1 by multiplying the transmission values, i.e. one minus the values given in the third row of Tab. 6.2. By dividing the values from row four and five, the transmission of fusion and fission events through the slit is given (row six).
The final goal of this chapter was to determine the new ratio between detected γ-rays which originate from fusion and those from fission. In the unshielded case the ratio between the areas of the peak at 360 keV and the line at 937 keV is 1.2(1). The shielded version has a better ratio of 8.6(15). While these values rely on the choice of the peaks the ratio between these gives the universal improvement of 7.2(13) due to the installation of the lead pot.
How far this value can be further enhanced is best investigated by computer simulations. The program *GEANT4* is a suitable tool to simulate such physical processes. It would be conceivable that there is an optimal size of the slit. The rate of transmitted photons through the shielding material can also be reduced by wrapping more lead or by using tantalum. This element has a higher absorption coefficient than lead. Compton scattering on lead produces K_x-rays of it and increases the rate of signals in the crystals. To prevent this radiation one might use a second shielding material which surrounds the lead. Copper for example retains many photons in this energy range and emits characteristic radiation with much lower energy (≈ 7 keV).

Chapter 7

Conclusion and Outlook

The measurements of fusion reactions were performed under several aspects. One subject was the dependence on nuclear structure for the occurence of internal conversion. Therefore, three isotopes of the chemical element radon, i.e. ^{204}Rn, ^{209}Rn and ^{210}Rn, were produced in the reactions of an ^{16}O beam with the targets ^{192}Pt resp. ^{198}Pt. The results, while empirically providing average values for the overall K_x-ray multiplicites, are difficult to interpret. The analysis with the γ- K_x-ray coincidence method exhibits smaller values for the K_x- multiplicity of all three nuclei than in the analysis with the γ- K_x-ray- K_x-ray coincidence method. This indicates that either the evaporation residues are populated not always at approximately the same excitation energy but rather over a broad range with different subsequent internal conversion probabilities, or that the internal conversion results from rather different γ-de-excitation cascades (or a combination of both).

In the theoretical part of this thesis, a mass-number dependence for the multiplicities of K_x-rays is derived. Results for K_x-ray multiplicity of previous experiments and the present study seem indeed to follow a strong mass dependence of the evaporation residue. If one extrapolates the data, a large multiplicity for super heavy elements can be expected and used to identify their formation. The detection of the K_x-rays faces two challenges: Firstly, the cross section becomes very small the heavier the target becomes and secondly, the photons from decays of the fission products flood the γ-detectors with all negative consequences, such as increased dead time and pile up effects.

Based on fusion of the ^{12}C beam with the heavy target ^{232}Th, this thesis presented approaches for solutions. The principle of the γ- K_x-ray- method is to trigger on known γ-peaks which belong to the evaporation residue and to get the number of associated K_x-rays. This method can be used vice versa, i.e. the trigger is set on the K_x-rays and one searches for associated γ-peaks. In turn, triggering on this line would purify the spectrum. In the analysis we found one peak that might belong to an evaporation residue.

The photons of both fusion and fission products are essentially emitted into 4π. But one can exploit the different distribution of the fusion and fission products. In contrast to fission which spreads isotropic, evaporation residues are forward directed. The suppression of photons from fission was achieved by installing a lead pot. The pot is more sensitive to γ-rays from nuclei with momentum in beam direction. From the comparison of decays which took place inside the lead pot, one was able to calculate the ratio between fusion and fission before and after mounting the shielding. A remarkable improvement of a factor 7 could be reached.

Steps for the future are the enhancement of the shielding geometry and the overall experimental setup. Detailed computer simulations will be necessary to optimize the design. The MINIBALL-detectors had a relatively large distance to the target and measured a significant number of signals from photons which transmitted through the lead. This background is reduced if smaller detectors are positioned such that only photons emerging from the slit are measured.
The accelerator facility at the Maier Leibnitz Laboratory supplies insufficient beam energy to perform super heavy element experiments. The present setup can be seen as a preliminary step towards fusion experiments in international facilities. A first tentative experiment, for example, has been discussed with the GARIS SHE team at RIKEN in Japan.

Appendix A

Internal conversion uses electrons from the atomic K-shell to get rid of electro-magnetic fields inside the excited nucleus. The vacance K shell will be filled from an electron from next higher shells, mostly from the L- and M-shell. Due to lower binding energy the electron loses energy by emitting photons, the so called K_x-rays. Moseley's law gives the energy of the K_x-ray

$$E = E_i - E_f = \frac{m_e q_e^4 (Z-1)^2}{8h^2\epsilon_0^2}(\frac{1}{1^2} - \frac{1}{n_i^2}) \tag{A.1}$$

where $(1/1^2 - 1/n_i^2)$ represents the atomic quantum numbers of the initial energy level n_i and the final energy level $n_f = 1$, m_e is the mass of the electron, q_e is the electron's charge. One refers to K_α if the transferred electron comes from the L-shell. K_β corresponds to the transition of an electron from the M-shell to the K-shell. Transitions from higher atomic shells are unlikey due to $1/n_i^2$ term in Equ. A.1. One distinguishs the characteristic radiation in dependence on the magnetic moment of the transferred electron, e.g., K_α splits into $K_{\alpha 1}$ and $K_{\alpha 2}$. Lesk [50] pointed out that the term $(Z-1)^2$ comes from electron-electron repulsion in the initial and final states.

Appendix B

Detection of γ- Radiation in Semiconducter Detectors

The detection process of photons in a semiconductor detector can be divided into three steps. Before each process will be described in detail, the whole process is outlined briefly: The semiconductor corresponds to a reverse-biased PIN- diode whose reverse high voltage lets the area between the electrodes become a depletion zone. First, the γ- particle strikes the depletion zone where it reacts with the detector material by photo effect, Compton scattering or pair creation. In each of the three processes, one or more high energy electrons are produced. The second step is characterized by the interaction of the electrons on their path through the zone. They slow down due to band structures of the semiconductor and generate a number of electron hole pairs which are proportional to the incident electron's energy. Finally, these electrons and holes drift toward the electrodes where their charge is read out as a current.

The following sections are based on [22], [44] and [81].

B.1 Energy Transition of Photons

The photon strikes the detector and interacts with the material. The proportionality of interaction increases rapidly with the number of protons Z of the detector material. Depending on its energy various processes are possible. Photo effect occurs at low γ- energy (keV- region) and the energy is complete absorbed by an electron that is bound within the atomic shell. If the photon has a higher energy (between 100 keV and 2 MeV) then Compton- scattering, i.e. inelastic collisions with quasi-free electrons is probable till the energy has lowered so much that photo effect occurs. In the case of a chain of successive Compton scattering, the total energy of the photon is therefore not transferred to a single electron but to several. To calculate the Doppler correction, Weisshaar pointed out that the first impact must have the highest energy disposition and showed that this is true for the most cases [81].

In our experiments, we are not interested in photons with higher energies and the last process will just be mentioned for completeness. If the photon exceeds twice the rest mass of one electron, pair creation is able to occur in the Coulomb field of an atom and creates an electron-positron pair.

B.2 Creation of Electron-Hole Pairs

The ejected electrons lose their energies by collisions within the depletion zone. The secondary electrons are lifted from the valence band to the conduction band, losing a hole in the valence band. The needed energy in germanium is only 2.96 eV which is the reason for the detector's high resolution. A primary electron with one MeV generates about $3 \cdot 10^5$ electron hole-pairs over a distance of about 1 mm and emits its energy on a time scale of about 10^{-11}s, approximately at the position of the interaction with the photon. The time scale is four orders of magnitudes shorter than the time to accumulate the charge. This information is important to decide whether detectors can localize the position of the photon. In this case, one can proceed to prompt and clearly localized electron-hole pair creation.

B.3 Signal Generation

In principle, the electron-hole pairs can be seen as one negatively and one positively charged component. Before they recombine, each of them will be moved to its opposite charged electrode. At the positive electrode (anode) the q^-- component influences charges in form of electrons which are measurable as current. If the electron has finally reached the electrode the influence charge corresponds to the whole charge of the q^-- component. For the positive charge the process is the same. In reality the components affect their opposite equal- charged electrode as well. It ends not until both charge components reached their electrodes. Fig. B.1 shows the time sequence of the measured current. The bend comes from the just described influence.

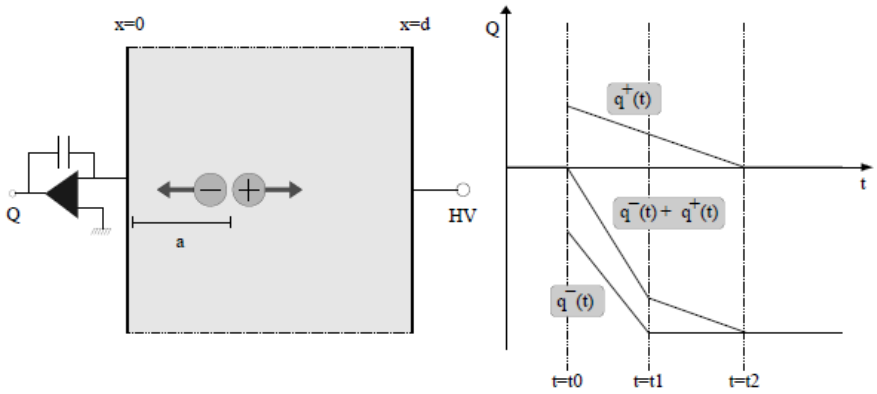

Figure B.1: *Left* is marked the position a of the entrance of the photon that excites electrons. The latter ones generate electron-pair holes in short time and at the same position. Depending on their charge the components move to the electrode with opposite charge. *Right* shows the theoretical charge, each component triggers. The sum gives the measurement result. *From* [81]

With the knowledge of the mobility of the charge components one is also able to determine the position of the incident photon.

Appendix C

Results of the γ- K_x-ray coincidence method for the gate at 797 keV:

Trans.	Energy [keV]	Area	eff.corr. Area	incl. plate
$13/2^+ \rightarrow 9/2^-$	376	13066 (139)	36559 (439)	41311 (496)
$13/2^- \rightarrow 9/2^-$	667	24069 (172)	92782 (663)	92782 (663)
$797 \rightarrow 0$	795	954 (73)	76233 (5833)	76233 (5833)

Table C.1: The gate was set on the transition energy 797 keV.

Zoom into the 667 keV energy region of the $\triangle t$-matrix between K_x-rays of radon and coincident photons for the reaction ^{198}Pt(^{16}O,5n)^{209}Rn:

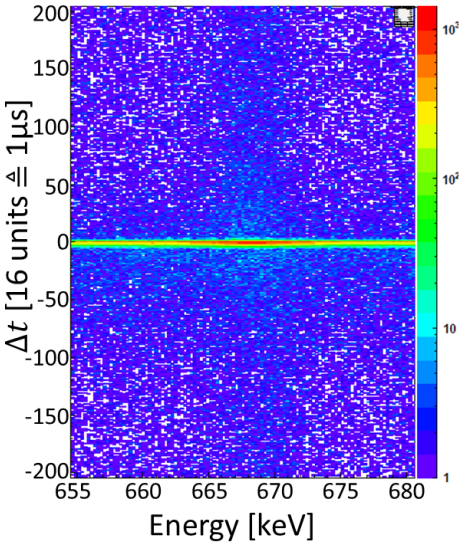

Figure C.1: Cut of $\triangle t$-matrix with trigger on K_x-rays on the transition energy 667 keV.

Uncertainties in background subtraction

The determination of the area of the peak depends on the right subtraction of the background. The subtraction involves always uncertainties. Hence we take two backgrounds which might be possible. The formula to calculate the maximum percentage p of uncertainty in the area of one peak is

$$p = \frac{|N(E_{back1}) - N(E_{back2})|}{N(E_{Peak})} \tag{C.1}$$

where $N(E_{back1})$ is the normalized area of the first energy background region. $N(E_{back2})$ is the normalized area of the second energy background region and $N(E_{Peak})$ is the number of counts in the peak of the transition energy.
For the peak 542 keV in ^{204}Rn:

Energy range [keV]	Area	normalized Area
540-544	3748593	
548-550	1563981	3127962
531-533	1983316	3966632
Uncert. [%]		22

Table C.2: The first line corresponds to N_{Peak}. The last two rows are the areas of different backgrounds $N(E_{back1})$ and $N(E_{back2})$.

For the peak 797 keV in ^{209}Rn:

Energy range [keV]	Area	normalized Area
796-799	2103777	
764-772	2272243	852091
821-836	1285844	257169
Uncert. [%]		28

Table C.3: The first line corresponds to N_{Peak}. The last two rows are the areas of different backgrounds $N(E_{back1})$ and $N(E_{back2})$.

For the peak 667 keV in ^{209}Rn:

Energy range [keV]	Area	normalized Area
666-669	2976931	
673-675	1010340	1414476
650-653	1269467	1184836
Uncert. [%]		8

Table C.4: The first line corresponds to N_{Peak}. The last two rows are the areas of different backgrounds $N(E_{back1})$ and $N(E_{back2})$.

For the peak 387 keV in ^{209}Rn:

Energy range [keV]	Area	normalized Area
387-389	2631153	
392-394	1304234	1304234
380-381	1388569	2777138
Uncert. [%]		56

Table C.5: The first line corresponds to N_{Peak}. The last two rows are the areas of different backgrounds $N(E_{back1})$ and $N(E_{back2})$.

For the peak 643 keV in ^{210}Rn:

Energy range [keV]	Area	normalized Area
642-645	1038871	
648-650	487284	974568
638-640	527810	1055620
Uncert. [%]		8

Table C.6: The first line corresponds to N_{Peak}. The last two rows are the areas of different backgrounds $N(E_{back1})$ and $N(E_{back2})$.

List of Figures

List of Tables

Bibliography

[1] K. Andgren: *Lifetime Measurements of excited states in ^{165}Lu and ^{107}Cd, Licentiate Thesis in Physics, Stockholm* (2006).

[2] R. Anholt and J. O. Rasmussen: *Phys. Rev. A, Vol.9, No. 2* (1974).

[3] R. Anholt: *Z Physik A - Atoms and Nuclei 292, 123-130* (1979).

[4] R. Anholt: *Z. Phys. A - Atoms and Nuclei 306, 285-295* (1982).

[5] M. Bender: *Structure of superheavy nuclei, 11th Int. Conf. on Nucl-Nucl Collisions May 27 - June 1 2012*.

[6] J. F. Berger and K. Pomorski: *Phys. Rev. Lett. Vol. 85 No. 1* (2000).

[7] D. C. Biswas, R. K. Choudhury, B. K. Nayak D. M. Nadkarni and V. S. Ramamurthy: *Phys. Rev. C Vol. 56 No. 4* (1997).

[8] S. Bjonholm: *Nucl. Phys. A 387, 51c* (1982).

[9] J. P. Briand, J. P. Rozet, P. Chevallier, A. Chetioui, M. Tavernier and A. Touati: *PJ. Phys. B: Atom. Molec. Phys. 13 (1980), 4751-4755*.

[10] B. Bruyneel: *Characterization of Segmented Large Volume, High Purity Germanium Detectors, Inaugural-Dissertation* , University of Cologne, (2006).

[11] P. A. Butler, R. D. Humphreys *et al.*: *Phys. Rev. Lett. Vol. 89 No. 20* (2002).

[12] P. A. Butler, P. M. Jones, K. J. Cann, J. F. C. Cocks, G. D. Jones, R. Julin and W. H. Trzaska: *Nucl. Instr. and Methods in Phys. Research A 381, 433-442* (1996).

[13] R. Butsch, D. J. Hofman, C. P. Montoya, P. Paul and M. Thoennessen: *Phys. Rev. C Vol. 44 No. 4* (1991).

[14] J. Byrne and N. Howarth: *J. Phys. B: At. Mol. Phys. 3, 280* (1970).

[15] T. A. Carlson and C. W. Nestor Jr.: *At. Data Nucl. Data Tables 19 153-173* (1977).

[16] R. F. Casten: *Nuclear Structure from a simple Perspective*, 2. Edition: Oxford University Press, (2000).

[17] S. Cohen, F. Plasil and W. J. Swiatecki: *Ann. Phys. (NY), 82, 557* (1974).

[18] B. Crasemann: *Atomic Inner Shell Processes I*, 1. Edition: Academic Press Inc, (1975).

[19] M. Dasgupta, D. J. Hinde, J. O. Newton and K. Hagino: *The nuclear potential in heavy-ion fusion* (*NN*).

[20] A. Dobrowolski, K. Pomorski and J. Bartel: *Phys. Rev. C 75, 024613* (2007).

[21] C. E. Duellmann: *Nucl. Instr. and Methods in Phys. Research B 266 4123–4130* (2008).

[22] J. Eberth, G. Pascovici *et al.*: *Miniball: A Gamma- Ray Spectrometer with position- sensitive Ge Detectors for Nuclear Structure Studies at Rex-Isolde* (*NN*)

[23] T. Ericson: *Nucl. Phys. 17, 250-263* (1960).

[24] H. Ernst, W. Henning, C. N. Davids, W. S. Freeman, T. J. Humanic, M. Paul, S. J. Sanders, F. W. Prosser and R. A. Racca: *Phys. Letters Vol. 119B, No. 4,5,6* (1982).

[25] H. Ernst, W. Henning, C. N. Davids, W. S. Freeman, T. J. Humanic, F. W. Prosser and R. A. Racca: *Phys. Rev. C Vol. 29, No. 2* (1984).

[26] G. Fazio, G. Giardina, A. Lamberto, C. Sacca, R. Palamara, A. I. Muminov, A. K. Nasirov, K. V. Pavliy, F. Hanappe, T. Materna and L. Stuttge: *Journal of the Phys. Society of Japan, Vol. 74, No. 1, 307–316* (2005).

[27] H. Feshbach: *Theoretical Nuclear Physics, Nuclear Reactions*, John Wiley and Sons, (1992).

[28] H. Friedrich: *Scattering Theory, Lecture Notes in Physics*, 1. Edition: Springer, (2013).

[29] N. K. Glendenning: *Rev. of Modern Phys. Vol. 47 No. 3* (1975).

[30] K. Green: *Master Thesis: Nuclear Structure of 112Cd through studies of β- decay*, Faculty of Graduate Studies, University of Guelph, (2010).

[31] K. Hagino, N. Rowley and M. Dasgupta: *Fusion cross sections at deep subbarrier energies* (*NN*).

[32] C. Hinke and L. Fabietti: *Fortgeschrittenenpraktikum Gamma Spektroskopie*, TU Munich, (2007).

[33] K. Hagino and N. Takigawa: *Subbarrier fusion reactions and many-particle quantum tunneling* (2012).

[34] S. Heinz, S. Hofman: *et al.*: *Eur. Phys. J. A 48: 32* (2012).

[35] W. F. Henning: *Nuclear Physic A400 (1983), 295c-314c*.

[36] W. F. Henning, Khoo *Compound Nuclear X-Ray Multiplicities - Prospects for Atomic-Number Determination of SHEs*, Argonne National Laboratory, (2012).

[37] R.-D. Herzberg, S. Moon *et al.*: *Eur. Phys. J. A 42, 333–337* (2009).

[38] *www.hzdr.de/ FWK/ MITARB / rs / highspin.html* invoked at 16.2.2013.

[39] R. Julin: *Lect. Notes Phys. 651, 263–294* (2004).

[40] H. J. Karwowski, S. E. Vigdor, W. W. Jacobs, S. Kailas, P. P. Singh, F. Soga and W. D. Ploughe: *Phys. Rev. Letters Vol. 42, No. 26* (1979).

[41] H. J. Karwowski, S. E. Vigdor, W. W. Jacobs, T. G. Throwe, D. L. Wark, S. Kailas, P. P. Singh, F. Soga, T. E. Ward and J. Wiggins: *Phys. Rev. Letters Vol. 47, No. 18* (1981).

[42] H. J. Karwowski, S. E. Vigdor, W. W. Jacobs, S. Kailas, P. P. Singh, F. Soga, T. G. Throwe, T. E. Ward, D. L. Wark, and J. Wiggins: *Phys. Rev. C Vol. 25, No. 3* (1982).

[43] S. Ketelhut, P. T. Greenlees *et al.*: *Phys. Rev. Letters 102, 212501* (2009).

[44] G. F. Knoll: *Radiation Detection and Measurement*, 4. Edition: John Wiley and Sons, (2010).

[45] K. S. Krane: *Introductory Nuclear Physics*, John Wiley and Sons, (1988).

[46] M. O. Krause: *J. Phys. Chem. Ref. Data, Vol. 8 No. 2* (1979).

[47] R. Kruecken: *Skript zur Vorlesung KTA im WS 2011/12*, TU Munich, (2011).

[48] Ajay Kumar, Hardev Singh, Rajesh Kumar, I. M. Govil, R. P. Singh, Rakesh Kumar, B.K. Yogi, K.S. Goldac, S.K. Datta, G. Viesti: *Nucl. Phys. A 798 1–15* (2008).

[49] M. Leino: *Nucl. Inst. and Methods in Phys. Research B 204 129–137* (2003).

[50] A. M. Lesk: *Am. Journ. Phys. 48, 492* (1980).

[51] K. T. Lesko, W. Henning, K. E. Rehm, G. Rosner, J. P. Schiffer, G. S. F. Stephans, B. Zeidman and W. S. Freeman: *Phys. Rev. Letters Vol. 55, No. 8* (1985).

[52] D. A. Liberman, D. T. Cromer and J. T. Waber: *Comp. Phys. Communications 2 107-113.* (1971).

[53] M.Hillman and Y.Eyal (code Julian), Avigdor Gavron (code PACE): PACE4 on LISE, Version 4.19.3, (2011).

[54] A. Lopez- Martens, K. Hauschild *et al.*: *Eur. Phys. J. A 32, 245–250* (2007).

[55] Mesytec Homepage *http://www.mesytec.com/ datasheets/ STM-16.pdf* invoked at 3.8.2013.

[56] W. E. Meyerhof, R. Anholt, J. Eichler and A. Salop: *Phys. Rev. A Vol. 17, No. 1* (1978).

[57] H. Morgenstern, W. Bohne, K. Grabisch, H. Lehr, and W. Stoeffler: *Z. Phys. A 313, 39-49* (1983).

[58] K. Morita, K. Morimoto, D. Kaji *et al.*: *Journal of the Phys. Society of Japan Vol. 73, No. 10, pp. 2593–2596* (2004).

[59] T. Mukoyama and H. Adachi: *Journal of the Phys. Society of Japan Vol. 53, No. 11, pp. 3782–3787* (1984).

[60] T. Mukoyama and H. Adachi: *Bull. Inst. Chem. Res., Vol. 67, No. 1*, Kyoto Univ, (1989).

[61] J. O. Newton: *Phys. Scr. 24 83* (1981).

[62] H. Nishioka, J. J. M. Verbaarschot, H. A. Weidenmueller and S. Yoshida: *Annals of Phys. 172, 67-99* (1986).

[63] K. Nishio, H. Ikezoe, Y. Nagame, M. Asai, K. Tsukada, S. Mitsuoka, K. Tsuruta, K. Satou, C. J. Lin and T. Ohsawa: *Phys. Rev. Lett. 93, 162701* (2004).

[64] National Nuclear Data Center, Brookhaven, New York, USA, *http://www.nndc.bnl.gov/ ensdf/* invoked at 10.7.2013.

[65] H. Oeschler, H. Freiesleben, K. D. Hildesbrand, P. Engelstein, J. P. Coffin, B.Heusch, and P. Wagner: *Phys. Rev. C Vol. 22, No. 2* (1980).

[66] Yu. Oganessian, V. K. Utyonkov, Yu. V. Lobanov *et al.*: *Phys. Rev. C 70, 064609* (2004).

[67] Yu. Oganessian: *J. Pure Appl. Chem., Vol. 78, No. 5, pp. 889–904* (2006).

[68] Z. Patyk and A. Sobiczewski: *Nuclear Physics A533 132-152* (1991).

[69] Z. Patyk, J. Skalski, R. A. Gherghescu and A. Sobiczewski: *APH N.S., Heavy Ion Physics 7 13-22* (1998).

[70] P. Reiter, T. L. Khoo, T. Lauritsen, C. J. Lister *et al.*: *Phys. Rev. Letters Vol. 84, No. 16* (2000).

[71] W. Reviol, D. G. Sarantites, R. J. Charity, C. J. Chiara, J. Elson, M. Montero, O. L. Pechenaya, S. K. Ryu and L. G. Sobotka: *Nucl. Instr. and Methods in Phys. Research A 541 478–500* (2005).

[72] W. Reviol, D. G. Sarantites, R. J. Charity, C. J. Chiara, J. Elson, M. Montero, O. L. Pechenaya, S. K. Ryu and L. G. Sobotka: *Spectroscopy Of Light Lead And Actinide Nuclei Using An Evaporation Residue Detector*, American Institute of Physics, (2005).

[73] M. E. Rose, L. C. Biedenharn and G. B. Arfken: *Phys. Rev. Vol. 85, No. 1* (1952).

[74] D. M. Sanchez- Cano: *Dopplerkorrektur mittels Impulsformanalyse – Untersuchung eines zwölffach segmentierten Germanium-Detektors, Diploma thesis*, University of Cologne, (2005).

[75] H. Schmeiduch: *Eine Methode zur Messung magnetischer Momente von Atomkernen im fs-Bereich, Diploma- thesis*, TU Munich, (2012).

[76] J. H. Scofield: *Phys. Rev. Vol. 179, No. 1* (1969).

[77] N. Shinohara, S. Usuda *et al.*: *Phys. Rev. C 34, 909-913* (1986).

[78] A. Sobiczewski and I. Muntian: *Nuclear Physics A734 176-179* (2004).

[79] T. C. Tucker, L. D. Roberts, C. W. Nestor, T. A. Carlson and F. B. Malik: *Phys. Rev. Vol. 174, No. 1* (1968).

[80] A. M. van den Berg, W. F. Henning, L. L. Lee, Jr., K. T. Lesko, K. E. Rehm, J. P. Schiffer, G. S. F. Stephans, F. L. H. Wolfs and W. S. Freeman: *Phys. Rev. Letters Vol. 56, No. 6* (1986).

[81] D. W. Weisshaar: *MINIBALL: Ein neuartiges Gamma-Spektrometer mit ortsauflösenden Germaniumdetektoren, Inaugural Dissertation* (2003): University of Cologne.

[82] T. Wendel, J. Groeger, C. Guenther, A. I. Levon *et al.*: *Phys. Rev. C 65, 014309* (2001).

[83] Wikipedia: *http://de.wikipedia.org/wiki/Fermis_Goldene_Regel* invoked at 28.4.2013.

[84] Wikipedia: *http://en.wikipedia.org/wiki/Constant_fraction_discriminator* invoked at 29.9.2013.

[85] S. S. M. Wong: *Introductory Nuclear Physics*, Wiley VCH Verlag, (2004).

Erklärung

Erklärung zur Master-Arbeit gemäß § 29 (Abs.6) LPO I.

Hiermit erkläre ich, dass die vorliegende Arbeit von mir selbstständig verfasst wurde, und dass keine anderen als die angegebenen Hilfsmittel benutzt wurden. Die Stellen der Arbeit, die anderen Werken dem Wortlaut oder Sinn nach entnommen sind, sind in jedem einzelnen Fall unter Angabe der Quelle als Entlehnung kenntlich gemacht.

Diese Erklärung erstreckt sich auch auf etwa in der Arbeit enthaltene Grafiken, Zeichnungen, Kartenskizzen und bildliche Darstellungen.

München, im Oktober 2013